UNIVERSITY OF CALIFORNIA, SAN DIEGO

Modelling the Phase Angle in Periodic fMRI Signals

A dissertation submitted in partial satisfaction of the
requirements for the degree Doctor of Philosophy
in
Electrical Engineering (Intelligent Systems, Robotics, and Control)

by

Chingfu Chen

Committee in charge:

Kenneth Kreutz-Delgado, Chair
Vikash Gilja
Ruey-Song Huang
Tzyy-Ping Jung
Thomas T. Liu
Truong Nguyen

2018

The Dissertation of Chingfu Chen is approved, and it is acceptable in quality and form for publication on microfilm and electronically:

Chair

University of California, San Diego

2018

DEDICATION

To my family, advisors Drs. Ruey-Song Huang and Kenneth Kreutz-Delgado, my friends, and everyone who helped me directly or indirectly toward my success.

TABLE OF CONTENTS

LIST OF FIGURES

LIST OF TABLES

ACKNOWLEDGEMENTS

I would like to appreciate my parents, my sister, and my aunts for the supports throughout my life. Talking to them is the best time in my Ph.D. student life.

I would like to thank Doctor Ruey-Song Huang for his guidance. Since I was in Taiwan, he pointed out what I did not see in my research and directed my research to the right track. I also want to show appreciation to Professor Kreutz-Delgado for providing the opportunity to show my ability for being a Ph.D. student in a world-famous university, strengthening my mathematically thinking and providing great insights in my research. Also thank Professors Tzyy-Ping Jung, Chin-Teng Lin, and Tzai-Wen Chiu for enriching my knowledge in neuroscience since my postgraduate study.

Thanks Lester Lee-Kang Liu, Hung-Wei Tseng, Yute Wang, Chun-Shu Wei, Shawn Sheng-Hsiou Hsu, Tony Ming-Hung Yen and other Taiwanese students for the support in life. Thanks Özgür Yiğit Balkan, Srinjoy Das, Luca Pion-Tonachini, Ramón Martinez Cancino, Alejandro Ojeda, and friends from Swartz Center for Computational Neuroscience for sharing the knowledge in the research.

Thanks all my TA students. You helped me overcome the fear of public speaking.

Chapter 2, in full, is a reprint of Chen, C.F., Kreutz-Delgado, K., Sereno, M.I., Huang, R.S., 2017. Validation of periodic fMRI signals in response to wearable tactile

stimulation. NeuroImage 150:99-111. The dissertation author was the primary investigator and author of this paper. I want to thank Doctor Ruey-Song Huang for the guidance of the direction of the research and Professor Kenneth Kreutz-Delgado for making mathematical statements more rigorous and unambiguous. Also thank Professor Marty Sereno for FreeSurfer support and comments on the manuscript.

Chapter 3, in full, is currently being prepared for submission for publication as Chen, C.F., Kreutz-Delgado, K., Sereno, M.I., Huang, R.S. Unraveling the spatiotemporal brain dynamics during a reach-to-eat task. The dissertation author was the primary investigator and author of this material. I want to thank Doctor Ruey-Song Huang for the guidance of the direction of the research and Professor Kenneth Kreutz-Delgado for making mathematical statements more rigorous. Also thank Professor Marty Sereno for the help on FreeSurfer and commenting the draft.

Chapter 4, in full, is a reprint of Huang, R.S., Chen, C.F., Sereno, M.I., 2017. Mapping the complex topological organization of the human parietal face area. NeuroImage 163:459-470. The dissertation author used circular statistics to investigate the association of phase angles in the fMRI signals in a voxel responding to visual and tactile stimuli. Also thank Professor Marty Sereno for FreeSurfer support and comments on the manuscript.

VITA

2003 Bachelor of Sciences, National Chiao Tung University, Taiwan

2009 Master of Sciences, National Chiao Tung University, Taiwan

2009-2010 Research Assistant, National Chiao Tung University, Taiwan

2011 Staff Research Associate, University of California, San Diego

2011-2018 Research Assistant, University of California, San Diego

2015-2017 Teaching Assistant, University of California, San Diego

2018 Doctor of Philosophy, University of California, San Diego

Publications:

Huang, R.S., Chen, C.F., Tran, A.T., Holstein, K.L., Sereno, M.I., 2012. Mapping multisensory parietal face and body areas in humans. Proc. Natl. Acad. Sci. USA 109, 18114-18119.

Huang, R.S., Chen, C.F., Sereno, M.I., 2015. Neural substrates underlying the passive observation and active control of translational egomotion. J. Neurosci. 35, 4258-4267.

Chen, C.F., Kreutz-Delgado, K., Sereno, M.I., Huang, R.S., 2017. Validation of periodic fMRI signals in response to wearable tactile stimulation. NeuroImage 150, 99-111.

Huang, R.S., Chen, C.F., Sereno, M.I., 2017. Mapping the complex topological organization of the human parietal face area. NeuroImage 163, 459-470.

Huang, R.S., Chen, C.F., Sereno, M.I., 2018. Spatiotemporal integration of looming visual and tactile stimuli near the face. Hum. Brain Mapp.

Chen, C.F., Kreutz-Delgado, K., Sereno, M.I., Huang, R.S., *in preparation*. Unraveling the spatiotemporal brain dynamics during a reach-to-eat task.

ABSTRACT OF THE DISSERTATION

Modelling the Phase Angle in Periodic fMRI Signals

by

Chingfu Chen

Doctor of Philosophy in

Electrical Engineering (Intelligent Systems, Robotics, and Control)

University of California, San Diego, 2018

Professor Kenneth Kreutz-Delgado, Chair

The human sensorimotor cortex contains topologically organized maps of the body and movements, usually referred to as Penfield's homunculus. The initial homun-

cular map was depicted using electrical stimulation in patients undergoing brain surgery. For the last 25 years, noninvasive functional magnetic resonance imaging (fMRI) has allowed researchers to map brain organization and function with high spatial resolution (on the order of millimeters). However, less research has been conducted to model the temporal dynamics of fMRI for its low temporal resolution (on the order of seconds). To map topological organization in visual, auditory, and sensorimotor cortices, the phase-encoded paradigm uses time delays in periodic fMRI signals to encode and decode the representations of different brain regions. Phase-encoded fMRI data are typically analyzed by Fourier transform, and an overall signal-to-noise ratio and a single phase of periodic signals are estimated from the entire time series. However, this method cannot fully characterize the temporal dynamics and stability of periodic signals and phases.

This dissertation includes three fMRI studies that aim to map the cortical representations of body parts (face and hand) and unravel the spatiotemporal brain dynamics during a reach-to-eat task. I proposed a data processing pipeline that uses independent component analysis to separate periodic noise from periodic signals, and use time-frequency analysis and circular statistics to model the spread of phase angle of fMRI time series and determine the stability of periodic signals. These analyses provide additional statistical measures, not obtainable using conventional linear methods, to validate

the observed periodic fMRI signals. These methods are fundamental steps to construct a more accurate and comprehensive functional brain atlas of the human sensorimotor cortex.

1 Introduction

1.1 Background of human brain mapping using fMRI

The human visual cortex contains retinotopic areas, such as V1, V2, and V3. The topological organization of neurons in each retinotopic area preserves the spatial relationships between photoreceptors on the retina. To map the area V1, for example, a ring of flashing checkerboards that expands from the central fixation and outward activates corresponding cortical representations from the fovea to the periphery (Engel, 1994).

The human visual cortex contains retinotopic areas, such as V1, V2, and V3. The topological organization of neurons in each retinotopic area preserves the spatial relationships between photoreceptors on the retina. To map the area V1, for example, a ring of flashing checkerboards that expands from the central fixation and outward activates corresponding cortical representations from the fovea to the periphery (Engel, 1994).

Similar to the visual cortex, the sensorimotor cortex contains topologically organized maps of the body, often referred to as the Penfield's Homunculus. The initial homuncular maps were depicted using electrical stimulation in patients undergoing brain surgery (Penfield and Boldrey, 1937). Recently, noninvasive fMRI has allowed re-

searchers to refine these maps with high spatial resolution on the order of millimeters (Chen et al., 2017; Huang and Sereno, 2007; Huang et al, 2012, 2017; Sereno and Huang, 2006).

In most somatosensory fMRI experiments, the representations of different body parts in sensorimotor cortex were mapped by manual stimulation. It is challenging to deliver tactile stimuli with consistent intensity, timing, and spatial precision. To date, only a few body parts have been mapped in humans. In recent years, computer-controlled stimulation systems have been developed to deliver high-density stimuli within and across body parts, which allow the Penfield's homunculus to be refined with high precision (Huang and Sereno, 2007; Huang et al, 2012).

1.2 Basic Principles of MRI and

1.2.1 The structure of an MRI scanner

An MRI scanner consists of a superconductive magnet that creates a strong, static magnetic field ($\mathbf{B}_0$ field; the main field), several radiofrequency (RF) coils that create a small varying magnetic field ($\mathbf{B}_1$ field) and/or receive the free induction decay (FID) signals from body tissue, and three gradient coils (x, y, z direction) that encode the spatial location in the scanner by varying the local magnetic field (Nishimura, 2010). The $\mathbf{B}_0$ field, e.g., 3 Tesla (T), is always present regardless of whether a subject is being scanned or not. In the MRI scanner, the $\mathbf{B}_0$ field is along the z direction, and the $\mathbf{B}_1$ field traverses on the x-y plane (Fig. 1.1, left panel). Note that these axes are not the same as those in the coordinate system in the human brain.

1.2.2 Basic imaging principles of MRI

A charged particle spins and creates a small magnetic field (Fig. 1.1, center panel). When an external magnetic field is applied, two magnetic fields interfere with each other and the particle precesses in the external field (Fig. 1.1, right panel) at the Larmor (resonance) frequency $\boldsymbol{\omega} = \gamma \mathbf{B}$, where γ is the gyromagnetic ratio varying from particles, and $\mathbf{B}$ is the external magnetic field. For the proton, the most abundant particle in the

human body, $\frac{\gamma}{2\pi} \approx 42.58$ MHz/T (Nishimura, 2010); hence, a proton precesses at ~127.75 MHz in a 3 T MRI scanner.

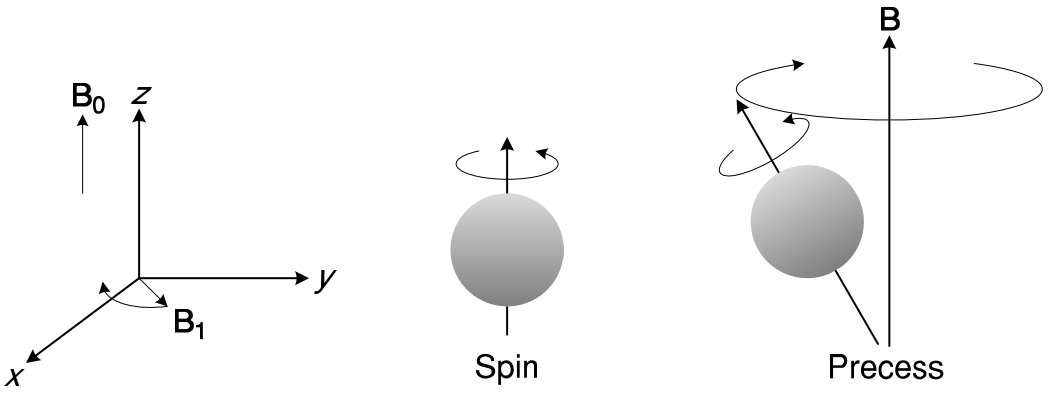

Fig. 1.1: Direction of magnetic fields and spin/precession of a charged particle. Left - the direction of $\mathbf{B}_0$ and $\mathbf{B}_1$ fields; center - the spin of a charged particle; right - a charged particle precessing in a magnetic field. The arrow around the magnetic field **B** indicates direction of precession.

In the MRI scanner, if a very small perturbation ($\mathbf{B}_1$ field) is added to the main field, $\mathbf{B}_0$, the particle is tipped off toward the x-y plane. Note that the $\mathbf{B}_1$ field also adds energy to the particle ("excitation"). When the $\mathbf{B}_1$ field is off, the particle returns to its original equilibrium (the state before excitation) and releases the absorbed energy by emitting the FID signal (Figs. 1.2 and 1.3). If the $\mathbf{B}_1$ field varies at the Larmor frequency ("on resonance excitation"), the FID signal can be received by the RF coils. Since the gradient coils change the local magnetic field and thus affect the local precessing frequency, the frequencies and phase angles from FID signals at different locations are not the same (Nishimura, 2010).

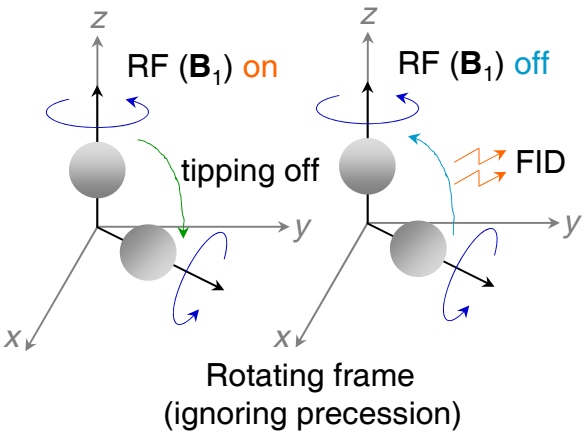

Fig. 1.2: Excitation of a charged particle.

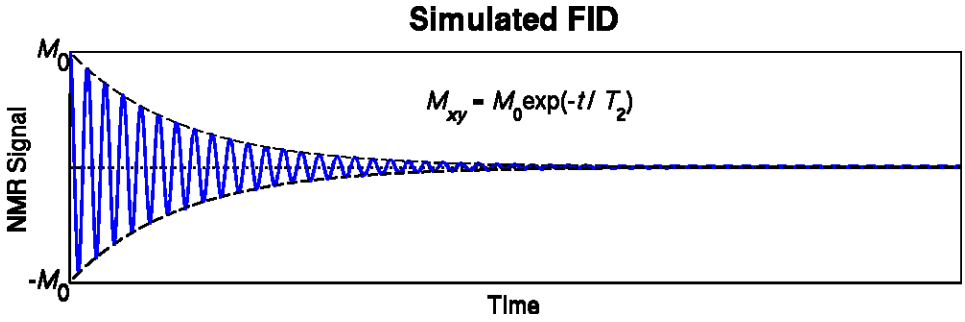

Fig. 1.3: A simulated FID signal.

The state before a particle being excited is the equilibrium, which is a lower energy state of this particle. Even in the equilibrium, this particle is still subject to magnetization from the main field (**B**$_0$ field). Let the magnetization be M_0. In the on resonance excitation, the **B**$_1$ field induces another magnetization on the xy-plane. Once the **B**$_1$ field is off, the magnetization along the z-axis M_z and on the xy-plane M_{xy} return to their equilibrium and can be expressed by (Nishimura, 2010):

$$M_z(t) = M_0\left[1-\exp\left(-\frac{t}{T_1}\right)\right], \tag{1.1}$$

and

$$M_{xy}(t) = M_0 \exp\left(-\frac{t}{T_2}\right). \tag{1.2}$$

T_1 and T_2 are time constants, and their values differ from types of tissue in the same strength of magnetic field. When $t \to \infty$, $M_z \to M_0$ and $M_{xy} \to 0$.

Let $\rho(x, y)$ be the proton density of a type of tissue at location (x, y). For a type of tissue, the magnetization during equilibrium M_0 is in proportion to $\rho(x, y)$. After an on resonance excitation, the image intensity can be represented as (Nishimura, 2010; a detailed explanation of adjusting T_2 can be found in this reference):

$$I(x, y) = \rho(x, y)\left[1 - \exp\left(\frac{-TR}{T_1}\right)\right]\exp\left(\frac{-TE}{T_2}\right), \tag{1.3}$$

where TR is the repetition time, the time between two excitation pulses, and TE is the echo time, the time from the excitation pulse to the center of an acquisition window. In Eq. (1.3), if the TE is much shorter than T_2, the resulting image is a T_1-weighted image; if the TR is much longer than T_1, the resulting image is a T_2-weighted image. A proton density-weighted image can be obtained by setting a very long TR with a very short TE. For example, in a T_1-weighted image (right panel in Fig. 1.4), the image intensities of different tissues depend on their T_1 and proton density.

An MRI image can be reconstructed from the 2-D spatial frequency domain, also known as the *k*-space. Locations in the *k*-space are encoded by the frequency and

phase information in the FID signal. The center of the *k*-space reflects the DC component of a physical image (Fig. 1.4, left panel). The physical image (Fig. 1.4, right panel) can be reconstructed by taking the 2-D inverse Fourier transform on the *k*-space image.

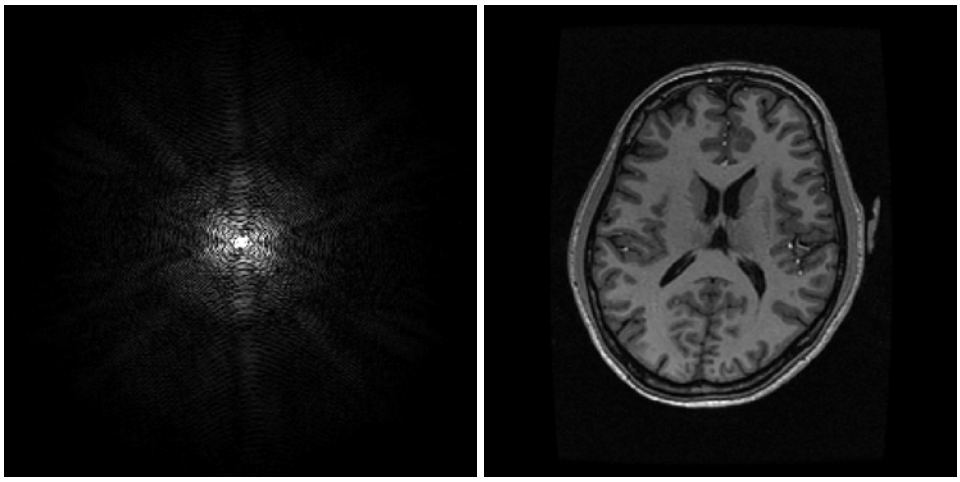

Fig. 1.4: The *k*-space and physical images. The physical image (right) can be reconstructed by taking the inverse Fourier transform on the *k*-space image.

Let f_x be the width of a physical image, or the field of view (FOV) along the x-direction, and δ_x be the spatial resolution along the same direction. If the size of the *k*-space along the *kx* direction is $2k_{xm}$ and the resolution along the *kx* direction is Δk_x, to reconstruct the image without aliasing, the following requirements must be met (Nishimura, 2010):

$$\frac{1}{\delta_x} = 2k_{xm} \quad \text{and} \quad \frac{1}{\Delta k_x} \geq f_x . \tag{1.4}$$

The size and resolution along the *ky* direction can be obtained by using Eq. (1.4).

The x- and y-directions of an image can be reconstructed from the phase and frequency information of the FID signal. To decide the location along the z-direction, it is

possible to excite only the part of interest (a slice) by a proper slice-selection pulse. Finally, a 3-D image can be acquired by exciting all possible locations along the z-direction sequentially (Nishimura, 2010). The basic element of a 3-D volume in the scanned region is a voxel (a small cube).

1.3 Basic Principles of fMRI

Functional brain imaging is achieved by direct or indirect measures of neural activities. Electroencephalography (EEG) and magnetoencephalography (MEG) directly measure neural activities from the cortical surface and have better temporal resolution. Functional magnetic resonance imaging (fMRI) and positron emission tomography (PET) indirectly measure neural activities from metabolic changes in the blood. Since it takes time to convert the blood sugar to energy, the temporal resolution is inferior (Buxton, 2009).

1.3.1 Background of fMRI

fMRI is a non-invasive functional brain imaging technique that measures blood-oxygen-level-depend (BOLD) signal. The BOLD time series is the change in blood oxygen level in response to stimuli or tasks. An fMRI dataset contains 4-D data (3-D volume + time), where the spatial resolution is about one millimeter and the temporal resolution is about one second. The typical dimension of a voxel is about 2-3 mm in x-, y-, and z-directions. Although the size of a voxel is quite large in comparison to the size of a neuron, fMRI is still capable of finding the function of the brain regions (Buxton, 2009). A typical BOLD signal includes an initial dip, an overshoot in response to the stimulus or

task, and a post-stimulus undershoot. The initial dip may not be always present, but the undershoot usually occurs (Buxton, 2013). For a sustained stimulus or task sustains, the overshoot becomes a plateau.

The first fMRI experiment was conducted in 1990 with anesthetized mice. Researchers discovered the change in local magnetic susceptibility when the oxygen level in the inhaled gas changed (Ogawa et al., 1990). The first human fMRI experiment was performed in 1991. In the experiment, subjects received photic stimuli that switched on and off periodically. Changes in signal intensity in response to the on/off periods of the stimuli were found in the primary visual cortex. Similar results were observed in the primary motor cortex when the subjects performed the hand-squeezing task (Kwong et al., 1992). Since then, fMRI become a prevalent tool for noninvasive human functional brain imaging.

1.3.2 Physiological aspects of fMRI

Hemoglobin is the protein in a red blood cell that carries oxygen. When oxyhemoglobin (hemoglobin binding with oxygen) releases oxygen to the tissue and becomes deoxyhemoglobin (hemoglobin not binding with oxygen), the magnet field is distorted and thus the MR signal decreases. When the neural activity increases, glucose metabo-

lism in tissue also increases and more oxyhemoglobin becomes deoxyhemoglobin. However, the oxygen reserve in the brain is very low. During neural activities, the cerebral blood flow increases much more to provide an abundant supply of oxyhemoglobin. Hence, more oxyhemoglobin is transported to the blood vessels near the neurons, and thus the oxygen level in the blood increase. Therefore, stronger BOLD response is correlated with increasing neural activity (Buxton, 2009, 2010).

1.3.3 Experimental designs

Block design and event-related design are the two prevalent types of designs for fMRI experiments. A block design experiment consists of “on” and “off” blocks. Each block lasts for several or even over 10 seconds. In an “on” block, the same stimulus is delivered to the subject repeatedly, or the subject performs the same task repeatedly. There is no stimulus or task in an “off” block (Fig. 1.5A). It is possible there are several types of “on” blocks in an fMRI experiment, but in each type of “on” block, only one type of stimulus (task) is delivered (performed). In an experiment using event-related design, a stimulus/task (“event”) is delivered/performed briefly, and the next event occurs after the BOLD response returns to its baseline (usually around 10 seconds) to prevent ambiguity (Fig. 1.5B). Each “event” in an event-related experiment can be regarded as an

"on" block in a block-design experiment but with much shorter duration (Buxton, 2009).

The BOLD response is usually regarded as the convolution of an underlying hemodynamic response function (HRF) β with the stimulus $\mathbf{X}$, known as the "linear systems assumption" (Boynton et al., 2012). Given this assumption, a general linear model (GLM) is usually applied to find the underlying HRF which "best" explains the observed fMRI time series corresponding to the experimental design. In the GLM model $\mathbf{y} = \mathbf{X}\beta$, $\mathbf{y}$ is the observed fMRI time series of a voxel, $\mathbf{X}$ is the design matrix built up from the stimuli, and β is the HRF of interest. The estimated HRF is the minimum-norm least-squares solution of the inverse problem associated with the GLM model.

In a "phase-encoded" (also known as "traveling wave" design, Fig. 1.5C) (Engel, 2012), the same stimulus is periodically delivered to sequential locations in the retina or on the body surface. Under the linear systems assumption, periodic stimulation delivered to the same location results in periodic BOLD signals at the stimulus frequency, which is defined as the total number of cycles per scan (cps). Within each stimulation cycle, different locations receive the same stimulus with different delays (Fig. 1.5C). The Fourier transform is widely used for analyzing the fMRI time series acquired from phase-encoded experiments, as detailed in Section 1.4.1. The information of stimulus locations (e.g., eccentricity) can be encoded/decoded by the phase angle (delay) of pe-

riodic fMRI time series at the stimulus frequency (Fig. 1.6). The phase-encoded design has been widely used for mapping the visual, auditory, and sensorimotor cortices.

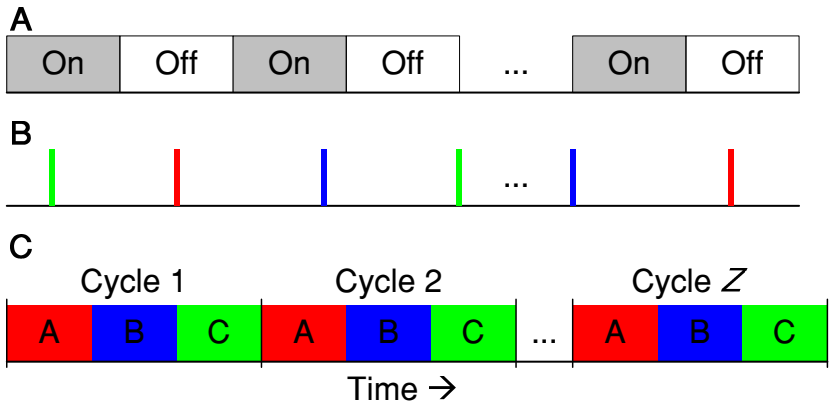

Fig. 1.5: fMRI Experimental Designs. (**A**): Example of a block design experiment. (**B**): Example of an event-related design experiment. (**C**): Example of a phase-encoded design experiment with two stimuli. In (C), A, B and C represent the same stimulus at different locations (delays).

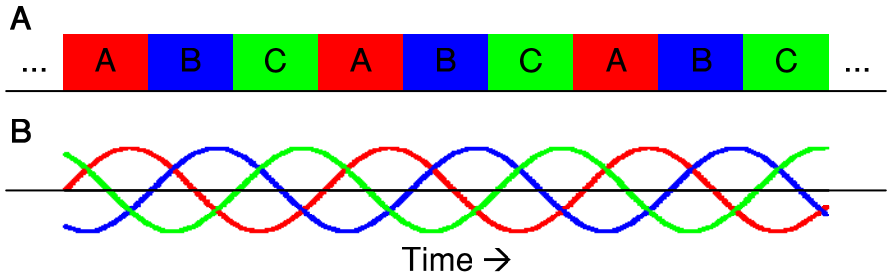

Fig. 1.6: The expected fMRI signals in a phase-encoded design experiment. The sinusoid waves here are to illustrate the relation (in time) between the stimuli and the expected fMRI signal. (**A**): The middle section of an example phase-encoded design experiment. (**B**): The expected fMRI time series from voxels in response to represent the same stimulus at different locations (delays).

1.4 Linear analysis of periodic fMRI time series

1.4.1 Fourier transform

In a phase-encoded design experiment, periodic BOLD signals in response to periodic stimulation are expected under the linear systems assumption. To extract periodic signals, a Fourier transform is applied to the acquired fMRI time series (length: T):

$$X(\omega) = \sum_{t=1}^{T} x(t)\exp(-j\omega t) = |X(t)|\exp(j\theta), \qquad (1.5)$$

where $x(t)$ is the fMRI time series from a voxel. If ω is the stimulus frequency ω_s, θ is the phase angle corresponding the delay in activation due to the stimulus.

Let $y(t)$ be a sinusoid signal and $Y(\omega)$ be its frequency-domain representation obtained using Eq. (1.5). If $y_1(t) = y(t-\phi_1)$ and $y_2(t) = y(t-\phi_2)$, $Y_1(\omega) = \exp(-j\phi_1)\cdot Y(\omega)$ and $Y_2(\omega) = \exp(-j\phi_2)\cdot Y(\omega)$.

Assume a voxel only responds to stimulating only one location. Let $x_1(t)$ and $x_2(t)$ be two fMRI time series from two different voxels that respond to stimuli at two different locations. The Fourier transforms of $x_1(t)$ and $x_2(t)$ yield two different phase angles, θ_1 and θ_2, of periodic signals at the stimulus frequency. Therefore, it is possible to find the stimulated location a voxel in response to by finding the phase angle in the signal. It is evident that precisely estimating the phase angle of the fMRI time series from each voxel is crucial in such phase-encoded experiments.

The *F*-statistic can be used to determine whether the periodic activation of a voxel is significant in comparing to the background non-stimulus-driven background activity of measured fMRI signals. Let ω_s be the set of stimulus frequency and ω_n be the set of other frequencies (defined as "noise"). ω_s may include the second and third harmonics of stimulus frequency since the few number of time samples of a fMRI time series. Assume ω_s and ω_n contain y_s and y_n frequencies respectively. Let dfs and dfn be the degrees of freedom of the signal and noise, which are respectively defined as $dfs = 2y_s$ and $dfn = 2y_n$ (Dobie and Wilson, 1996). Hence, an *F*-statistic can be obtained by:

$$F = \frac{\frac{1}{dfs}\sum_{\omega\in\omega_s}|X(\omega)|^2}{\frac{1}{dfn}\sum_{\omega\in\omega_n}|X(\omega)|^2}, \tag{1.6}$$

where $|X(\omega)|$ can be obtained from Eq. (1.5). Eq. (1.6) is essentially a normalized SNR. A *p*-value can be further estimated from the $F_{(dfs,\,dfn)}$ distribution. A smaller *p*-value indicates a larger *F*-value and a higher SNR of the signal.

1.4.2 Limitations of linear analysis

The *F*-statistic is an overall measure that estimates how strong the periodic signal is in the entire fMRI time series of a voxel. However, this measure has some limita-

tions. For example, a time series containing sustained authentic periodic signals embedded in strong noise and another time series containing strong partial periodic signals may have comparable *F*-values. Therefore, the *F*-value alone cannot reveal the stability of different periodic activations.

In addition to neurons, a voxel may contain other tissues, such as blood vessels, fat, and water. The non-neuron tissue will reduce the overall fMRI signal measured in this voxel and lower the statistical significance. For somatotopic mapping using fMRI, the general goal is to map the larger extent of brain regions in response to the stimuli or tasks. It is reasonable to choose a moderate statistical threshold in order to outline the boundaries rather than the peaks of these regions (Chen, 2017). Convention linear methods apply Fourier transform to the fMRI time series and obtain an overall SNR (*F*-statistic) and a phase angle of periodic signals at the stimulus frequency. These single measures are insufficient to fully characterize the detailed temporal profile and stability of periodic signals.

In the dissertation, I propose a novel data processing pipeline that uses spatial independent component analysis (ICA), time-frequency analysis, and circular statistics to validate the stability of periodic fMRI signals. Spatial ICA separates periodic noise from periodic signals to obtain a “clean” fMRI dataset (detailed in Chapter 3); time-

frequency analysis obtains the trend in SNR and phase angles of a fMRI time series (detailed in Chapters 2 and 3); and circular statistics models the spread of phase angles to provide additional measures for selecting voxel or regions of interest (ROIs) (detailed in Section 1.5). These analyses provide additional statistical measures, not obtainable using conventional linear methods, to validate the observed periodic fMRI signals. These methods are fundamental steps to construct a more accurate and comprehensive functional brain atlas of the human sensorimotor cortex.

1.5 Introduction to Circular Statistics

Circular statistics, also known as directional statistics, is a field of statistics focusing on data with intrinsic periodicity. Possible applications include geology, meteorology, biology, astronomy, physics, image analysis, medicine, and other fields with periodic data. (Fisher, 1993; Mardia, 2000).

1.5.1 A toy example

In this section, all angles are presented in degrees.

Given a set of three angles, $\Theta = \{\theta_1 = 10°, \theta_2 = 20°, \theta_3 = 330°\}$, one can find its mean direction (mean angle), $\bar{\theta}$ by computing the direct mean:

$$\bar{\theta} = \frac{1}{3}\sum_{i=1}^{3}\theta_i = \frac{10° + 20° + 330°}{3} = 120°.$$

Since $\theta_3 = 330° = -30°$, the mean direction can also be computed by:

$$\bar{\theta} = \frac{1}{3}\sum_{i=1}^{3}\theta_i = \frac{10° + 20° + (-30°)}{3} = 0°.$$

Further, for any angle θ and any integer k, $\theta = \theta + k \cdot 360°$. It is possible to convert the set Θ into $\Theta = \{\theta_1 = 10° + k_1 \cdot 360°, \theta_2 = 20° + k_2 \cdot 360°, \theta_3 = 330° + k_3 \cdot 360°\}$ (k_1, k_2, and k_3 are integers) and the mean angle would be $\bar{\theta} = 120°(k_1 + k_2 + k_3 + 1)$. The wrap-around issue remains even if the range of the angles is restricted to an interval with a proper range: if $\theta_i \in [-180° \quad 180°) \quad \forall i$, the mean angle of $\theta_4 = -179°$ and $\theta_5 = 179°$ would be

$0°$. Therefore, the resulting mean angles $\bar{\theta}$ may not be unique or properly explain the data.

To reflect the fact that the angles are only defined modulo 360°, they can be put on the unit circle (Fig. 1.7) by $z_i = \exp(j\theta_i)$, $j = \sqrt{-1}$ to eliminate the ambiguity. The mean direction can be obtained by averaging of these three complex numbers. Hence, to calculate the mean direction $\bar{\theta}$ for Θ in the toy example, one can

1. Convert the angles into the unit-length complex numbers:

   $\theta_1 = 10°$ ➔ $z_1 = \exp(j10°)$

   $\theta_2 = 20°$ ➔ $z_2 = \exp(j20°)$

   $\theta_3 = 330°$ ➔ $z_3 = \exp(j330°)$, and

2. Find the mean of the complex numbers:

$$\bar{z} = \frac{1}{3}\sum_{i=1}^{3} z_i = \frac{z_1 + z_2 + z_3}{3} = 0.9302\exp(j0.3217°) = \bar{r}\exp(j\bar{\theta}).$$

Therefore, the mean direction would be $\bar{\theta} = 0.3217°$. Since the corresponding complex number of an angle is unique, the sum of these complex numbers is also unique. The above method eliminates the ambiguity in directly computing the mean of the angles and obtains a unique estimate of the mean angle.

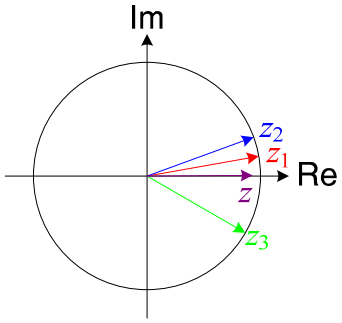

Fig. 1.7: The three angles and the corresponding complex numbers on the unit circle.

1.5.2 Summary Statistics

Given a set of angles $\Theta = \{\theta_n\}_{n=1}^{N} = \{\theta_1, \ldots, \theta_n\}$. The mean direction $\bar{\theta}$ can be reasonably obtained by first converting the angles to the corresponding unit-length complex numbers $z_n = \exp(j\theta_n)$, $n = 1, \ldots, N$, and calculating the mean of these numbers (Fisher, 1993; Jammalamadaka and SenGupta, 2001; Mardia and Jupp, 2000):

$$\bar{z} = \frac{1}{N}\sum_{n=1}^{N} z_n = \bar{r}\exp(j\bar{\theta}), \tag{1.7}$$

where $\bar{r}$ is the resultant length and $0 \le \bar{r} \le 1$. Eq. (1.7) is the first sample moment of the angles, and the p^{th} sample moments can be obtained in a similar way (Fisher, 1993; Jammalamadaka and SenGupta, 2001; Mardia and Jupp, 2000):

$$\bar{z}_p = \frac{1}{N}\sum_{n=1}^{N} z_n^p = \bar{r}_p \exp(j\bar{\theta}_p). \tag{1.8}$$

For phase-encoded fMRI data, we aim to find the mean angles of non-unit-length complex numbers. Therefore, Eq. (1.8) is modified into (Grabska-Barwińska et al., 2012; Levick and Thibos, 1982; Ringach et al., 2002):

$$\bar{z}_p = \frac{\sum_{n=1}^{N} z_n^p}{\sum_{n=1}^{N} |z_n|^p} = \bar{r}_p \exp\left(j\bar{\theta}_p\right). \tag{1.9}$$

If the lengths of these complex numbers are equal, i.e., $|z_1| = \ldots = |z_N|$, the results are the same as those obtained from Eq. (1.8).

The circular variance, υ, is defined as (Fisher, 1993; Mardia and Jupp, 2000):

$$\upsilon = 1 - \bar{r}, \tag{1.10}$$

and the circular standard deviation, ς, is defined as:

$$\varsigma = \sqrt{-2\log\left(\bar{r}\right)} = \sqrt{-2\log\left(1-\upsilon\right)}, \tag{1.11}$$

in which $\log(\cdot)$ is the natural logarithm. Note that in usual, $\varsigma \neq \sqrt{\upsilon}$. The motivation of defining circular standard distribution in this way is detailed in Section 3.4.2 in Mardia and Jupp, 2000.

Since the circular variance and circular standard deviation are the direct interpretations of the resultant length of the angular data, $\bar{r}$, and may not sufficiently describe the data (Fisher, 1993), it is also useful to consider the circular dispersion δ, defined as (Fisher, 1993; Mardia and Jupp, 2000):

$$\delta = \frac{1-\bar{r}_2}{2\bar{r}}. \tag{1.12}$$

The circular variance υ takes value in $[0,1]$, and the circular standard deviation ς and the circular dispersion δ take values in $[0,\infty)$. If the angles in an angular dataset

are more concentrate, the values of υ, ς, and δ are smaller.

1.5.3 Association between angles

The associations between two sets of angular data can be estimated using the circular correlation coefficient, ρ. Given two angular datasets $\Theta^{(1)} = \left\{\theta_n^{(1)}\right\}_{n=1}^{N} = \left\{\theta_1^{(1)}, \ldots, \theta_N^{(1)}\right\}$ (with mean direction $\overline{\theta}^{(1)}$) and $\Theta^{(2)} = \left\{\theta_n^{(2)}\right\}_{n=1}^{N} = \left\{\theta_1^{(2)}, \ldots, \theta_N^{(2)}\right\}$ (with mean direction $\overline{\theta}^{(2)}$), the sample circular correlation coefficient, $\rho^{(1)(2)}$, is defined as: (Jammalamadaka and SenGupta, 2001)

$$\rho^{(1)(2)} = \frac{\sum_{n=1}^{N}\left[\sin\left(\theta_n^{(1)} - \overline{\theta}^{(1)}\right)\sin\left(\theta_n^{(2)} - \overline{\theta}^{(2)}\right)\right]}{\sqrt{\left[\sum_{n=1}^{N}\sin^2\left(\theta_n^{(1)} - \overline{\theta}^{(1)}\right)\right]\left[\sum_{n=1}^{N}\sin^2\left(\theta_n^{(2)} - \overline{\theta}^{(2)}\right)\right]}}. \tag{1.13}$$

The circular correlation coefficient ranges from -1 to 1, inclusive.

In the linear statistics, the *p*-value of correlation coefficient is accessed to reflect the degree of association of two random variables. Similarly, in circular statistics, the *p*-value of the circular correlation coefficient $\rho^{(1)(2)}$ can be estimated from the distribution of $\sqrt{N}\frac{\sqrt{\hat{\lambda}_{20}\hat{\lambda}_{02}}}{\sqrt{\hat{\lambda}_{22}}}$ to reflect the association between two circular random variables (Jammalamadaka and SenGupta, 2001), where

$$\hat{\lambda}_{ij} = \frac{1}{N}\sum_{n=1}^{N}\left[\sin^i\left(\theta_n^{(1)} - \overline{\theta}^{(1)}\right)\sin^j\left(\theta_n^{(2)} - \overline{\theta}^{(2)}\right)\right]. \tag{1.14}$$

Since $\sqrt{N}\frac{\sqrt{\hat{\lambda}_{20}\hat{\lambda}_{02}}}{\sqrt{\hat{\lambda}_{22}}}\rho^{(1)(2)} \sim N(0,1)$ when N is large, the significance level of $\rho^{(1)(2)}$ can be verified under the null hypothesis $\rho^{(1)(2)} = 0$. If the two datasets are independent, $\rho^{(1)(2)} = 0$.

1.5.4 Examples of Circular Probability Distributions

Note: the angles in this section are described in radians.

The circular uniform distribution is the most basic distribution in circular statistics (Mardia and Jupp, 2000). This distribution is usually regarded as the null model against other alternative models such as unimodal or multimodal model (Fisher, 1993; Mardia and Jupp, 2000). For a circular random variable $\Theta \in [0, 2\pi)$, the probability density function of the circular uniform distribution is (Fisher, 1993; Jammalamadaka and SenGupta, 2001; Mardia and Jupp, 2000):

$$f(\Theta = \theta) = \frac{1}{2\pi}, \tag{1.15}$$

and the cumulative distribution function between two angles a and b ($a \le b \le a + 2\pi$) can be calculated by integrating the probability density function:

$$P(a \le \Theta \le b) = \int_a^b f(\Theta = \theta)d\theta = \int_a^b \frac{1}{2\pi} d\theta = \frac{b-a}{2\pi}. \tag{1.16}$$

The mean direction of the circular uniform distribution is undefined. The resultant

length is 0, the circular variance is 1, and both circular standard deviation and circular dispersion are ∞.

The von Mises distribution, $VM(\phi, \kappa)$, is the most common unimodal distribution in circular statistics. It is the circular analogy of the normal distribution. For a circular random variable $\Theta \in [0, 2\pi)$, the probability density function of a $VM(\phi, \kappa)$ distribution is (Fisher, 1993; Jammalamadaka and SenGupta, 2001; Mardia and Jupp, 2000):

$$f(\Theta = \theta; \phi, \kappa) = \frac{1}{2\pi I_0(\kappa)} \exp[\kappa \cos(\theta - \phi)], \tag{1.17}$$

where ϕ is the mean direction, $\kappa \geq 0$ is the concentration parameter (analogues to the inverse of the variance in the normal distribution), and I_0 is the modified Bessel function of order 0. When $\kappa = 0$, the von Mises distribution becomes a circular uniform distribution (Eq. (1.15)); when $\kappa \to \infty$, it is a point distribution at the mean direction of the von Mises distribution. Fig. 1.8 shows the probability density functions of the $VM(0, \kappa)$ distributions of selected κ. Although the cumulative distribution function of the von Mises distribution can theoretically be found by integrating the probability density function, a closed-form expression for the cumulative distribution function does not exist and must be determined numerically (Fisher, 1993; Jammalamadaka and SenGupta, 2001; Mardia and Jupp, 2000).

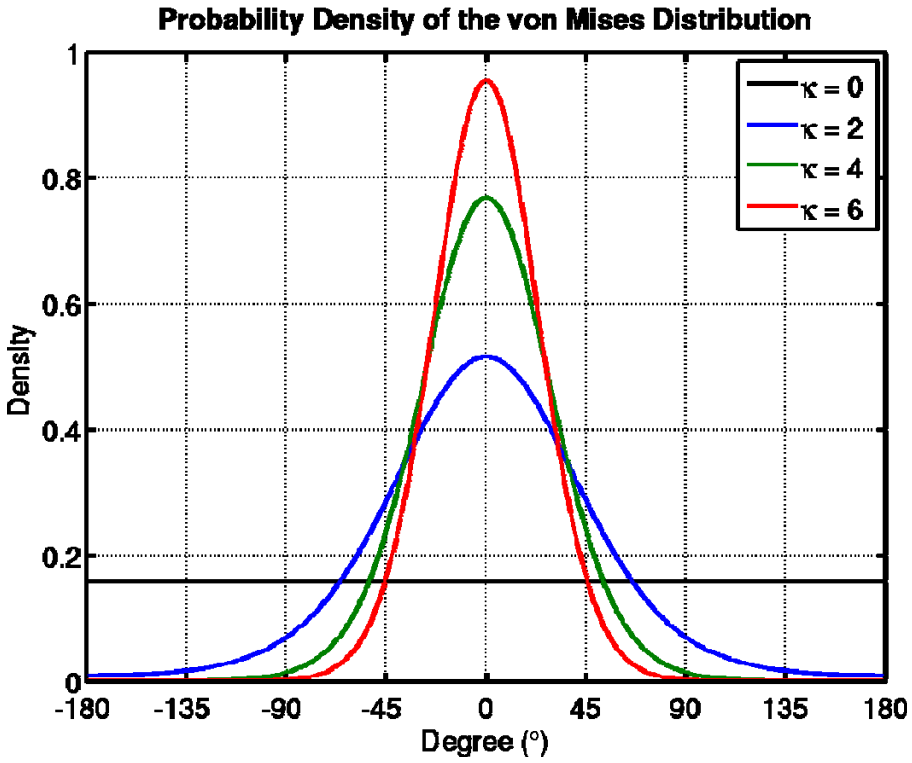

Fig. 1.8: Probability density functions of von Mises distributions of selected κ's.

Let $\Theta = \{\theta_n\}_{n=1}^{N} = \{\theta_1, \ldots, \theta_n\}$ be a set of independent samples drawn from a $VM(\phi, \kappa)$ distribution. The joint probability density function of Θ is:

$$f(\Theta = \theta_1, \ldots, \Theta = \theta_N; \phi, \kappa) = \left[\frac{1}{2\pi I_0(\kappa)}\right]^N \exp\left[\kappa \sum_{n=1}^{N} \cos(\theta_n - \phi)\right]. \qquad (1.18)$$

The parameters ϕ and κ can be estimated by maximum likelihood estimation (Mardia and Jupp, 2000), yielding

$$\hat{\phi} = \bar{\theta} \qquad \text{and} \qquad \hat{\kappa} = A^{-1}(\bar{r}), \qquad (1.19)$$

in which $\bar{\theta}$ and $\bar{r}$ are the mean direction and the resultant length of the dataset respectively, and $A(\cdot)$ is a one-to-one mapping (in the range of $\bar{r}$).

In standard linear statistics, if $X \sim N(\mu, \sigma^2)$, $P(\mu - k\sigma \le X \le \mu + k\sigma)$ is fixed if k

is set to a specific value regardless of the values of μ and σ; e.g., $P(\mu-\sigma \le X \le \mu+\sigma) \approx 0.6827$ independent of the mean and standard deviation. However, if $\Theta \sim VM(\phi, \kappa)$ and ς is the circular standard deviation, the values of $P(\phi - k\varsigma \le \Theta \le \phi + k\varsigma)$ depends on the value of ς. In particular, $P(\phi-\varsigma \le \Theta \le \phi+\varsigma) \approx 0.6827$ is only valid if the concentration parameter κ is not too small, or the distribution is not too disperse (Fisher, 1993). In order to better summarize the circular quantities, it is always possible to find θ_c such that

$$P(\phi - \theta_c \le \Theta \le \phi + \theta_c) = q\,, \tag{1.20}$$

where q is a given probability value (Fisher, 1993). The values of q corresponding to different values of κ and θ_c are listed in Mardia and Jupp, 2000.

1.5.5 Applying circular statistics to periodic fMRI data

For an experiment using the phase-encoded paradigm, the stimuli are presented sequentially in a cycle. If different brain regions react to respond to the same stimulus at different locations, the phase angles of the signals differ in these regions (because the stimulus onsets are staggered in time; see Sections 1.3.3). Circular statistics can be applied to fMRI time series acquired from phase-encoded experiments at three different levels of analysis:

1. Voxel level (Chen et al, 2017, in preparation): Time-frequency analysis is performed on the fMRI time series of a voxel to obtain the phase angles from time to time at the stimulus frequency. Then, circular statistics is used to model the distribution of the phase angles for selecting voxels with stable (low phase jitter) periodic fMRI time series.
2. ROI level: Once the mean phase angles at the stimulus frequency from the voxels in an region of interest (ROI) is obtained, circular statistics can be applied to select voxels with stable fMRI time series (Chen et al, 2017) or compare the association of the phase angles between different stimulation (Huang et al, 2017).
3. Whole-brain level: Circular statistics can be used to select ROIs that responds to different stimuli and model the overall phase angle from the ROIs that respond to the same stimulus (Chen et al, 2017).

Applications of circular statistics on actual fMRI data are detailed in the following chapters.

1.6 References

Boynton, G.M., Engel, S.A., Heeger, D.J., 2012. Linear systems analysis of the fMRI signal. NeuroImage 62:975-984.

Buxton, R.B., 2009. Introduction to Functional Magnetic Resonance Imaging: Principles and Techniques, second ed. Cambridge University Press, Cambridge.

Buxton, R.B., 2010. Interpreting oxygenation-based neuroimaging signals: the importance and the chal-lenge of understanding brain oxygen metabolism. Front. Neuroenergetics 2:8.

Buxton, R.B., 2013. The physics of functional magnetic resonance imaging (fMRI). Rep. Prog. Phys. 76:096601.

Chen, C.F., Kreutz-Delgado, K., Sereno, M.I., Huang, R.S., 2017. Validation of periodic fMRI signals in response to wearable tactile stimulation. NeuroImage 150:99-111.

Dobie, R.A., Wilson, M.J., 1996. A comparison of t test, F test, and coherence methods of detecting steady-state auditory-evoked potentials, distortion-product otoacoustic emissions, or r sinusoids. J. Acoust. Soc. Am. 100, 2236-2246.

Engel, S.A., 2012. The development and use of phase-encoded functional MRI designs. NeuroImage 62:1195-1200.

Engel, S.A., Rumelhart, D.E., Wandell, B.A., Lee, A.T., Glover, G.H., Chichilnisky, E.J., Shadlen, M.N., 1994. fMRI of human visual cortex. Nature 369: 525.

Fisher, N.I., 1993. Statistical Analysis of Circular Data, first ed. Cambridge University Press, Cambridge.

Grabska-Barwińska, A., Ng, B.S., Jancke, D., 2012. Orientation selective or not? - Measuring significance of tuning to a circular parameter. J. Neurosci. Methods 203, 1-9.

Huang, R.S., Chen, C.F., Sereno, M.I., 2017. Mapping the complex topological organi-

zation of the human parietal face area. NeuroImage 163:459-470.

Huang, R.S., Chen, C.F., Tran, A.T., Holstein, K.L., Sereno, M.I., 2012. Mapping multisensory parietal face and body areas in humans. Proc. Natl. Acad. Sci. USA 109:18114-18119.

Huang, R.S., Sereno, M.I., 2007. Dodecapus: An MR-compatible system for somatosensory stimulation. NeuroImage. 34:1060-1073.

Jammalamadaka, S.R., SenGupta, A., 2001. Topics in Circular Statistics. World Scientific Publishing Co., River Edge, New Jersey, USA.

Kwong, K.K., Belliveau, J.W., Chesler, D.A., Goldberg, I.E., Weisskoff, R.M., Poncelet, B.P., Kennedy, D.N., Hoppel, B.E., Cohen, M.S., Turner R., 1992. Dynamic magnetic resonance imaging of human brain activity during primary sensory stimulation. Proc. Natl. Acad. Sci. USA 89:5675-569.

Levick, W.R., Thibos, L.N., 1982. Analysis of orientation bias in cat retina. J. Physiol. 329, 243-261.

Mardia, K.V., Jupp, P.E., 2000. Directional Statistics. John Wiley & Sons, Hoboken, New Jersey, USA.

Nishimura, D.G., 2010. Principles of magnetic resonance imaging.

Ogawa, S., Lee, T.M., Kay, A.R., Tank, D.W., 1990. Brain magnetic resonance imaging with contrast dependent on blood oxygenation. Proc. Natl. Acad. Sci. USA 87:9868-9872.

Penfield, W., Boldrey, E., 1937. Somatic motor and sensory representation in the cerebral cortex of man as studied by electrical stimulation. Brain 60, 389-443.

Ringach D.L., Shapley R.M., Hawken M.J., 2002. Orientation selectivity in macaque V1: diversity and laminar dependence. J. Neurosci. 22, 5639-5651.

Sereno, M.I., Huang, R.S., 2006. A human parietal face area contains aligned head-

centered visual and tactile maps. Nat. Neurosci. 9:1337-1343.

2 Validation of periodic fMRI signals in response to wearable tactile stimulation

Ching-fu Chen[1], Kenneth Kreutz-Delgado[1,2], Martin I. Sereno[3,4], Ruey-Song Huang[2]*

[1]*Department of Electrical and Computer Engineering, University of California, San Diego, La Jolla, CA 92093, USA*

[2]*Institute for Neural Computation, University of California, San Diego, La Jolla, CA 92093, USA*

[3]*Birkbeck/UCL Centre for NeuroImaging (BUCNI), London WC1E 7HX, U.K.*

[4]*Department of Psychology and Neuroimaging Center, San Diego State University, San Diego, CA 92182, USA*

*Correspondence to:
Ruey-Song Huang
Institute for Neural Computation
University of California, San Diego
9500 Gilman Dr. #0559
La Jolla, CA 92093-0559
Phone/fax: (858) 822-5977
email: rhuang@ucsd.edu

This chapter has been published in NeuroImage *Volume 150 (2017), pages 99-111.*

2.0 Abstract

To map cortical representations of the body, we recently developed a wearable technology for automatic tactile stimulation in human functional magnetic resonance imaging (fMRI) experiments. In a two-condition block design experiment, air puffs were delivered to the face and hands periodically. Surface-based regions of interest (S-ROIs) were initially identified by thresholding a linear statistical measure of signal-to-noise ratio of periodic response. Across subjects, S-ROIs were found in the frontal, primary sensorimotor, posterior parietal, insular, temporal, cingulate, and occipital cortices. To validate and differentiate these S-ROIs, we develop a measure of temporal stability of response based on the assumption that a periodic stimulation evokes stable (low-variance) periodic fMRI signals throughout the entire scan. Toward this end, we apply time-frequency analysis to fMRI time series and use circular statistics to characterize the distribution of phase angles for data selection. We then assess the temporal variability of a periodic signal by measuring the path length of its trajectory in the complex plane. Both within and outside the primary sensorimotor cortex, S-ROIs with high temporal variability and deviant phase angles are rejected. A surface-based probabilistic group-average map is constructed for spatial screening of S-ROIs with low to moderate temporal variability in non-sensorimotor regions. Areas commonly activated across sub-

jects are also summarized in the group-average map. In summary, this study demonstrates that analyzing temporal characteristics of the entire fMRI time series is essential for second-level selection and interpretation of S-ROIs initially defined by an overall linear statistical measure.

Keywords: wearable tactile stimulation, human somatotopy, linear systems analysis, time-frequency analysis, signal stability

2.1 Introduction

The human sensorimotor cortex contains somatotopic representations of the body, often referred to as the homunculus map (Penfield and Boldrey, 1937). Noninvasive neuroimaging techniques, such as functional magnetic resonance imaging (fMRI), have been used to map part of the sensorimotor homunculus. Manual touching, rubbing, or brushing is commonly used to stimulate the surface of multiple body parts in fMRI experiments (Disbrow et al., 2000; Eickhoff et al., 2008; Miyamoto et al., 2006). However, it is challenging to manually control the timing, intensity, and extent of tactile stimuli with a consistent level of precision throughout the experiment. Various MR-compatible devices for automatic delivery of electrical, pneumatic, vibrotactile, or mechanical stimulation have been developed (Dresel et al., 2008; Golaszewski et al., 2012; Huang and Sereno, 2007; Servos et al., 1998). To date, several limitations remain in the development of automatic stimulation devices for fMRI experiments: (1) Materials and components must be compatible with the MRI environment; (2) Devices must remain operational under strong static and dynamic magnetic fields and rapidly changing radio frequency pulses; (3) Devices must not interfere with MR image acquisition; (4) Devices must fit in the limited space between the subject and the wall of the scanner bore; and (5) Devices must be set up and torn down quickly to reduce MRI time (cost) and ensure

subject comfort. To overcome some of these limitations, we recently developed a wearable technology for automatic tactile stimulation on multiple body parts in the MRI scanner (Huang et al., 2012). To validate this wearable technology for somatotopic mapping, we used a block-design paradigm in which stimuli were delivered periodically to two alternating body parts (e.g., face vs. hands) during an fMRI experiment.

Linear systems analysis has been used to determine whether the fMRI time series in a voxel contains a periodic signal that is strongly correlated with a periodic stimulus (Boynton et al., 2012; Engel et al., 1994; Sereno et al., 1995). The overall signal-to-noise ratio (SNR) at the stimulus frequency of a time series is assessed by a statistical measure (e.g., *F*- or *t*-statistic). A cluster of voxels with statistical measures higher than a selected threshold is then identified as a region of interest (ROI). Analysis of our somatotopic mapping data has revealed multiple ROIs within and outside the primary somatosensory and motor cortex (S-I and M-I) (Huang and Sereno, 2007; Huang et al., 2012; Sereno and Huang, 2006). However, major challenges arise in selecting and interpreting these ROIs. First, a single statistical measure of SNR only partially illustrates the signal characteristics of a time series. A high statistical measure may result from a high correlation in part of, but not the entire, time series. By contrast, a low statistical measure may result from weak but sustained periodic signals embedded in a noisy

background. Second, most whole-brain fMRI datasets contain isolated and sporadic activation spots (ROIs) that are difficult to interpret, i.e., some may be associated with authentic functional brain activation while some are just false positives. Third, a data-driven approach would be helpful for labeling new somatotopic areas in humans because no generally accepted functional brain atlas can be used as a reference map to validate unknown ROIs, particularly those found outside the primary sensorimotor cortex. For example, several human neuroimaging studies have shown preliminary evidence of somatotopic areas in nonprimary sensorimotor cortex (Dresel et al., 2008; Fink et al., 1997; Huang and Sereno, 2007; Huang et al., 2012; Zlatkina et al., 2016). Taken together, there is a need to further validate and differentiate ROIs by analyzing the temporal characteristics of fMRI signals in each ROI.

In this study, we apply time-frequency analysis to fMRI time series and use circular statistics to characterize the distribution of phase angles within-voxel, within-ROI, and within-subject. We then assess the temporal stability of a periodic signal in each ROI by measuring the path length of its trajectory in the complex plane. A shorter path length generally indicates a more stable periodic signal. To assess inter-subject spatial variability, a surface-based probabilistic group-average map is constructed to further screen ROIs with a low probability of occurrence across subjects. These approaches

take into consideration of fluctuations over the entire fMRI time series as well as the spatial distribution of activation sites on the cortical surface, thereby providing a more comprehensive way to select and interpret ROIs in somatosensory fMRI experiments.

2.2 Materials and Methods

2.2.1 Participants

Two right-handed subjects (ages 21-22; one female; Subjects 1 to 2) with no history of neurological disorders participated in this study. We also included and reanalyzed datasets of fourteen additional subjects (ages 18-30; 8 female; Subjects 3 to 16) from our previous study (Huang et al., 2012). All subjects gave informed consent according to protocols approved by the Human Research Protections Program of the University of California, San Diego (UCSD).

2.2.2 Wearable technology for tactile stimulation

Design concept. We recently developed a wearable technology for full-body tactile stimulation in the MRI scanner (see Figs. 1 and S1 in Huang et al., 2012). The wearable technology consists of a 64-channel pneumatic control system, full-body suits, and multiple modules for selected body parts. The custom-built control hardware (including a portable computer) is located in the console room adjacent to the shielded MRI room and thus its materials and operation would not interfere with MR image acquisition. The stimulus control system takes in compressed air from a cylinder (Praxair UN1002; output: ~60 psi) and delivers air puffs (instantaneous peak pressure on the

skin: ~15-20 psi) to designated body locations underneath the wearable suits or modules via bundles of plastic tubes (25-ft in length; 1/16-in inside diameter). Arrays of quick connectors (Colder Products Company, MN; Part No. SMM01, SMF01) allow researchers to freely select the number of stimulation channels and reconfigure the wearable modules according to the need of different experimental designs (Fig. 2.1). Furthermore, the wearable approach allows stimulation sites to be “pre-wired” to designated locations with high spatial precision, and thus significantly reduces the time for experimental setup.

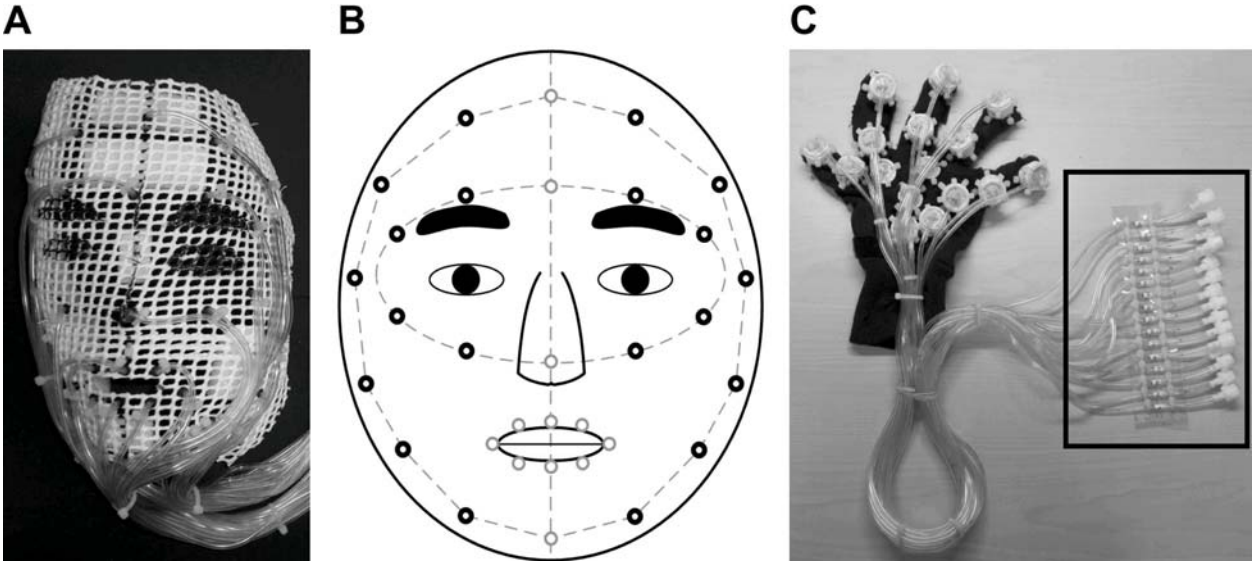

Fig. 2.1: Wearable modules for tactile stimulation in fMRI experiments. (**A**) A custom-molded facial mask embedded with 32 stimulation sites. (**B**) Schematics of 20 facial stimulation sites (thick black circles) used in this study. (**C**) A glove embedded with 16 stimulation sites on the left hand.

Wearable modules. A facial mask was custom molded for each subject using X-LITE thermoplastic materials (Runlite SA, Belgium) (Fig. 2.1A, B). Fiducial points of the

eyebrows, eyes, nose, and lips were marked on the mask during face molding for each subject. Plastic tubes ending with elbow-shaped connectors (right-angle nozzles) at designated locations were tied to the grid (~ 0.5 cm per cell) of the mask. Pieces of polyethylene foam were padded underneath the mask in order to provide soft contact with the face and raise the gap between the nozzles and the skin. Two pairs of cloth gloves embedded with tubes and nozzles were built for stimulation on both hands of male and female subjects. Each glove contains 16 stimulation sites, including two on each finger and six on the palm (Fig. 2.1C).

2.2.3 Experimental design and stimuli

The wearable technology enables stimulation on multiple body parts in the same experiment in order to map as many somatotopic areas as possible using the shortest practical time at an MRI facility. Two or more body parts can be selected in the same scan provided that their cortical representations have little to no overlap, as suggested by previous experiments that mapped a single body part per scan (Huang and Sereno, 2007; Huang et al., 2012). In the current study, a two-condition block-design paradigm was used to map bilateral representations of face and hands in two identical 256-s scans. Each scan consisted of eight cycles of two alternating (periodic) conditions,

where sequences of air puffs (200 ms each) were delivered to 20 locations on the face for 16 s and then to 32 locations across both hands for 16 s (Fig. 2.1). Within each body part, an air puff at the current location was always followed by the next air puff at a different random location without a delay. In each 16-s block, about 4 or 2.5 air puffs were delivered at a randomized interval to each location on the face or hands. These low-rate, randomized stimuli are designed to elicit maximum brain response within each cortical area of body-part representation while minimizing sensory adaptation and habituation during each stimulation block. Subjects closed their eyes during the entire experiment, and they were instructed to covertly attend to the locations of stimuli without making any response.

2.2.4 Experimental setup and data acquisition

Subjects were scanned using an 8-channel head coil in a General Electric (GE) Discovery MR750 3-Tesla scanner at the Center of fMRI at UCSD. The subject lay supine on the scanner bed wearing a mask and a pair of cloth gloves. Quick connectors were used to connect the wearable modules with bundles of tubes that passed through a waveguide and reached the stimulus control system in the console room. Fiducial points marked on the mask were used to precisely align them with the corresponding

points on the subject's face. Tape and Velcro were used to firmly secure some of the stimulation sites on the gloves. To minimize head movements, foam padding was inserted between the mask and the head coil.

Functional images of Subjects 1 and 2 were acquired using single-shot echo-planar imaging (EPI) with parameters: field of view (FOV) = 22.4 cm, repetition time (TR) = 2 s, echo time (TE) = 30.1 ms, flip angle (FA) = 90°, voxel size = 3.5 mm isotropic, in-plane matrix size = 64×64, 38 axial slices, and 128 images per slice (256 s per scan). Two field-mapping scans for distortion correction were acquired using fast low angle shot (FLASH) imaging with parameters: FOV= 22.4 cm, TR = 1 s, TE = 3.5-5.5 ms, FA = 60°, spatial resolution = 3.5 mm isotropic, in-plane matrix size = 64×64, and 38 axial slices. Two sets of high-resolution structural images were acquired using fast spoiled gradient-echo (FSPGR) imaging with parameters: FOV = 25.6 cm, TR = 8.108 ms, TE = 3.172 ms, FA = 8°, voxel size = 1 mm isotropic, in-plane matrix size = 256 × 256, and 160 axial slices. A slightly different set of scanning parameters was used for Subjects 3 to 16 (for details, see SI Methods in Huang et al., 2012).

2.2.5 Image preprocessing

For each subject, two sets of structural images were averaged after precise

manual alignment. The FreeSurfer package (Dale et al., 1999; Fischl et al., 1999) was then used to reconstruct cortical surfaces from the average structural images. Geometric distortions in functional images were corrected using two field-mapping scans and protocols provided by the Center of fMRI at UCSD (http://fmri.ucsd.edu/Howto/3T/fieldmap.html). Distortion-corrected functional images were motion-corrected using the *3dvolreg* tool of the Analysis of Functional NeuroImages (AFNI) package (Cox, 1996). For each voxel, point-wise average was applied to time series of two functional scans. Functional voxels were registered with vertices on the cortical surfaces using a transformation matrix obtained by manually refining the alignment between functional and structural images using FreeSurfer. Only surface-bound voxels that were located within 0-2 mm along the normal of each vertex on the cortical surface were subjected to further analyses. Subsequent data analysis procedures were carried out in MATLAB (MathWorks, Natick, MA), and the results were rendered on inflated cortical surfaces using FreeSurfer.

2.2.6 Linear systems analysis and statistics

Functional MRI data were first analyzed using a linear systems approach commonly used in retinotopic mapping studies (Boynton et al., 2012; Engel et al., 1994;

Sereno et al., 1995). This approach measures periodic fMRI signals in response to periodic sensory stimulation and assesses the statistical significance of an overall SNR from the entire time series. For each voxel, linear trends are first removed from the averaged time series (128 sample points), and a power spectrum (64 bins in 0-63 cycles/scan) is obtained by discrete Fourier transform (DFT):

$$X_m(\omega) = \sum_{t=1}^{T} x_m(t)\exp(-j\omega t) = |X_m(\omega)|\exp[j\theta_m(\omega)], \qquad (2.1)$$

in which $x_m(t)$ is the time series in Voxel m, T is the total sample points, and $X_m(\omega)$, $|X_m(\omega)|$, and $\theta_m(\omega)$ are the complex value, amplitude, and phase angle at frequency ω respectively. The "signal" and "noise" are defined as the component at the stimulus frequency ($\omega_s = 8$ cycles/scan) and the components at remaining frequencies ($\omega_n = 0-63$ cycles/scan; excluding 0-2, 7-9, 15-17, 23-25, and 32 cycles/scan) respectively. For each voxel, an *F*-statistic value (F_m) is obtained by comparing the ratio between the signal energy $|X_m(\omega_s)|^2$ and the sum of noise energy $|X_m(\omega_n)|^2$, and then normalized by their degrees of freedom:

$$F_m = \frac{|X_m(\omega_s)|^2 / df_s}{\left(\sum_{\omega\in\omega_n} |X_m(\omega)|^2\right) / df_n}. \qquad (2.2)$$

A *p*-value is then estimated by considering the degrees of freedom of signal ($df_s = 2$ for real and imaginary parts at the stimulus frequency) and noise ($df_n = 102$ for

the remaining frequencies) in F_m. Voxels with *F*-values exceeding a single threshold ($F_{2,102} = 7.3973$, $p = 0.001$, uncorrected) are selected and rendered on the cortical surfaces (Fig. 2.2A). A 180° offset is applied to the phase angle at the stimulus frequency $\theta_m(\omega_s)$, and then voxels with phase angles in the first and second halves of a cycle are rendered in red (face representations) and green (hand/finger representations) respectively. Detached activation sites (each with a surface area larger than 30 mm^2) on the cortical surface are considered possible representations of the face or hands (fingers), which are semi-automatically labeled as surface-based ROIs (S-ROIs) using FreeSurfer (Fig. 2.2A).

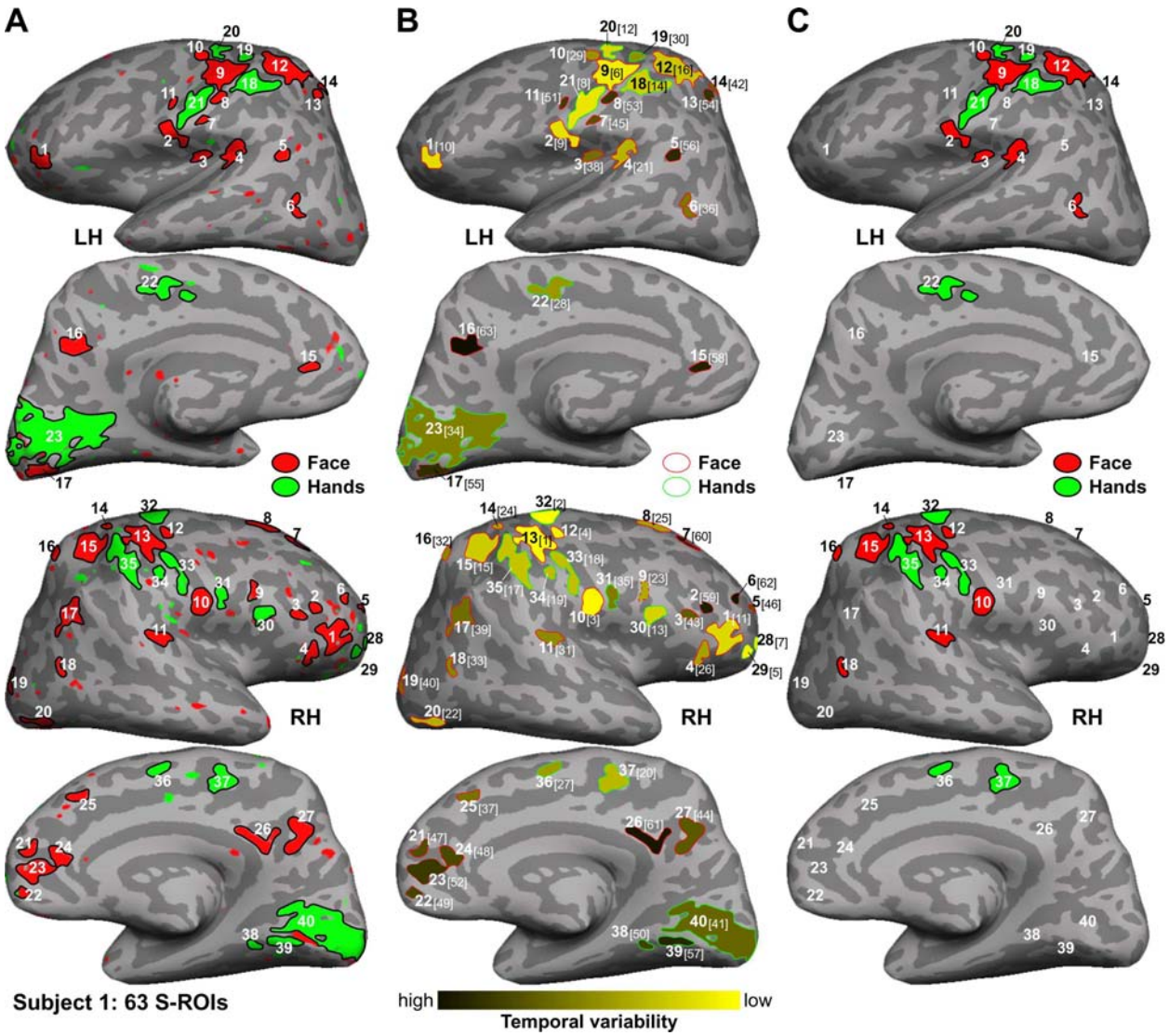

Fig. 2.2: Selection of S-ROIs in response to tactile stimulation on the face or hands in Subject 1. (**A**) Activation maps are thresholded at $p = 0.001$ (uncorrected). Each indexed S-ROI outlined in a black contour has a surface area larger than 30 mm^2. (**B**) S-ROIs sorted by temporal variability. Each number in brackets indicates the rank of S-ROIs between 1 (lowest) and R (highest) (see Table 2.S1). Dashed contours indicate S-ROIs rejected with deviant mean phase angles (see Fig. 2.7). (**C**) Retained S-ROIs (enclosed in black contours) and rejected S-ROIs (indexed without contours) after S-ROI selection.

2.2.7 Limitations of the linear statistics method

The linear statistical method uses a single measure to determine if the signal-to-noise ratio of a periodic signal is statistically significant in each voxel. It is straightforward to identify voxels with the highest statistical measures (i.e., peak activation) within each S-ROI. To construct a somatotopic map, however, a generally accepted statistical threshold is selected to outline the larger extent of each body-part representation. As shown on the cortical surfaces of one representative subject (Fig. 2.2A), dozens of S-ROIs survive at $p = 0.001$ (uncorrected), including those located within and outside the primary sensorimotor cortex. Although recent fMRI studies have revealed somatotopic areas in nonprimary cortex (e.g., Huang et al., 2012; Zlatkina et al., 2016), the boundary of a broader sensorimotor network has not been established for accepting or rejecting S-ROIs solely by their anatomical locations. Some of the S-ROIs found in the posterior parietal, frontal, temporal, cingulate, and even occipital cortex could contain authentic brain activation driven by higher-level processing of tactile stimuli, while others could result from non-brain activities containing partial but strong periodic signals at the stimulus frequency from unknown sources. For example, S-ROIs LH-23 and RH-40 in the primary visual cortex (V1) of Subject 1 (Fig. 2.2A) show significant response and could potentially be involved in cross-modal processing of tactile stimuli. Although it is

straightforward to reject S-ROIs located in the visual cortex in fMRI experiments that only involve tactile stimulation, objective and quantitative measures still need to be developed to further differentiate S-ROIs within and outside the primary somatosensory cortex (S-I). A fundamental assumption for an ideal periodic signal is that its amplitude and phase angle are stable throughout the entire time series. However, a single statistical measure (e.g., *F*-statistic) only reveals the overall correlation between an fMRI time series and the stimulus pattern (e.g., a periodic boxcar), which does not take into consideration the temporal stability of amplitude and phase of a periodic signal over the duration of the scan. For example, S-ROIs in V1 and S-I of Subject 1 show comparable signal energy at the stimulus frequency in the average power spectra; however, the fMRI time series in bilateral V1 show partial periodic waveforms with higher amplitude than those in S-I (Fig. 2.3). The effect of partial periodicity on signal stability is further illustrated with simulated data in the *Simulation* section below. To overcome the aforementioned limitations, we apply time-frequency analysis to fMRI time series, use circular statistics to characterize the distribution of signal phase and reject outlier voxels within each S-ROI, and then assess the temporal variability of a periodic signal in each S-ROI by measuring the total path length of its SNR trajectory in the complex plane.

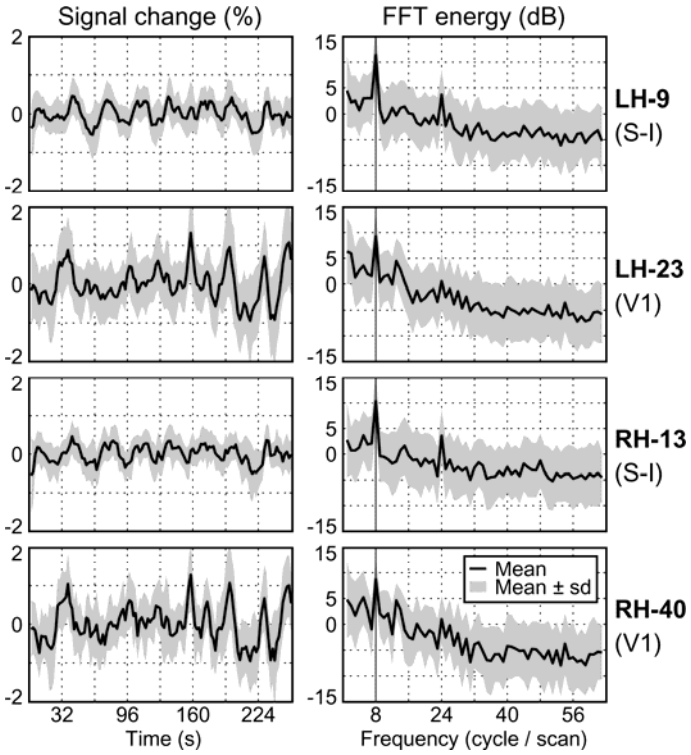

Fig. 2.3: Examples of periodic and quasi-periodic fMRI signals in four selected S-ROIs of Subject 1. S-ROIs LH-9 and RH-13 in S-I showed sustained periodic signals (full 8 cycles) with low amplitude, while S-ROIs LH-23 and RH-40 in V1 showed only a few cycles with high amplitude (left panels). FFT power spectra of time series in all four S-ROIs (right panels) showed comparable signal energy at the stimulus frequency (8 cycles/scan).

2.2.8 Time-frequency analysis

Time-frequency decomposition is applied to the time series of all surface-bound voxels in both hemispheres. For Voxel m in an S-ROI r containing M voxels, the detrended time series (128 points) is multiplied by a moving Hamming window (width: 16 points) centered at t_0 and then subjected to 128-point DFT to yield $X_m(\omega_s, t_0) = |X_m(\omega_s, t_0)| \exp[j\theta_m(\omega_s, t_0)]$ using Eq. (2.1). In the resulting Fourier spectrum,

the SNR within this window is computed by dividing the signal energy at the stimulus frequency ω_s (8 cycles/scan) by the sum of energy at the remaining frequencies ω_n (0-63 cycles/scan excluding ω_s):

$$\left|S_m(\omega_s,t_0)\right|^2=\frac{\left|X_m(\omega_s,t_0)\right|^2}{\sum_{n,n\neq s}\left|X_m(\omega_n,t_0)\right|^2}. \tag{2.3}$$

The SNR amplitude and phase at time t_0 are represented by:

$$S_m(\omega_s,t_0)=\left|S_m(\omega_s,t_0)\right|\exp\left[j\theta_m(\omega_s,t_0)\right]. \tag{2.4}$$

Repeating this procedure for each $t=t_0$ with a step size of 1, a complex SNR time series at the stimulus frequency ω_s of Voxel m is then obtained:

$$S_m(\omega_s,t)=\left|S_m(\omega_s,t)\right|\exp\left[j\theta_m(\omega_s,t)\right]. \tag{2.5}$$

This time series is further averaged across time to obtain the mean SNR of this voxel:

$$\bar{S}_m(\omega_s)=\frac{1}{T}\sum_{t=1}^{T}S_m(\omega_s,t)=\left|\bar{S}_m(\omega_s)\right|\exp\left[j\bar{\theta}_m(\omega_s)\right], \tag{2.6}$$

in which $\left|\bar{S}_m(\omega_s)\right|$ and $\bar{\theta}_m(\omega_s)$ are the mean SNR amplitude and mean phase angle of Voxel m. Finally, $\bar{S}_m(\omega_s)$ is averaged across M voxels to obtain the mean SNR amplitude and mean phase angle of S-ROI r by:

$$\bar{S}^{(r)}(\omega_s)=\frac{1}{M}\sum_{m=1}^{M}\bar{S}_m(\omega_s)=\left|\bar{S}^{(r)}(\omega_s)\right|\exp\left[j\bar{\theta}^{(r)}(\omega_s)\right]. \tag{2.7}$$

2.2.9 Circular statistics

Circular statistics (also known as directional statistics) is used to model the distribution of an angular dataset $\phi \in \{\phi_n\}_{n=1}^{N} = \{\phi_1, \ldots, \phi_N\}$. Each angle is first converted into a unit-length complex number $z_n = \exp(j\phi_n)$, and the average of all complex numbers is obtained by:

$$\mu_1 = \bar{z} = \frac{1}{N}\sum_{n=1}^{N} z_n = \bar{R}_1 \exp(j\bar{\phi}_1), \tag{2.8}$$

in which $\bar{R}_1$ is the resultant length and $\bar{\phi}_1$ is the mean direction (Fisher, 1993).

Eq. (2.8) is modified for a complex dataset $z \in \{z_n\}_{n=1}^{N} = \{z_1, \ldots, z_N\}$, which contains non-unit-length complex numbers $z_n = r_n \exp(j\phi_n)$. The first moment, μ_1, is computed by (Grabska-Barwińska et al., 2012; Levick and Thibos, 1982; Ringach et al., 2002):

$$\mu_1 = \frac{\sum_{n=1}^{N} z_n}{\sum_{n=1}^{N} |z_n|} = \bar{R}_1 \exp(j\bar{\phi}_1), \tag{2.9}$$

in which $\bar{R}_1$ is the resultant length, and $\bar{\phi}_1$ is the mean direction. Similarly, the p^{th} moment, μ_p, is computed by:

$$\mu_p = \frac{\sum_{n=1}^{N} z_n^p}{\sum_{n=1}^{N} |z_n|^p} = \bar{R}_p \exp(j\bar{\phi}_p), \tag{2.10}$$

in which $\bar{R}_p$ is the resultant length, and $\bar{\phi}_p$ is the mean direction. Note that for all *p*, $0 \le \bar{R}_p \le 1$.

The circular variance, $cvar$, is defined as (Fisher, 1993, Grabska-Barwińska et al., 2012; Levick and Thibos, 1982; Ringach et al., 2002):

$$cvar = 1 - \overline{R}_1 , \tag{2.11}$$

and the circular standard deviation, csd, is defined as:

$$csd = \sqrt{-2\log(1 - cvar)} = \sqrt{-2\log \overline{R}_1} , \tag{2.12}$$

where $\log(\cdot)$ denotes natural logarithm. Note that csd is not equal to $\sqrt{cvar}$. The circular dispersion, δ, is defined as:

$$\delta = \frac{1 - \overline{R}_2}{2\overline{R}_1^2} , \tag{2.13}$$

in which $\overline{R}_1$ and $\overline{R}_2$ are the resultant length from the first two moments. The value of $cvar$ ranges between 0 and 1, and the values of csd and δ range from 0 to positive infinity. In an angular dataset, smaller values of $cvar$, csd, and δ indicate a more concentrated distribution of angles (Fig. 2.4).

In this study, within-voxel circular statistics, $cvar_m$, csd_m, and δ_m, were computed from the complex time series $S_m(\omega_s, t)$ [see Eq. (2.5)] of Voxel m; within-ROI circular statistics, $cvar^{(r)}$, $csd^{(r)}$, and $\delta^{(r)}$ were computed from the distribution of $\overline{S}_m(\omega_s)$ [see Eq. (2.6)] across voxels within S-ROI r.

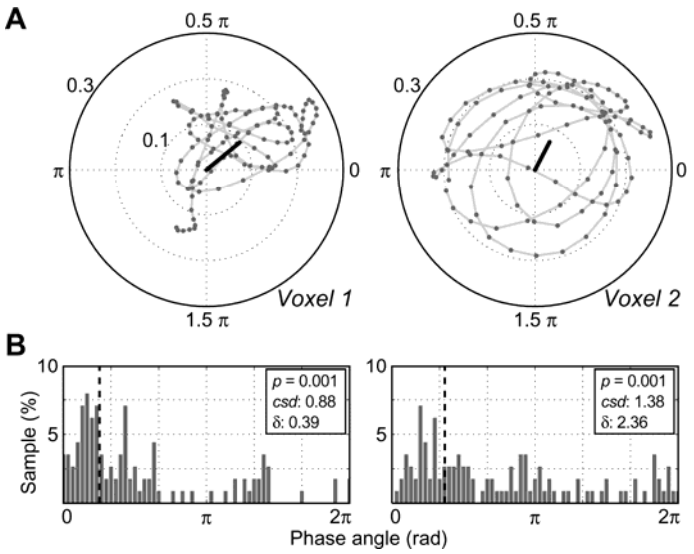

Fig. 2.4: Complex time series (**A**) and distribution of phase angles (**B**) in two representative voxels of Subject 1. The black bar in (A) and dashed line in (B) represent the mean phase angle, $\overline{\theta}_m(\omega_s)$, in each voxel. Although both voxels have the same *p*-value, Voxel 1 shows a narrower distribution of phase angles as characterized by lower values of circular standard deviation and dispersion (csd_m and δ_m).

2.2.10 Voxel selection

Each S-ROI is outlined as a cortical region representing a single body part (e.g., face or hand), and thus most of its voxels are assumed to exhibit a homogeneous distribution of phase angles. However, some voxels, even in the primary somatosensory cortex, may contain non-brain tissues and/or cerebrospinal fluid (Buxton, 2009), which affect local magnetic susceptibility and result in signal characteristics notably different from the majority of voxels in an S-ROI. To better assess the overall signal stability in an S-ROI, two criteria based on circular statistics are defined to reject outliers from further

analysis (Fig. 2.5). First, a voxel is rejected if its mean phase angle $\overline{\theta}_m(\omega_s)$ [see Eq. (2.6)] falls outside of the angular boundaries (a black thick sector in Fig. 2.5B) defined by:

$$\overline{\theta}^{(r)}(\omega_s) \pm csd^{(r)}, \tag{2.14}$$

where $\overline{\theta}^{(r)}(\omega_s)$ [see Eq. (2.7)] and $csd^{(r)}$ are the mean and circular standard deviation of phase angles, $\left\{\overline{\theta}_m(\omega_s)\right\}_{m=1}^{M}$ [see Eq. (2.6)], computed across M untrimmed voxels within S-ROI r (Fig. 2.5A). The second criterion further selects voxels based on circular statistical measures, csd_m and δ_m, computed within each voxel (Fig. 2.5C). In a two-condition block-design experiment, the range of phase angles of a complex time series [See Eq. (2.5)] in response to each stimulus condition (face or hand) is anticipated to be less than half of a cycle (180° or ±90°). Therefore, voxel m is rejected if its csd_m is larger than 90° or δ_m is larger than 1.5 (an empirically determined threshold). For the remaining M_{trim} voxels (Fig. 2.5D), $\overline{S}^{(r)}(\omega_s)$ and $\overline{\theta}^{(r)}(\omega_s)$ in Eq. (2.7) are recalculated to obtain:

$$\overline{S}_{\text{trim}}^{(r)}(\omega_s) = \frac{1}{M_{\text{trim}}} \sum_{m=1}^{M_{\text{trim}}} \overline{S}_m(\omega_s) = \left|\overline{S}_{\text{trim}}^{(r)}(\omega_s)\right| \exp\left[j\overline{\theta}_{\text{trim}}^{(r)}(\omega_s)\right]. \tag{2.15}$$

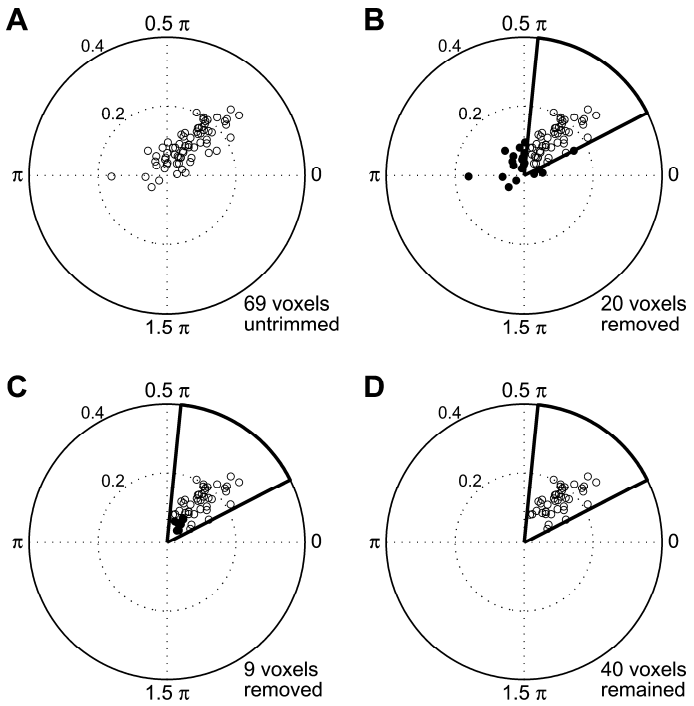

Fig. 2.5: Voxel selection for a representative S-ROI of Subject 1. (**A**) Distribution of untrimmed voxels in the complex plane. Each circle represents the mean amplitude and phase angle in each voxel. (**B**) Removing voxels (black dots) with mean phase angles, $\overline{\theta}_m(\omega_s)$, falling outside of the circular boundaries (thick black sector) defined by Eq. (2.14). (**C**) Removing voxels (black dots) with $csd_m \geq 90°$ or $\delta_m \geq 1.5$. (**D**) Remaining voxels after voxel selection.

2.2.11 Temporal variability of periodic signals

To assess the overall temporal variability of signals at the stimulus frequency ω_s complex SNR time series $S_m(\omega_s, t)$ are point-wise averaged across M_{trim} remaining voxels in an S-ROI (after voxel selection) to obtain an average complex time series:

$$\overline{S}^{(r)}_{\text{trim}}(\omega_s, t) = \frac{1}{M_{\text{trim}}} \sum_{m=1}^{M_{\text{trim}}} S_m(\omega_s, t) = \left|\overline{S}^{(r)}_{\text{trim}}(\omega_s, t)\right| \exp\left[j\,\overline{\theta}^{(r)}_{\text{trim}}(\omega_s, t)\right]. \qquad (2.16)$$

The temporal variability of a complex time series, $\{z(1), \cdots, z(t), \ldots, z(T)\}$, is as-

sessed by the total path length of its trajectory in the complex plane (Fig. 2.6A):

$$L = \sum_{t=2}^{T} \left| z(t) - z(t-1) \right|, \tag{2.17}$$

in which $|\cdot|$ denotes the distance between two consecutive time points on the trajectory. A smaller L value indicates a more stable periodic signal (Fig. 2.6B, C), e.g., L is zero for a pure sine wave. For each S-ROI, the temporal variability of the complex SNR time series $\overline{S}^{(r)}_{\text{trim}}(\omega_s, t)$ is computed by:

$$\overline{L}^{(r)}_{\text{trim}}(\omega_s) = \sum_{t=2}^{T} \left| \overline{S}^{(r)}_{\text{trim}}(\omega_s, t) - \overline{S}^{(r)}_{\text{trim}}(\omega_s, t-1) \right|. \tag{2.18}$$

Finally, S-ROIs on both hemispheres are sorted by temporal variability (L-value) and each of them is assigned a rank between 1 (lowest) and R (highest), where R is the total number of S-ROIs in both hemispheres of each subject (Fig. 2.2B; Table 2.S1).

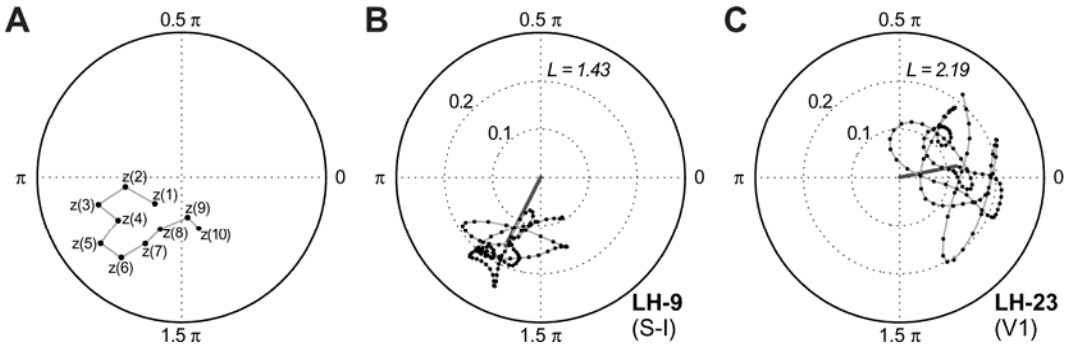

Fig. 2.6: Measuring the temporal variability of a periodic signal by the total path length of its trajectory in the complex plane. (A) Schematics of a 10-point time series. (B, C) The path length of the mean SNR time series in two representative S-ROIs of Subject 1. The gray thick bar indicates the mean phase angle in each S-ROI. The temporal variability (L-value) of S-ROI LH-9 is lower than that of LH-23.

2.2.12 S-ROI clustering and selection

Within each subject, S-ROIs are grouped into clusters (face or hand) by S-ROI mean phase angle, $\overline{\theta}^{(r)}_{\text{trim}}(\omega_s)$ [see Eq. (2.15)]. The angular boundaries of each body-part cluster (dashed sectors in Fig. 2.7) are calculated from the mean $\pm$ 1.5 csd of all $\overline{\theta}^{(r)}_{\text{trim}}(\omega_s)$ within each cluster using Eqs. (2.7) and (2 12). In each cluster, an S-ROI is rejected if its mean phase angle deviates from the cluster; i.e., with $\overline{\theta}^{(r)}_{\text{trim}}(\omega_s)$ falling outside of the boundaries (e.g., see S-ROIs outlined in dashed contours in Fig. 2.2B). Finally, S-ROIs surviving all selection criteria are retained and rendered on the cortical surfaces (Fig. 2.2C).

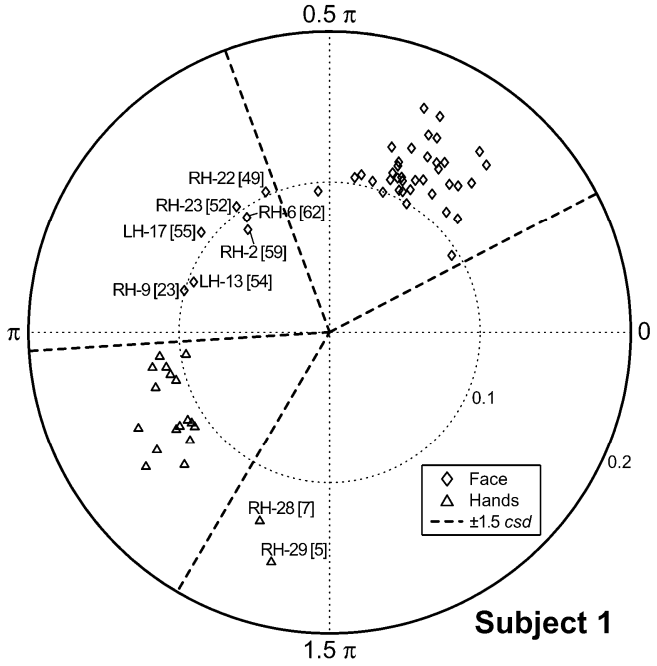

Fig. 2.7: Distribution of S-ROI mean phase angles, $\overline{\theta}^{(r)}_{\text{trim}}(\omega_s)$, in Subject 1. Each dashed sector indicates the average $\pm$ 1.5 csd of $\overline{\theta}^{(r)}_{\text{trim}}(\omega_s)$ in the face or hand cluster. Only S-ROIs with $\overline{\theta}^{(r)}_{\text{trim}}(\omega_s)$ falling outside of the sectors are labeled, with their ranks of temporal variability indicated in brackets (see Table 2.S1).

2.2.13 Summary of data analysis

Figure 2.8 summarizes the data processing pipeline of analytic methods proposed in this study. Table 2.1 summarizes the notations used for within voxel and within S-ROI analyses.

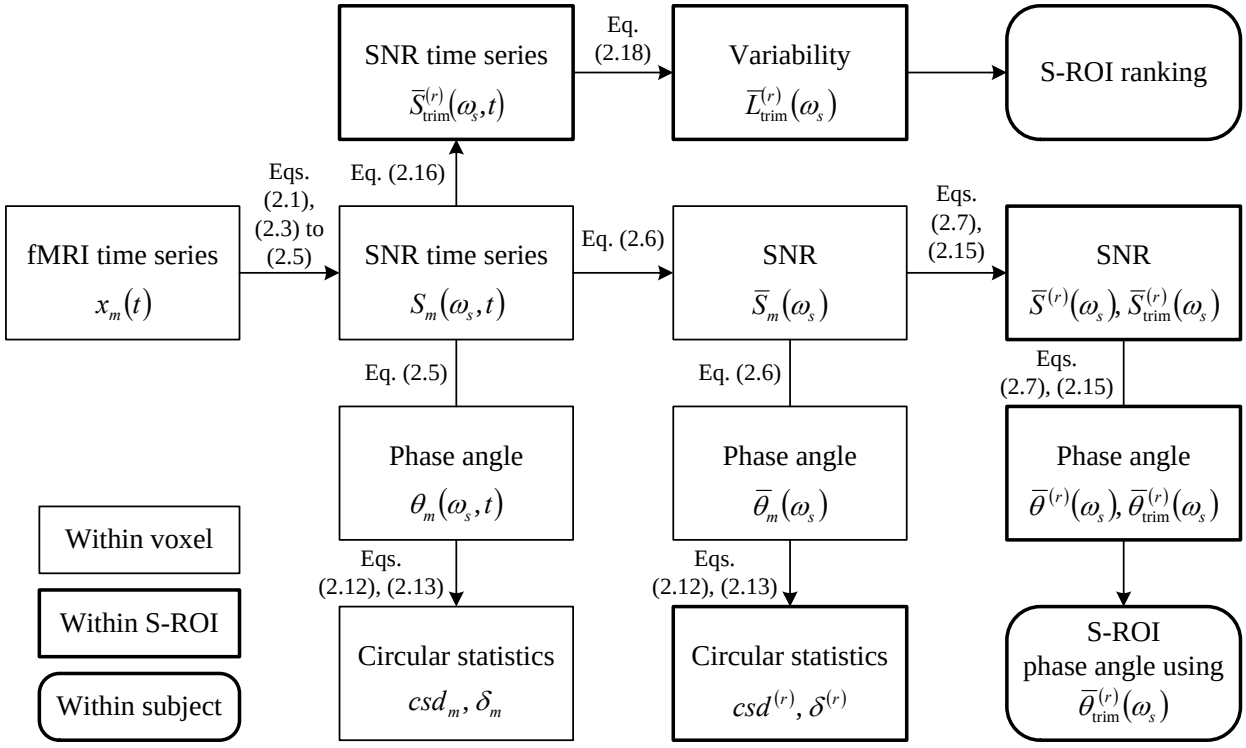

Fig. 2.8: Data analysis pipeline. Legends on the lower left corner indicate the levels of analysis.

Table 2.1: Summary of notations.

Category	Notation	Equation	Level	Description
SNR	$S_m(\omega_s,t)$	Eq. (2.5)	Voxel	SNR time series of a voxel.
	$\overline{S}_m(\omega_s)$	Eq. (2.6)	Voxel	Mean SNR of a voxel.
	$\overline{S}^{(r)}(\omega_s)$	Eq. (2.7)	S-ROI	Mean SNR of an S-ROI. Trim: recomputed from the
	$\overline{S}^{(r)}_{\text{trim}}(\omega_s)$	Eq. (2.15)		remaining voxels after voxel selection.
	$\overline{S}^{(r)}_{\text{trim}}(\omega_s,t)$	Eq. (2.16)	S-ROI	Mean SNR time series of an S-ROI.
Phase angle	$\theta_m(\omega_s,t)$	Eq. (2.5)	Voxel	Phase angle time series of a voxel.
	$\overline{\theta}_m(\omega_s)$	Eq. (2.6)	Voxel	Mean phase angle of a voxel.
	$\overline{\theta}^{(r)}(\omega_s)$	Eq. (2.7)	S-ROI	Mean phase angle of an S-ROI. Trim: recomputed
	$\overline{\theta}^{(r)}_{\text{trim}}(\omega_s)$	Eq. (2.15)		from the remaining voxels after voxel selection.
Circular statistics	csd_m; δ_m	Eqs. (2.12), (2.13)	Voxel	Circular standard deviation / dispersion of a voxel.
	$csd^{(r)}$; $\delta^{(r)}$	Eqs. (2.12), (2.13)	S-ROI	Circular standard deviation / dispersion of an S-ROI.
Temporal Variability	$\overline{L}^{(r)}_{\text{trim}}(\omega_s)$	Eq. (2.18)	S-ROI	Path length of the mean SNR time series of an S-ROI.

2.2.14 Simulation

Simulated data were used to illustrate the effect of noise on circular statistical measures and signal stability. Periodic signals $\eta^{(1)}(t)$ (a 128-point sine wave at frequency $\omega_s = 8$ cycles/scan), and white Gaussian noise $\varepsilon(t)$, were generated using MATLAB *sin* and *wgn* functions respectively. Three levels of SNR were simulated to match statistical measures of $p = 10^{-8}$, $p = 10^{-4}$, and $p = 0.05$, which were estimated from $F_{2,102}$ [see Eq. (2.2)]. In the first set of simulation (Fig. 2.9A, left panels), three

time series $\gamma_1^{(1)}(t)$, $\gamma_2^{(1)}(t)$, and $\gamma_3^{(1)}(t)$ with an overall SNR = 0.44, 0.2, and 0.06 were generated by adjusting α_i in:

$$\gamma_i^{(1)}(t) = \frac{\alpha_i \eta^{(1)}(t) + \varepsilon(t)}{\alpha_i + 1},\ i = 1, 2, 3. \tag{2.19}$$

Time-frequency analysis [Eqs. (2.3) to (2.5)] was then applied to these time series to yield the SNR time series at the stimulus frequency ω_s: $\Gamma_1^{(1)}(\omega_s, t)$, $\Gamma_2^{(1)}(\omega_s, t)$, and $\Gamma_3^{(1)}(\omega_s, t)$. Circular standard deviation ($csd^{(1)}$), circular dispersion ($\delta^{(1)}$), and path length ($\overline{L}^{(1)}$) were computed from these SNR time series (Fig. 2.9B, C, left panels). All three measures increase as the level of overall SNR decreases (Table 2.2, Simulation 1).

Table 2.2: Circular statistics and temporal variability of simulated data.

	Overall	Simulation 1 (Full 8 cycles)			Simulation 2 (2 in 8 cycles off)		
p-value	SNR	$csd^{(1)}$	$\delta^{(1)}$	$\overline{L}^{(1)}$	$csd^{(2)}$	$\delta^{(2)}$	$\overline{L}^{(2)}$
10^{-8}	0.44	0.372	0.138	1.852	0.665	0.249	2.320
10^{-4}	0.2	0.617	0.318	2.058	0.832	0.535	2.333
0.05	0.06	1.121	1.276	2.171	1.271	2.117	2.336

csd: circular standard deviation; δ: circular dispersion; $\overline{L}$: path length. The superscripts (1) and (2) indicate simulation sets.

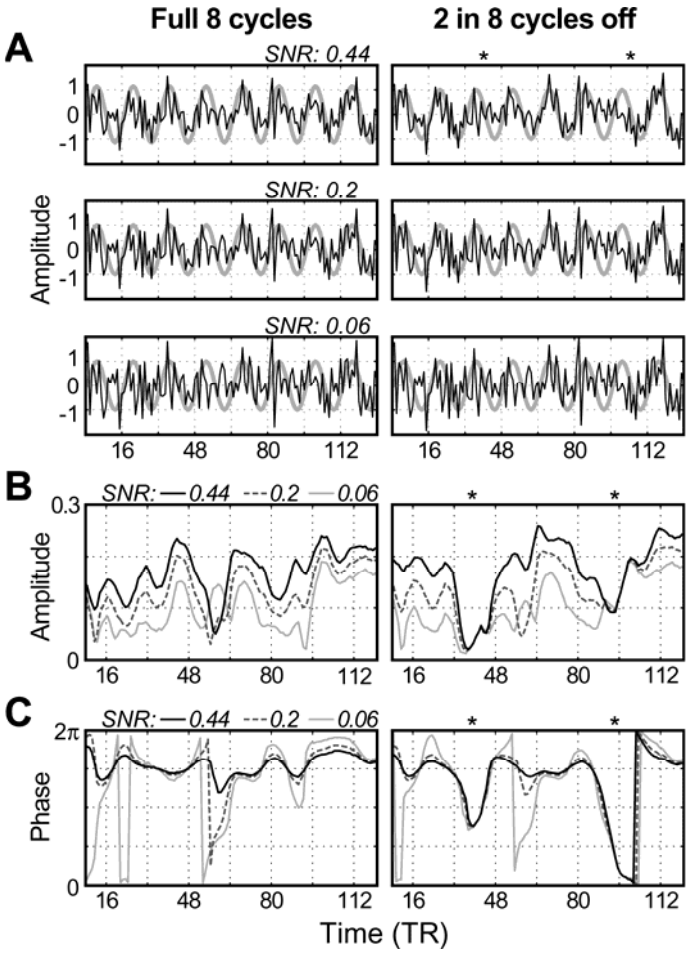

Fig. 2.9: Analysis of simulated data consisting of full and partial periodic signals with additive noise. Left panels: full eight cycles of periodic signals; Right panels: two in eight cycles off, as indicated by (*). (**A**) Time courses of simulated data (black traces). Thick gray traces: pure sine waves. (**B**, **C**) Amplitude and phase angle of the complex SNR time series obtained by Eqs. (2.3) to (2.5).

To further illustrate the effect of partial periodicity on circular statistical measures and signal stability, two cycles of the pure sine wave, $\eta^{(1)}(t)$, were set to 0 (off) yielding $\eta^{(2)}(t)$. The same noise from the previous simulation, $\varepsilon(t)$, was superimposed on $\eta^{(2)}(t)$ as in:

$$\gamma_i^{(2)}(t) = \frac{\beta_i \eta^{(2)}(t) + \varepsilon(t)}{\alpha_i + 1},\ i = 1, 2, 3, \tag{2.20}$$

where α_i in the denominator is from the previous simulation. The overall SNR of $\gamma_1^{(2)}(t)$, $\gamma_2^{(2)}(t)$, and $\gamma_3^{(2)}(t)$ were set to 0.44, 0.2, and 0.06 respectively by adjusting β_i (Fig. 2.9A, right panels). Time-frequency analysis was then applied to $\gamma_i^{(2)}(t)$ [Eqs. (2.3) to (2.5)], and $csd^{(2)}$, $\delta^{(2)}$ and $\overline{L}^{(2)}$ were computed from the resulting SNR time series (Fig. 2.9B, C, right panels). All three measures increase as the overall SNR level decreases (Table 2.2, Simulation 2). At the same level of overall SNR, these measures are higher in partial periodic signals (Table 2.2; comparing Simulation 1 with Simulation 2).

2.3 Results

Results of S-ROI selection are illustrated in details for Subjects 1 to 4 (Figs. 2.2, 2.7; Inline Supplementary Figs. 2.S1-2.S4; Supplementary Tables 2.S1 to 2.S4). Additional results of S-ROI selection in Subjects 5 to 16 are included in Supplementary Figs. 2.S5-2.S16 and Supplementary Tables 2.S5-2.S16. For each subject, we summarize S-ROIs approximately grouped by cortical regions and reject S-ROIs with moderate to high temporal variability and/or deviant phase angles. In some cases, S-ROIs with low to moderate temporal variability are further rejected if they appear in random cortical regions with low probabilities of tactile response according to the surface-based probabilistic group-average map as detailed in *Inter-subject spatial variability* below (Fig. 2.10).

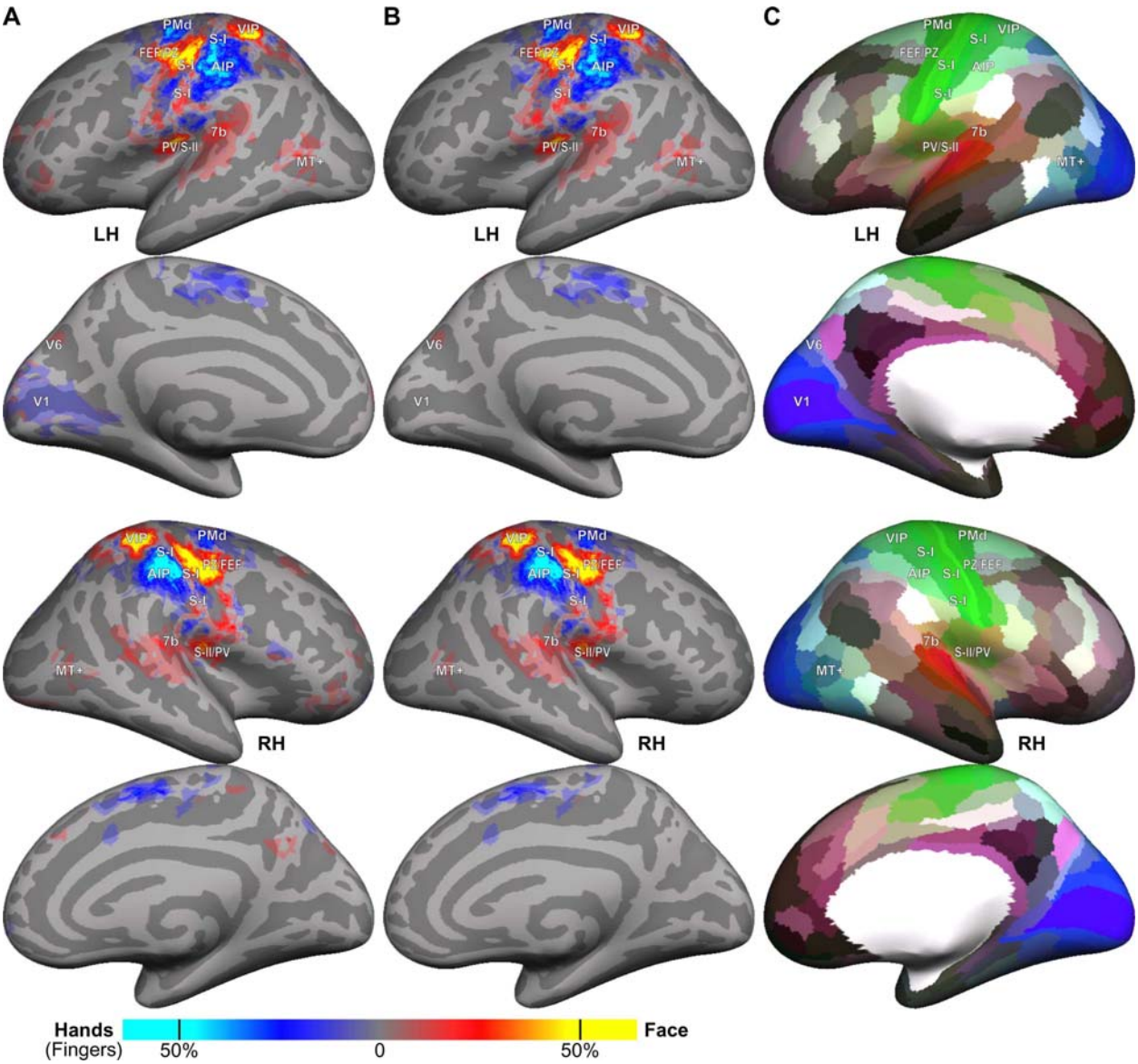

Fig. 2.10: A group-average probabilistic map showing common activation sites across sixteen subjects. (**A**) An initial group-average map of S-ROIs retained with low to moderate temporal variability. (**B**) The final group-average map reconstructed after spatial screening of S-ROIs (see text). (**C**) HCP-MMP1.0 atlas (Glasser et al., 2016) rendered on the same cortical surfaces and overlaid with labels at exactly the same locations in (A) and (B). Labels relating to approximate areas in the HCP atlas are summarized as follows: PMd: area 6d; FEF/PZ: FEF and area 4; S-I (face): area 3b; S-I (hand/fingers): areas 1 and 2; AIP: areas 2, PFt, and AIP; VIP: areas 2 and 7PC; PV/S-II: areas Op2-3, Op4, and Ig; 7b: area RI; MT+: areas MST and MT.

2.3.1 Subject 1

Pre- and postcentral regions. S-ROIs LH-2, LH-9, LH-10, LH-19, LH-20, LH-21, RH-10, RH-12, RH-13, RH-32, RH-33, and RH-34 located between pre- and postcentral gyri are to be retained because they show low to moderate temporal variability (Fig. 2.2B, C; unmarked entries in Table 2.S1). However, S-ROIs LH-7, LH-8, LH-11, and RH-31 in the same region are to be rejected due to moderate to high temporal variability (Fig. 2.2B, C; indicated by shaded entries in Table 2.S1).

Posterior parietal regions. S-ROIs LH-12, LH-18, RH-14, RH-15, RH-16, and RH-35 in the posterior parietal cortex are to be retained because they show low to moderate temporal variability. S-ROIs LH-13 and LH-14 in the same region are to be rejected due to moderate to high temporal variability.

Insular and temporal regions. S-ROIs LH-3, LH-4, and RH-11 near/in the posterior lateral sulcus (parietal operculum) are retained despite of moderate temporal variability. In temporal-parietal regions, S-ROIs LH-5 and RH-17 are to be rejected due to moderate to high temporal variability. In middle temporal regions, LH-6 and RH-18 are retained despite of moderate temporal variability.

Lateral frontal regions. S-ROIs RH-2 to RH-9 in the frontal cortex are to be rejected because they show moderate to high temporal variability. On the contrary, S-

ROIs LH-1, RH-1, RH-28, RH-29, and RH-30 in the inferior frontal region show low temporal variability, indicating relatively stable periodic signals. S-ROIs RH-28 and RH-29 are to be rejected immediately because they show deviant mean phase angles (Fig. 2.7). S-ROIs LH-1, RH-1, and RH-30 are initially retained but later rejected during spatial screening according to the group-average map (Fig. 2.10A, B).

Other regions. S-ROIs LH-22, RH-36, and RH-37 near or in the cingulate sulcus are retained despite of moderate temporal variability. S-ROIs LH-15 and RH-21 to RH-25 in the medial frontal region are to be rejected due to high temporal variability. S-ROIs LH-16, RH-26, and RH-27 in the precuneus are to be rejected due to high temporal variability. S-ROIs LH-17, LH-23, RH-19, RH-20, and RH-38 to RH-40 in the occipital lobe are to be rejected due to moderate to high temporal variability.

2.3.2 Subject 2

Pre- and postcentral regions. S-ROIs LH-3, LH-8, LH-12, LH-13, LH-14, RH-3, RH-8, RH-18, and RH-19 located between pre- and post-central gyri are to be retained because they show low to moderate temporal variability (Fig. 2.S2B, C; Table 2.S2). However, S-ROIs LH-2, LH-4, LH-5, LH-23, RH-1, RH-2, and RH-24 in the same region are to be rejected due to high temporal variability.

Posterior parietal regions. S-ROIs LH-7, LH-15, RH-5, RH-6, RH-7, RH-21, and RH-22 in the posterior parietal cortex are to be retained because they show low to moderate temporal variability. S-ROIs LH-5, LH-6, LH-16, LH-17, LH-24, RH-4, and RH-23 in the same region are to be rejected due to moderate to high temporal variability.

Insular and temporal regions. S-ROIs LH-11 and RH-14 in the middle temporal region are to be retained because they show low temporal variability, while RH-13 in the same region is to be rejected due to high temporal variability. S-ROIs LH-8, LH-9, LH-10, LH-18, LH-19, RH-8, RH-9, RH-12, RH-17, and RH-20 near/in the lateral sulcus (parietal operculum) are to be retained because they show low to moderate temporal variability. S-ROIs LH-8 and LH-9 are not rejected for deviant mean phase angles because they fall slightly outside the boundaries (Fig. 2.S1A). S-ROIs RH-10, RH-11, and RH-16 in the same region are to be rejected due to high temporal variability.

Other regions. S-ROI LH-22 in the cingulate sulcus is retained despite that it shows only moderate temporal variability, while S-ROIs LH-20, LH-21, and RH-25 are to be rejected due to moderate to high temporal variability. S-ROIs LH-1 in the frontal cortex and RH-15 in the occipital cortex are to be rejected due to high temporal variability.

2.3.3 Subject 3

Pre- and post-central regions. S-ROIs LH-1, LH-3, LH-4, LH-5, RH-1, RH-2, RH-9, RH-10, and RH-17 located between pre- and post-central gyri are to be retained because they show low to moderate temporal variability (Fig. 2.S3B, C; Table 2.S3). However, S-ROIs LH-9, LH-10, and LH-17 in the same region are to be rejected due to high temporal variability.

Posterior parietal regions. S-ROIs LH-6, LH-11, RH-3, RH-10, RH-11, and RH-12 in the posterior parietal cortex are to be retained because they show low to moderate temporal variability. S-ROIs LH-7, LH-13, LH-15, LH-16, and RH-4 in the same region are to be rejected due to high temporal variability, while LH-14 is to be rejected for its deviant mean phase angle (Fig. 2.S1B).

Insular and temporal regions. S-ROI LH-8 in the middle temporal region is to be rejected due to high temporal variability. S-ROIs LH-2, LH-12, RH-6, RH-13, and RH-14 near/in the lateral sulcus (parietal operculum) are to be retained because they show low to moderate temporal variability. S-ROI RH-5 in the same region is to be rejected due to high temporal variability.

Other regions. S-ROIs RH-7 in the lateral occipital cortex and RH-8 in the frontal cortex are to be rejected due to high temporal variability and deviant mean phase an-

gles (Fig. 2.S1B). S-ROIs LH-18, RH-15, and RH-16 near/in the cingulate sulcus are to be retained despite of moderate to slightly higher temporal variability (see Discussion). S-ROI LH-19 in the same region is to be rejected due to moderate temporal variability and its deviant mean phase angle (Fig. 2.S1B).

2.3.4 Subject 4

Pre- and post-central regions. S-ROIs LH-2, LH-6, LH-13, LH-15, LH-16, RH-1, RH-8, and RH-10 located between pre- and post-central gyri are retained because they show low to moderate temporal variability (Fig. 2.S4B, C; Table 2.S4). However, S-ROI LH-3 in the same region is to be rejected due to high temporal variability. Furthermore, S-ROIs LH-1 and LH-14 are to be rejected because they show deviant mean phase angles (Fig. 2.S1C).

Posterior parietal regions. S-ROIs LH-10, LH-11, LH-15, RH-3, and RH-8 in the posterior parietal cortex are to be retained because they show low to moderate temporal variability. S-ROIs RH-4 and RH-9 in the same region are to be rejected due to high temporal variability.

Insular and temporal regions. S-ROI LH-9 in the middle temporal region is to be rejected due to high temporal variability. S-ROIs LH-4, LH-5, LH-8, and RH-6 near/in the

lateral sulcus (parietal operculum) are to be retained because they show low to moderate temporal variability. S-ROIs LH-7 and RH-5 in the same region are to be rejected due to high temporal variability, while RH-2 is to be rejected for its deviant mean phase angle (Fig. 2.S1C).

Other regions. S-ROIs LH-17 and RH-11 near the cingulate sulcus are to be retained as they show high temporal variability. S-ROIs LH-12 and RH-7 in the same region are to be rejected due to high temporal variability.

2.3.5 Inter-subject spatial variability

To find common activation sites across subjects, we constructed a surface-based probabilistic map for spatial screening of S-ROIs using spherical group averaging methods (Fischl et al., 1999; Hagler et al., 2007). For each hemisphere of each subject, vertices enclosed in each initially retained S-ROI with low to moderate temporal variability are assigned a value of 100 and the remaining vertices on the cortical surface are assigned a value of 0. Each binary map is morphed into the spherical coordinates to register with the *Buckner40* average sphere in FreeSurfer. The morphed binary maps are averaged across subjects ($N = 16$) in the spherical coordinates, and then rendered on inflated cortical surfaces of the *fsaverage* dataset in FreeSurfer. An initial group-average

map (Fig. 2.10A) is used as a reference map to further screen random S-ROIs with a low probability of occurrence across subjects. For example, the lateral frontal cortex contains random S-ROIs in a few subjects, each of which appears only once at an inconsistent location. These S-ROIs are rejected within each subject during spatial screening to reconstruct a final group-average map (Fig. 2.10B; also see S-ROIs indicated by double daggers [‡] in Tables 2.S1 to 2.S16).

Areas with high probabilities of occurrence across subjects include face and hand (finger) representations in the primary somatosensory cortex (S-I); hand (finger) representations in the dorsal premotor cortex (PMd); a polysensory zone (PZ; Graziano and Gandhi, 2000) of face representation in the precentral gyrus, which overlaps with the posterior part of the frontal eye fields (FEF); human homologue of macaque anterior intraparietal area (AIP) at the inferior postcentral sulcus; and human homologue of macaque ventral intraparietal area (VIP) at the superior postcentral sulcus. Other areas with lower probabilities of occurrence across subjects include parietal ventral (PV)/S-II, 7b, and MT+, which are activated by stimulation to the face.

To compare our results with other sensorimotor maps, the HCP-MMP1.0 atlas (Glasser et al., 2016) is projected onto the *fsaverage* cortical surfaces (Fig. 2.10C) using annotation files available from https://figshare.com/articles/HCP-

MMP1_0_projected_on_fsaverage/3498446. The HCP atlas is overlaid with area labels at exactly the same locations as those in the group-average map (Fig. 2.10A, B). While the HCP atlas shows the relative locations among areas, the extent (border) of each area on the atlas is only for reference. Here we tried our best to relate brain areas labeled in our group average map with areas outlined in the HCP atlas (see captions of Fig. 2.10C).

2.4 Discussion

The human sensorimotor network, broadly defined, includes the premotor, primary motor, primary somatosensory, secondary somatosensory, supplementary motor, and posterior parietal cortices. To date, somatotopic representations in the sensorimotor network have only been partially mapped using fMRI and other neuroimaging techniques. One of the challenges of somatotopic mapping is to stimulate multiple body parts under various constraints in the MRI scanner. In this study, we demonstrated the use of wearable technology for automatic tactile stimulation in a block-design fMRI experiment, where air puffs were delivered periodically to the face and hands (fingers) in the same scan. As this technology is still in its early stage of development, further studies are needed to investigate the optimal location, density, intensity, frequency, duration, and spatiotemporal patterns of tactile stimuli for effective stimulation on different body parts in fMRI experiments. For example, previous electrophysiological studies have suggested that the hand and foot exhibit different temporal tuning functions in response to vibrotactile stimulation (Tobimatsu et al. 1999, 2000). Here, we discuss primarily on the validation of measured periodic fMRI signals within S-ROIs in response to periodic boxcar stimulation on two alternating body parts.

Linear systems analysis of fMRI data revealed dozens of S-ROIs within and out-

side the primary sensorimotor cortex in each of the subjects shown. An S-ROI is typically identified as a distinct, continuous cortical region containing voxels with statistical measures higher than a selected threshold. However, this approach has some nontrivial limitations because a single, overall statistical measure (e.g., *F*-statistic) only partially illustrates the signal characteristics of a time series. A high statistical measure may result from a strong quasi-periodic signal that only appears in a portion of a time series. By contrast, a low statistical measure may result from a weak but sustained periodic signal embedded in a noisy time series (Fig. 2.9A). To construct a somatotopic atlas, rather than a handful of peak locations identified with the highest statistical measures, we selected a generally accepted statistical threshold to outline the larger extent (contour) of each S-ROI. We then developed quantitative methods to further validate and differentiate all S-ROIs within each subject. Time-frequency analysis of fMRI signals in each voxel yielded a complex time series of normalized amplitude (SNR) and phase angle at the stimulus frequency. Circular statistics was used to characterize the distribution of phase angles within each voxel, across voxels within each S-ROI, and across S-ROIs within each subject (Figs. 2.4, 2.5, 2.7, 2.S1). Voxels with deviant phase angles were rejected from further analysis to ensure a more precise estimate of the mean phase angle in each S-ROI, and S-ROIs with mean phase angles deviating from each

body-part cluster were then rejected in each subject (Figs. 2.7, 2.S1). Temporal variability of the average SNR time series in each S-ROI was assessed by the total path length of its trajectory in the complex plane (Fig. 2.6). Finally, S-ROIs were sorted by their temporal variability within each subject (Figs. 2.2B, 2.S2B, 2.S3B, 2.S4B). These second-level analyses (Fig. 2.8; Table 2.1) reveal the phase distribution and temporal stability of periodic signals not obtainable by conventional linear statistical measures.

Existing advanced mathematical algorithms, such as spatial independent component analysis (ICA), principal component analysis (PCA), and clustering, could potentially be used for second-level voxel selection. Although spatial ICA can parcellize the whole brain volume into different independent sources (Beckmann, 2012; Smith et al., 2013), it can not be applied to most S-ROIs that contain less spatial samples (voxels) than temporal samples (128 time points) in the current study. It is possible to use PCA to reduce data dimension and select voxels with the highest variance in fMRI time series. Furthermore, clustering methods (e.g., *k*-means or fuzzy *c*-means) could be used to classify voxels into a number of clusters. However, neither PCA nor clustering assesses the temporal stability of periodic signals in the resulting principal components or clusters. Both methods would still require a “third-level” analysis on temporal characteristics using the proposed method in the current study.

Wearable tactile stimulation on the face and hands (fingers) activated S-ROIs in frontal, primary sensorimotor, supplementary motor, posterior parietal, insular, temporal, and occipital cortices. To date, a comprehensive atlas of somatotopic maps has not been established in humans. Therefore, S-ROIs cannot be selected by drawing borders defining the overall extent of the sensorimotor network. In our proposed method, the temporal variability of periodic signals facilitates the selection and interpretation of S-ROIs approximately grouped by their cortical locations in each subject. Most of the S-ROIs in the lateral and medial prefrontal cortex can be immediately rejected for high temporal variability and/or deviant phase angles. However, some S-ROIs in the frontal regions show strong periodic signals with low to moderate temporal variability (e.g., S-ROIs LH-1, RH-1, and RH-30 of Subject 1 in Fig. 2.2B; S-ROIs LH-1 and RH-1 of Subject 9 in Fig. 2.S9). While these periodic signals may result from slow head movements at the same frequency as stimulation (8 cycles/scan), the extent of such motion artifacts is unlikely to be restricted to small and isolated cortical regions. Furthermore, these frontal S-ROIs only appear at random locations with very low probabilities of occurrence across subjects according to the group-average map (Fig. 2.10A, B). Therefore, it is justifiable to reject them during spatial screening.

Anterior to the central sulcus, face representations extend into areas PZ at the

precentral gyrus (Graziano and Gandhi, 2000; Huang and Sereno, 2007) and FEF, with high probabilities of occurrence in both hemispheres in the group-average map (Fig. 2.10). Superior to areas PZ/FEF, a hand (finger) representation is found bilaterally in dorsal premotor cortex (PMd) in the group-average map, which is consistent with findings in previous studies (Dresel et al., 2008; Meier et al., 2008).

Some of the S-ROIs located between the pre- and post-central gyri are rejected immediately for high temporal variability (e.g., S-ROIs LH-7, LH-8, and LH-11 of Subject 1 in Fig. 2.2B; S-ROIs LH-4 and LH-5 of Subject 2 in Fig. 2.S2B; S-ROIs LH-3 and RH-6 of Subject 14 in Fig. 2.S14). These S-ROIs are considered false-positive despite that they were initially identified as statistically significant in cortical regions known to respond to tactile stimulation. Other S-ROIs retained in the primary sensorimotor cortex show more complex topological organization across subjects than depicted by the simple homuncular model (Penfield and Boldrey, 1937; also see maps in Meier et al., 2008). Typical organization of face and hand (finger) representations at the postcentral gyrus (S-I) is demonstrated in the left hemispheres of Subject 2 (S-ROIs LH-3 and LH-15 in Fig. 2.S2), Subject 5 (S-ROIs LH-4, LH-5, and LH-7 in Fig. 2.S5), and Subject 10 (S-ROIs LH-8, LH-7, and LH-5 in Fig. 2.S10), where the hands (fingers) are located superior to the face. Other subjects show large variations in the organization of face and

hands (fingers) in S-I. In particular, the lower face (chin) representations show low probabilities of occurrence in both hemispheres in the group-average map (as indicated by “S-I” at the inferior part of the postcentral gyrus in Fig. 2.10). This is likely because the stimulus patterns (rapid random or sequential tactile motion on the face) and intensity did not result in sustained and strong hemodynamic response in this region (Huang et al., 2012; also see discussion of area VIP below). Furthermore, Subject 1 (S-ROIs LH-21 and RH-33 in Fig. 2.2), Subject 2 (S-ROI LH-13 in Fig. 2.S2), Subject 9 (S-ROIs LH-3 and RH-4 in Fig. 2.S9; rejected for deviant phase angles), and Subject 16 (S-ROIs LH-2 and RH-5 in Fig. 2.S16) show significant activation (with the same phase as other “hand/finger” representations) at the inferior part of the central sulcus. These atypical S-ROIs are considered to be deactivation of tongue or lip representations (unstimulated) during stimulation to the face (Fig. 2.1), rather than activation in response to hand/finger stimulation.

The current study used a two-condition block-design paradigm to map locations and overall extent of the hand (finger) and face representations in pre- and post-central regions. Mapping detailed somatotopic representations of individual fingers or subdivisions of the face in primary somatosensory cortex has been demonstrated using phase-encoded design paradigms in previous studies by us and others (Besle et al., 2013;

Huang and Sereno, 2007; Mancini et al., 2012). While the current study did not reveal a detailed somatotopic map within each S-ROI, the proposed method for second-level voxel selection based on circular statistical measures, including mean phase angle and circular standard deviation and dispersion, would be suitable for finding the most probable phase representing a single finger or a face subdivision in future studies.

In the secondary somatosensory cortex, face and/or hand representations are found at the posterior lateral sulcus. For example, S-ROIs LH-3 and LH-4 of Subject 1 (Fig. 2.2) and S-ROIs LH-5 and LH-8 of Subject 4 (Fig. 2.S4) may correspond to areas parietal ventral (PV)/S-II and 7b of face representations (Disbrow et al., 2000; Huang and Sereno, 2007). Both areas PV/S-II and 7b show low probabilities of occurrence in both hemispheres in the group-average map (Fig. 2.10). Beyond the primary and secondary somatosensory cortex, face and hand representations are found in the posterior parietal cortex. For example, the left hemisphere of Subject 1 shows an arrangement of face (VIP) and hand/finger (AIP) representations extending from superior to inferior postcentral sulcus (see S-ROIs LH-12 and LH-18 in Fig. 2.2). This order is opposite to the typical arrangement of face and hand representations in S-I, where the face is located inferior-lateral to the hand along the postcentral gyrus (Huang and Sereno, 2007; Huang et al., 2012). In some subjects, multiple additional representations of face or

hand are found posterior to areas VIP and AIP (e.g., see the right posterior parietal cortex of Subject 2 in Fig. 2.S2). Some of them are considered to be authentic because of low temporal variability, while some are rejected for high temporal variability. In the group-average map, hand (finger) representations extend from area AIP at the inferior postcentral sulcus into the superior postcentral gyrus (S-I), which is located anterior and inferior to the face representation (VIP) at the superior postcentral sulcus (Fig. 2.10). Notably, area VIP shows a higher probability of occurrence than that of the lower face representation in S-I. This is likely because VIP is important in integrating random or sequential tactile motion across large receptive fields on the face, while S-I prefers sustained and localized stimulation in small receptive fields (Huang et al., 2012; Sereno and Huang, 2006).

Multiple S-ROIs in non-sensorimotor regions are found to respond to tactile stimulation in a few subjects. Response in the visual cortex during tactile stimulation has been demonstrated in other studies (e.g., Merabet et al., 2007). In this study, S-ROIs in the primary visual cortex (V1) in both hemispheres of Subject 1 are eventually rejected due to moderate to high temporal variability (Fig. 2.2B), although they could potentially be involved in covert spatial attention of tactile motion. On the medial wall, S-ROIs LH-22 and RH-37 of Subject 1 and LH-22 of Subject 2 are retained although they show only

moderate temporal variability (Figs. 2.2B, 2.S2B). Some of them may overlap with the cingulate sulcus visual area (CSv) found to respond to optic-flow motion (Wall and Smith, 2008). In the middle temporal cortex, S-ROIs LH-6 and RH-18 of Subject 1 (Fig. 2.2B), S-ROIs LH-11 and RH-14 of Subject 2 (Fig. 2.S2B), S-ROI LH-14 of Subject 10 (Fig. 2.S10), and S-ROI LH-12 of Subject 16 (Fig. 2.S16) show low to moderate temporal variability. These S-ROIs may overlap with the medial superior temporal area (MST) important for processing multisensory motion (Beauchamp et al., 2007; Jiang et al., 2015). This region is tentatively labeled MT+ (middle temporal complex) in the group-average map (Fig. 2.10). Together, activation in the aforementioned visual and multisensory areas suggests that they may be involved in tactile spatial attention and forming mental imagery of tactile motion on the face or hands.

In this study, we demonstrated the use of a second-level measure, temporal variability, to further validate and differentiate S-ROIs initially identified by thresholding a linear statistical measure. This data-driven approach facilitates the selection and interpretation of atypical S-ROIs found in the frontal, occipital, and temporal cortices. We have also rejected some of the S-ROIs with high temporal variability in the primary sensorimotor cortex, although they were initially selected because they are statistically significant and located in presumably correct anatomical locations. Once an S-ROI has

been validated in an fMRI scan, its reproducibility can then be validated by repeated scans within the same subject. Cross-subject reproducibility of S-ROIs, particularly those retained with low to moderate temporal variability in non-sensorimotor cortex, can be further validated by surface-based and probabilistic atlases constructed using spherical averaging methods as demonstrated in previous and current studies (Fischl et al., 1999; Hagler et al., 2007; Van Essen and Dierker, 2007).

In summary, this study is our first step toward the construction of a more complete surface-based somatotopic atlas, with contours (S-ROIs) delineating cortical representations of different body parts in multiple regions of the sensorimotor network. The proposed second-level analyses examine temporal variation of the entire fMRI time series, circular statistics of phase angles at multiple levels, and spatial distribution of activation sites across subjects, which provide more comprehensive information for selecting and interpreting S-ROIs in response to tactile stimulation. These methods are easily generalizable for mapping other body parts and other sensory modalities in future fMRI experiments.

2.5 Acknowledgements

This work was supported by NIH Grant R01 MH 081990 to M.I.S. and R.-S.H. and UC San Diego Frontiers of Innovation Scholars Program (FISP) Project Fellowships to C.-F.C.

This chapter, in full, is a reprint of Chen, C.F., Kreutz-Delgado, K., Sereno, M.I., Huang, R.S., 2017. Validation of periodic fMRI signals in response to wearable tactile stimulation. NeuroImage 150:99-111. The dissertation author was the primary investigator and author of this paper. I want to thank Doctor Ruey-Song Huang for the guidance of the direction of the research and Professor Kenneth Kreutz-Delgado for making mathematical statements more rigorous and unambiguous. Also thank Professor Marty Sereno for FreeSurfer support and comments on the manuscript.

2.6 Supplementary materials

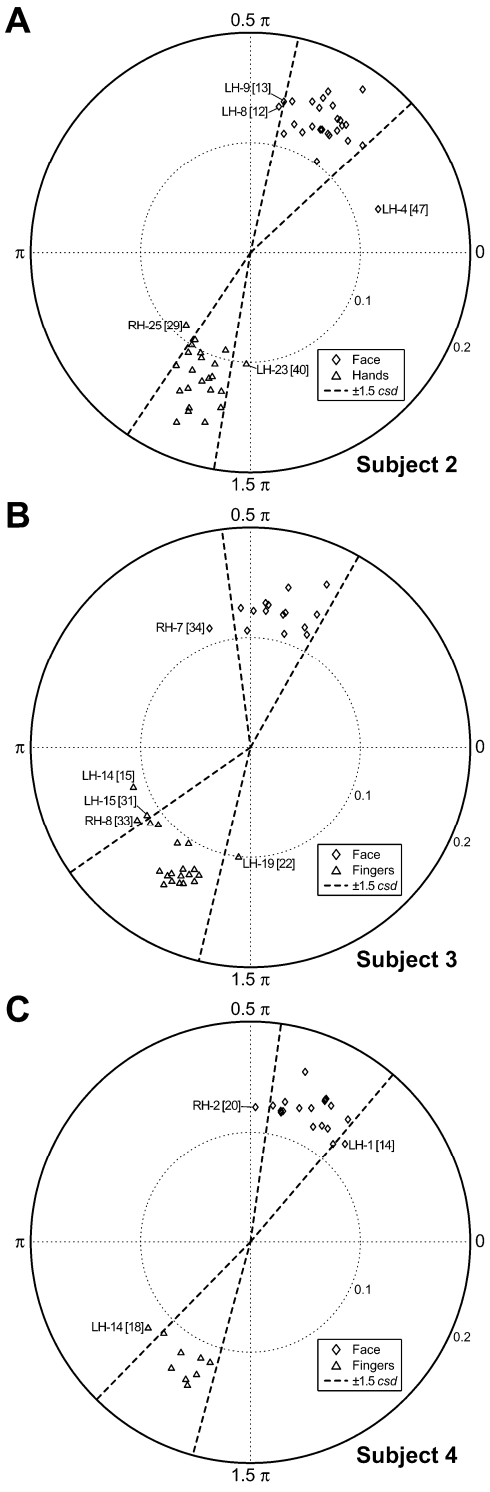

Fig. 2.S1: Distribution of S-ROI mean phase angles, $\overline{\theta}^{(r)}_{\text{trim}}(\omega_s)$, in Subjects 2-4. All conventions follow Fig. 2.7. Also see Tables 2.S2-2.S4.

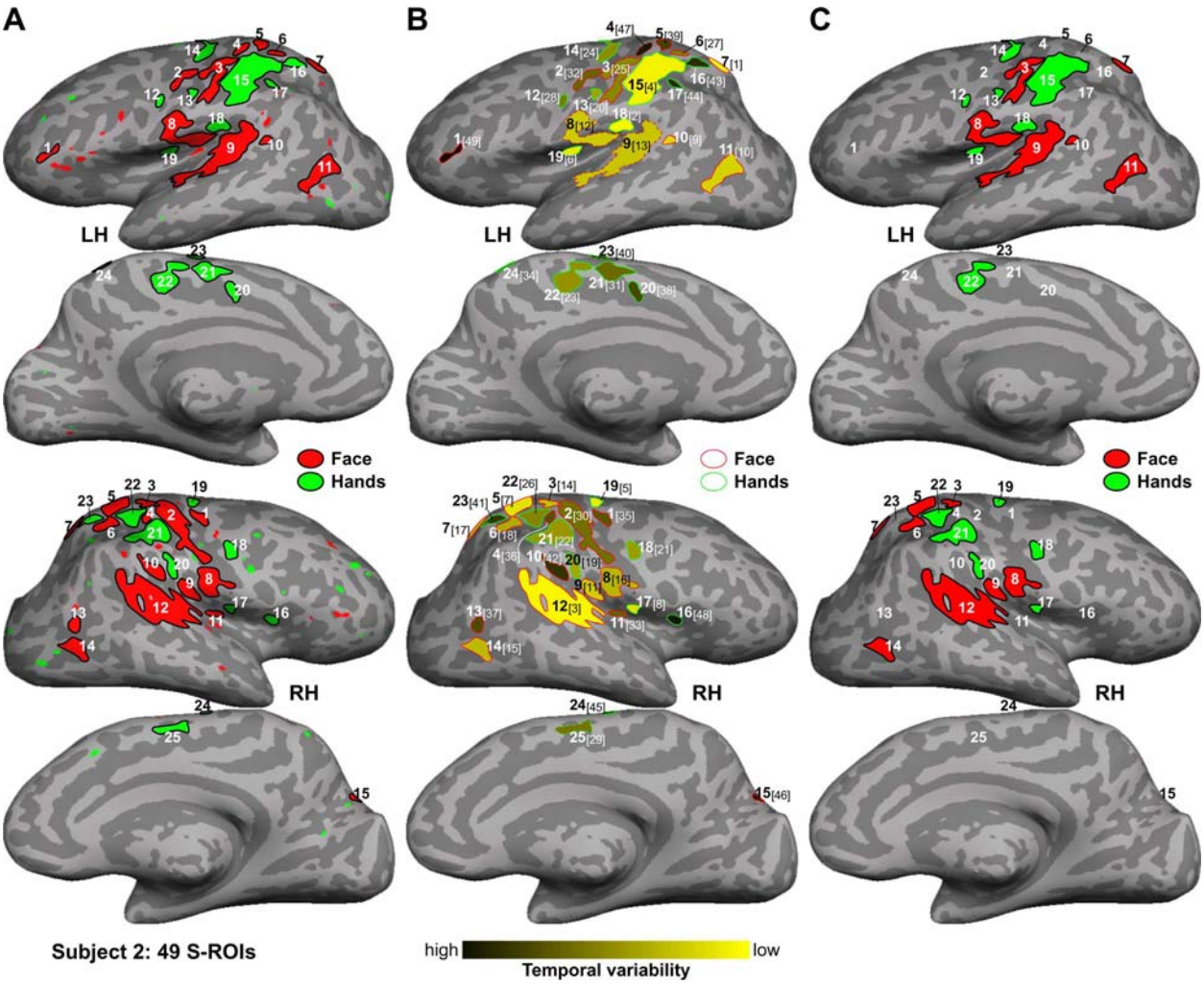

Fig. 2.S2: Selection of S-ROIs in Subject 2. All conventions follow Fig. 2.2.

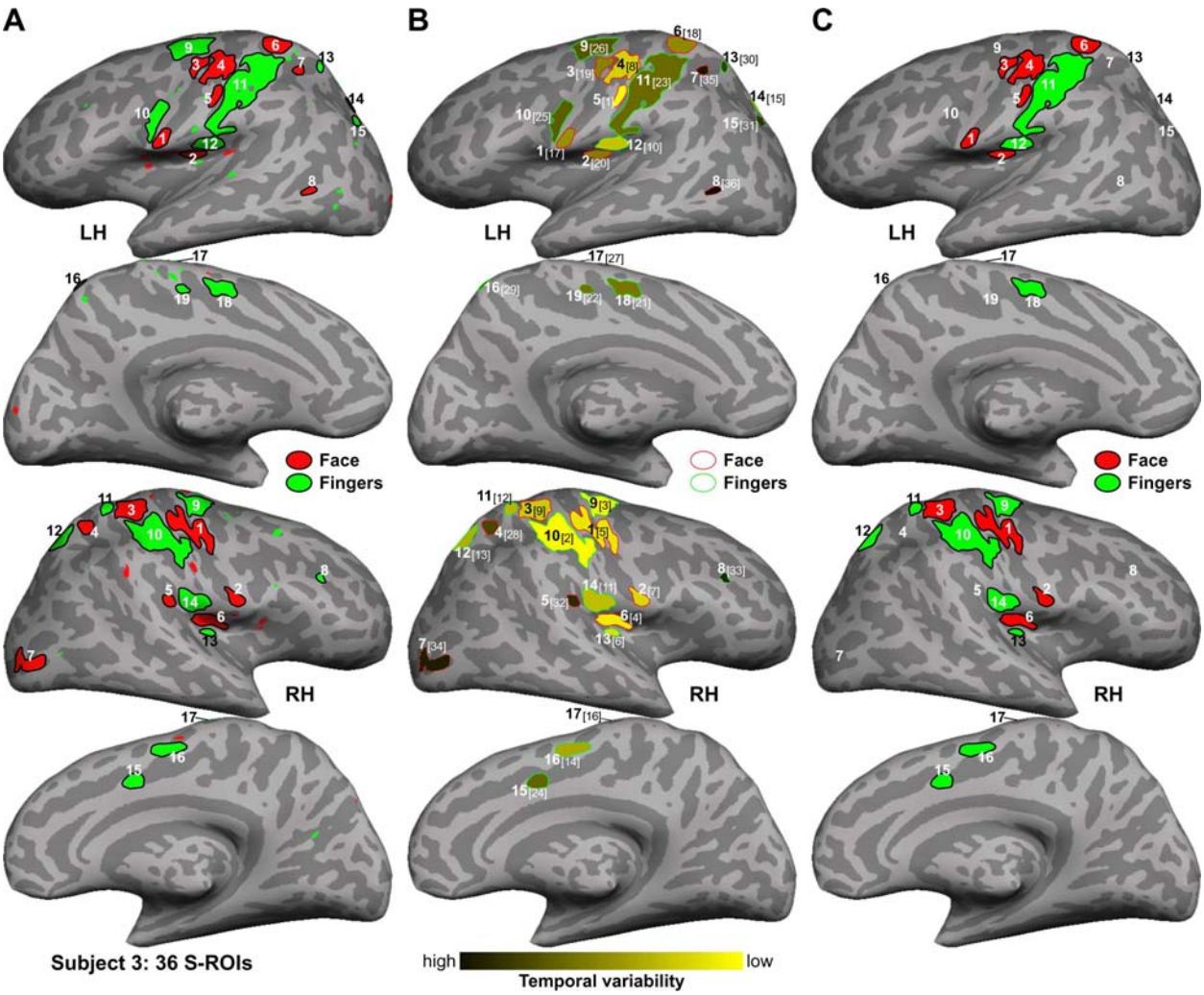

Fig. 2.S3: Selection of S-ROIs in Subject 3. All conventions follow Fig. 2.2.

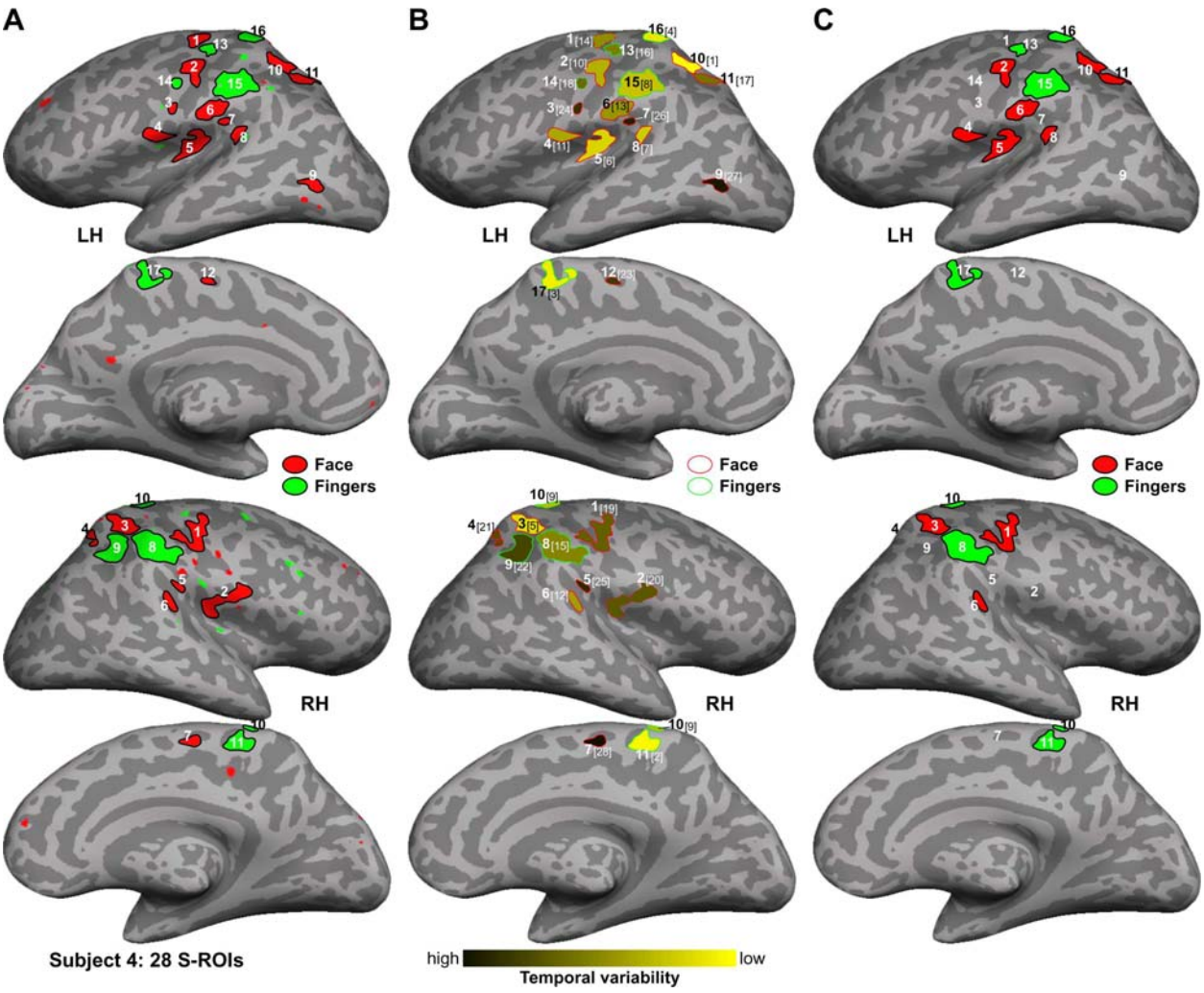

Fig. 2.S4: Selection of S-ROIs in Subject 4. All conventions follow Fig. 2.2.

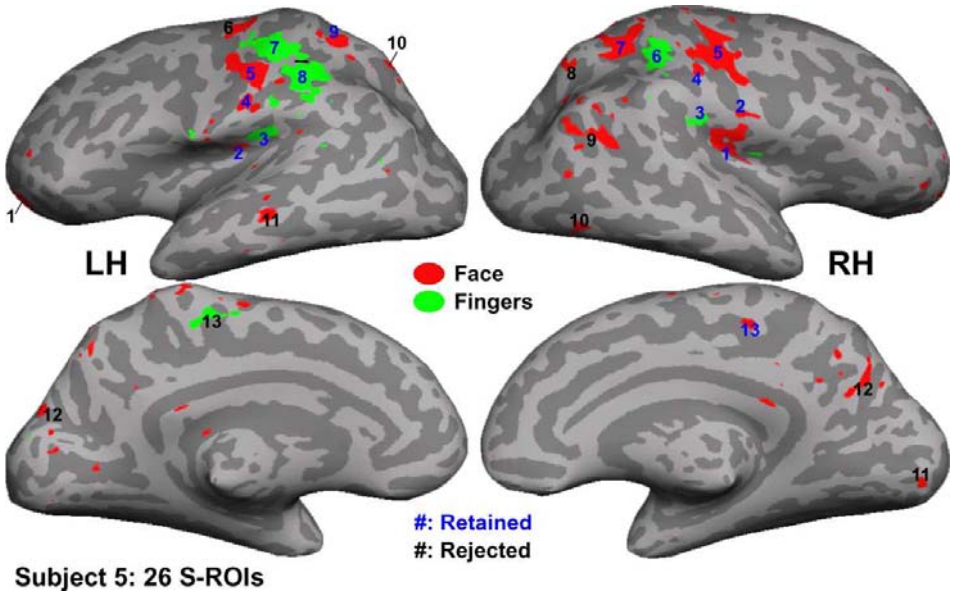

Fig. 2.S5: Selection of S-ROIs in Subject 5. Activation maps are thresholded at $p = 0.001$ (uncorrected). Each indexed S-ROI has a surface area larger than 30 mm^2. Retained and rejected S-ROIs are respectively indicated in blue and black indices (see Table 2.S5).

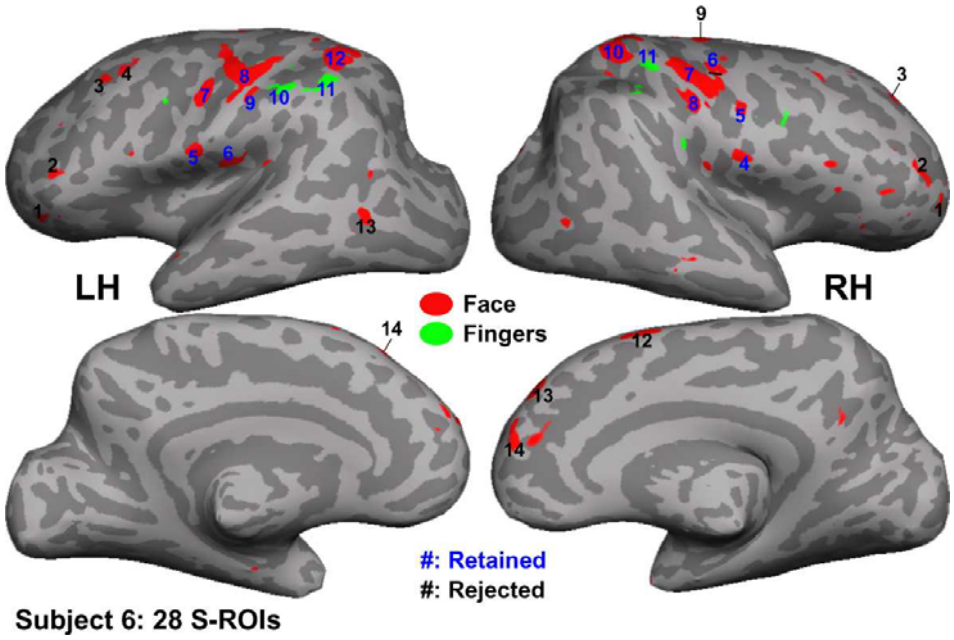

Fig. 2.S6: Selection of S-ROIs in Subject 6. See Table 2.S6 for retained and rejected S-ROIs. All conventions follow Fig. 2.S5.

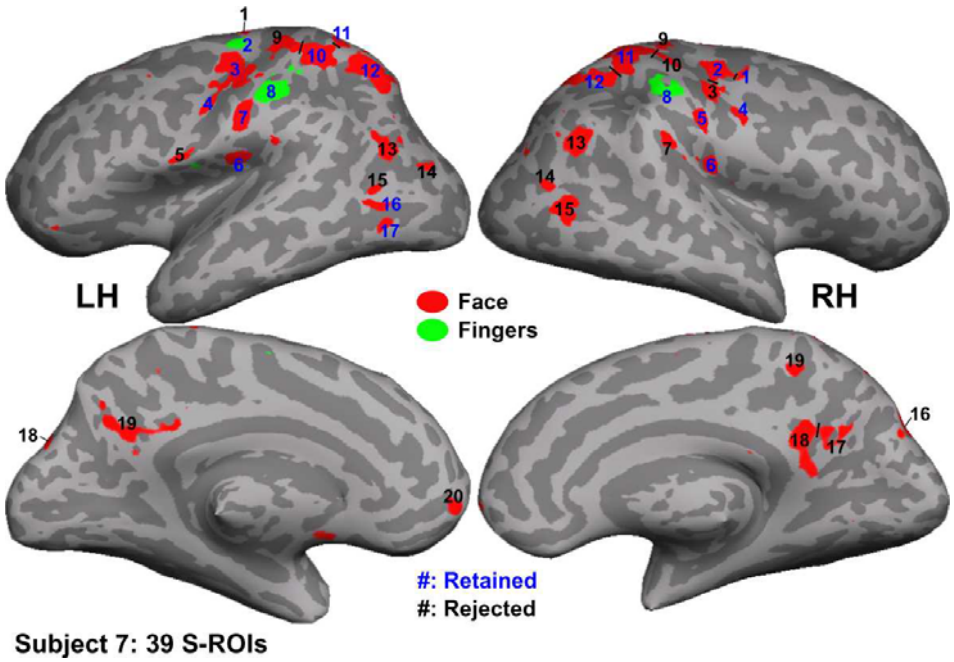

Fig. 2.S7: Selection of S-ROIs in Subject 7. See Table 2.S7 for retained and rejected S-ROIs. All conventions follow Fig. 2.S5.

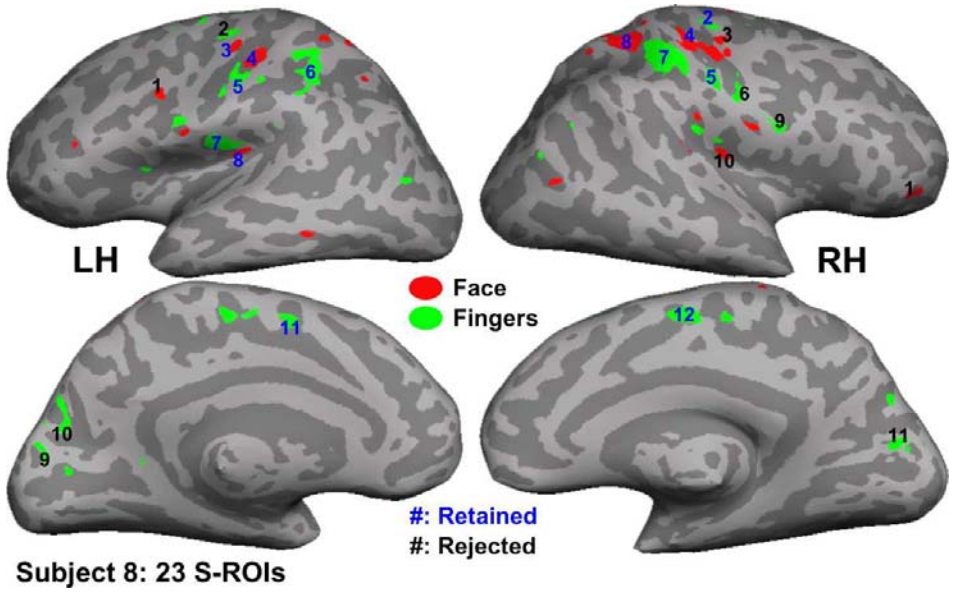

Fig. 2.S8: Selection of S-ROIs in Subject 8. See Table 2.S8 for retained and rejected S-ROIs. All conventions follow Fig. 2.S5.

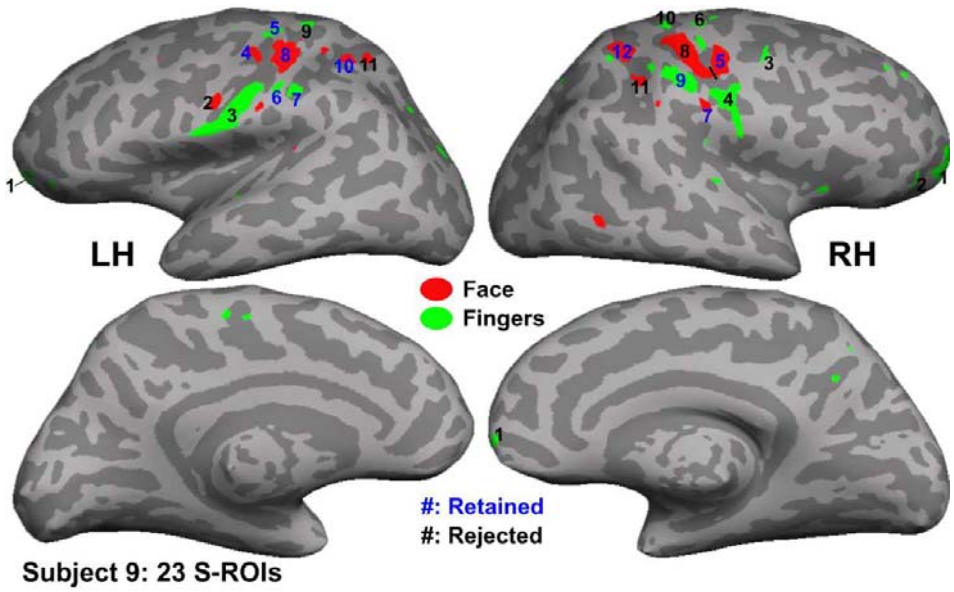

Fig. 2.S9: Selection of S-ROIs in Subject 9. See Table 2.S9 for retained and rejected S-ROIs. All conventions follow Fig. 2.S5.

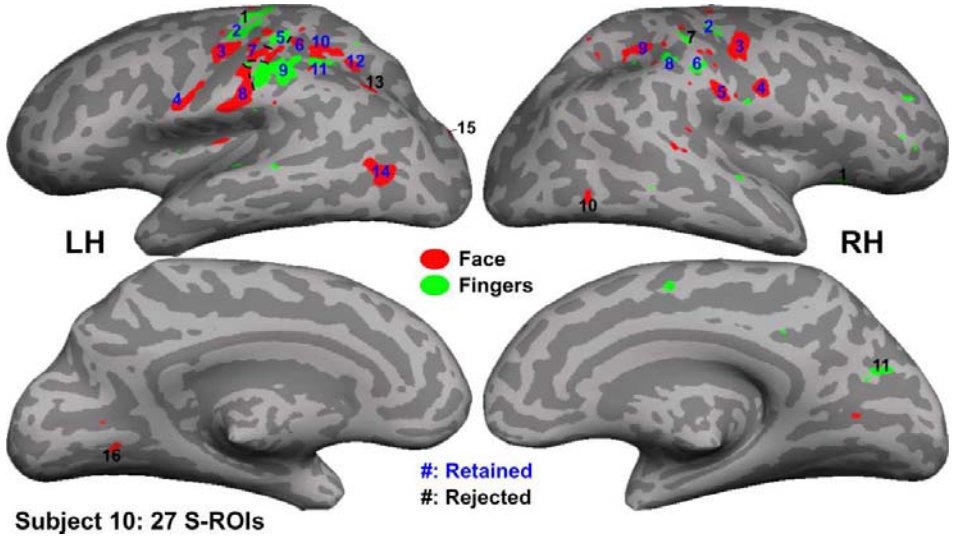

Fig. 2.S10: Selection of S-ROIs in Subject 10. See Table 2.S10 for retained and rejected S-ROIs. All conventions follow Fig. 2.S5.

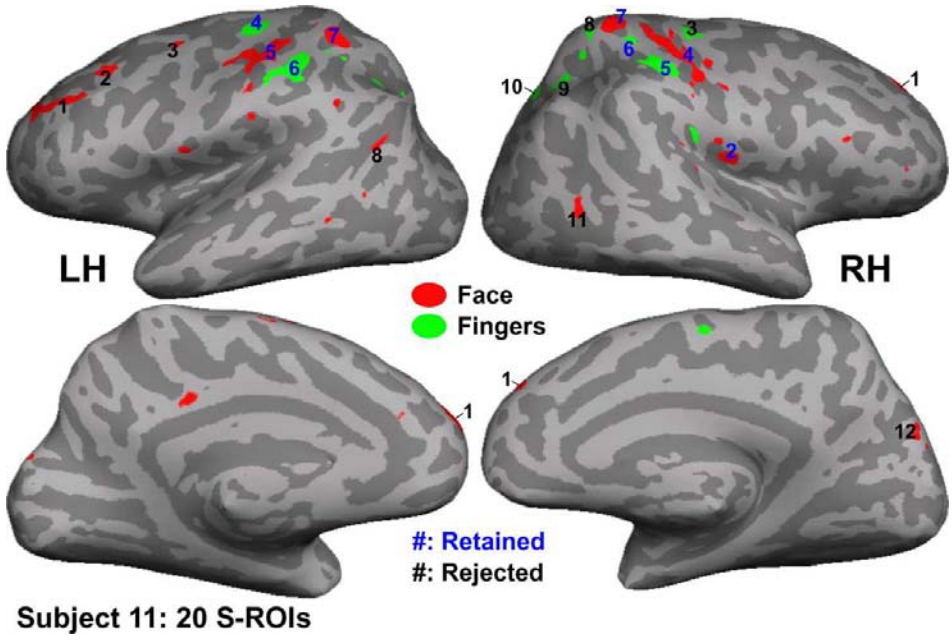

Fig. 2.S11: Selection of S-ROIs in Subject 11. See Table 2.S11 for retained and rejected S-ROIs. All conventions follow Fig. 2.S5.

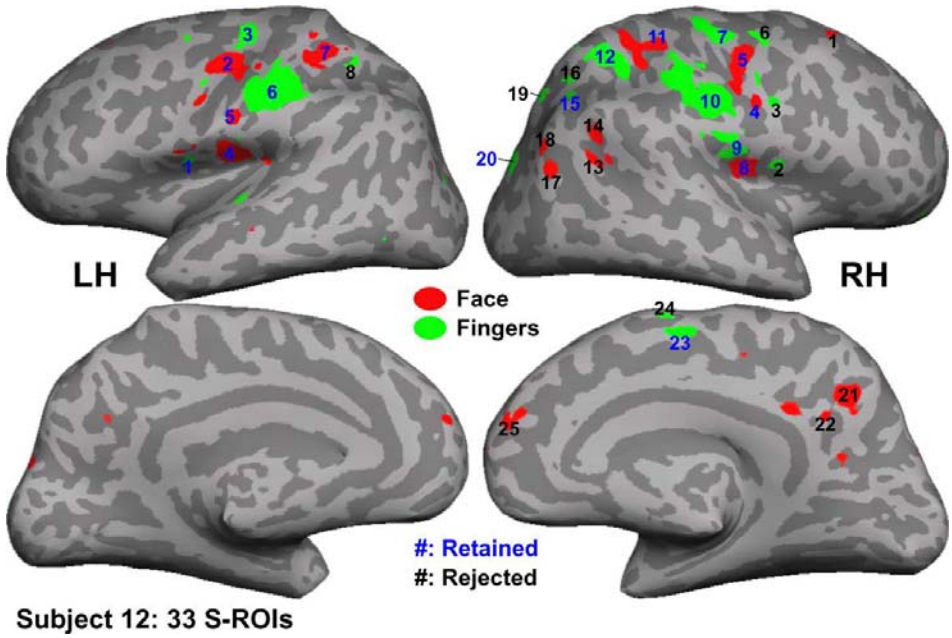

Fig. 2.S12: Selection of S-ROIs in Subject 12. See Table 2.S12 for retained and rejected S-ROIs. All conventions follow Fig. 2.S5.

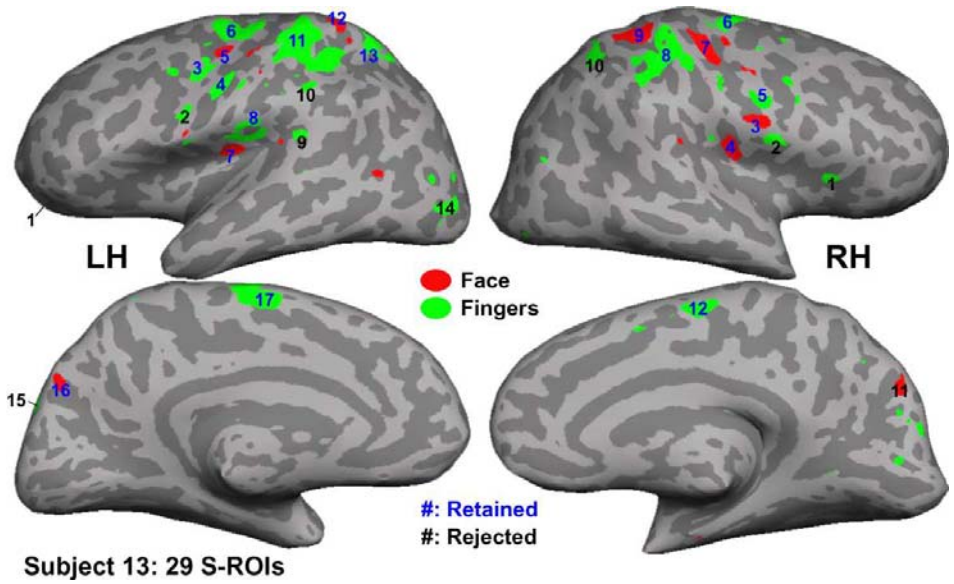

Fig. 2.S13: Selection of S-ROIs in Subject 13. See Table 2.S13 for retained and rejected S-ROIs. All conventions follow Fig. 2.S5.

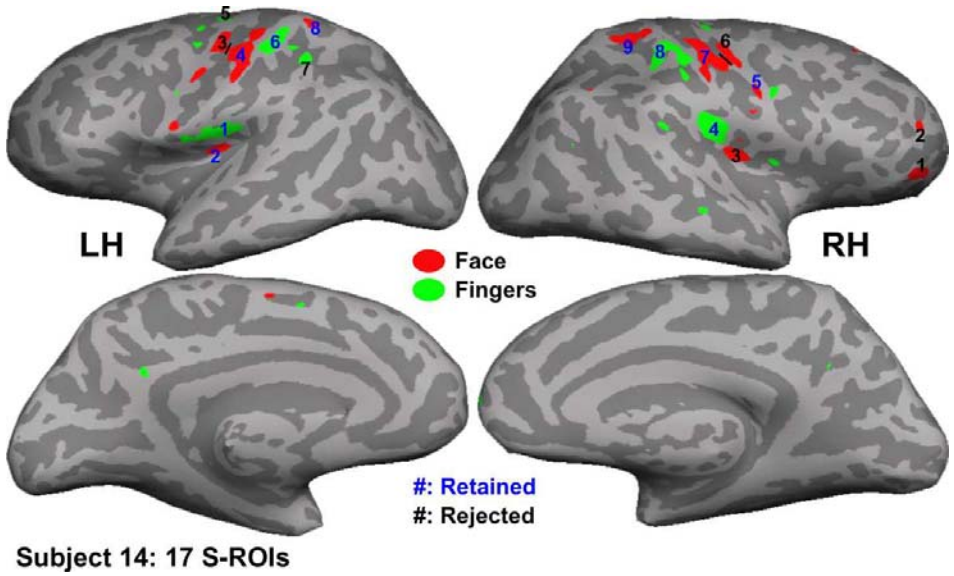

Fig. 2.S14: Selection of S-ROIs in Subject 14. See Table 2.S14 for retained and rejected S-ROIs. All conventions follow Fig. 2.S5.

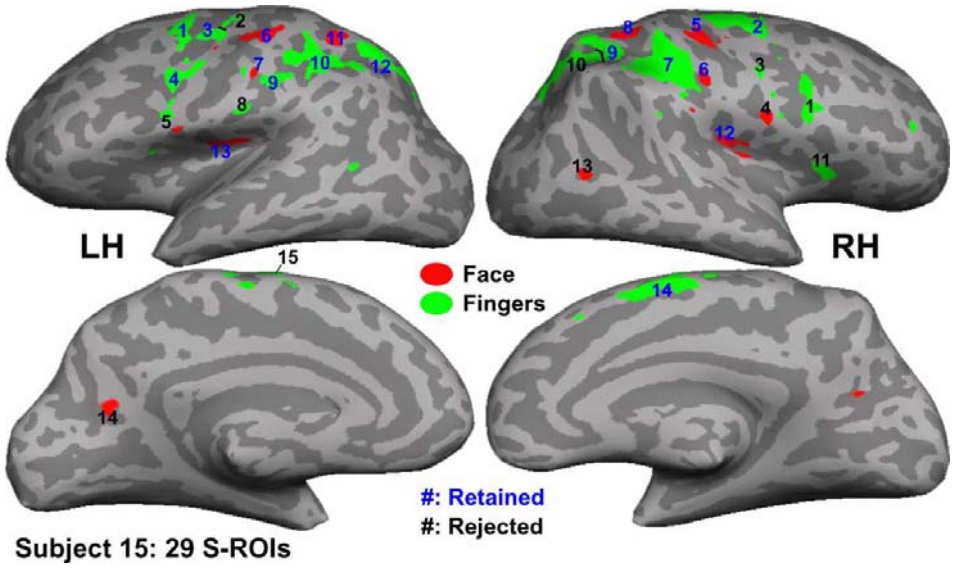

Fig. 2.S15: Selection of S-ROIs in Subject 15. See Table 2.S15 for retained and rejected S-ROIs. All conventions follow Fig. 2.S5.

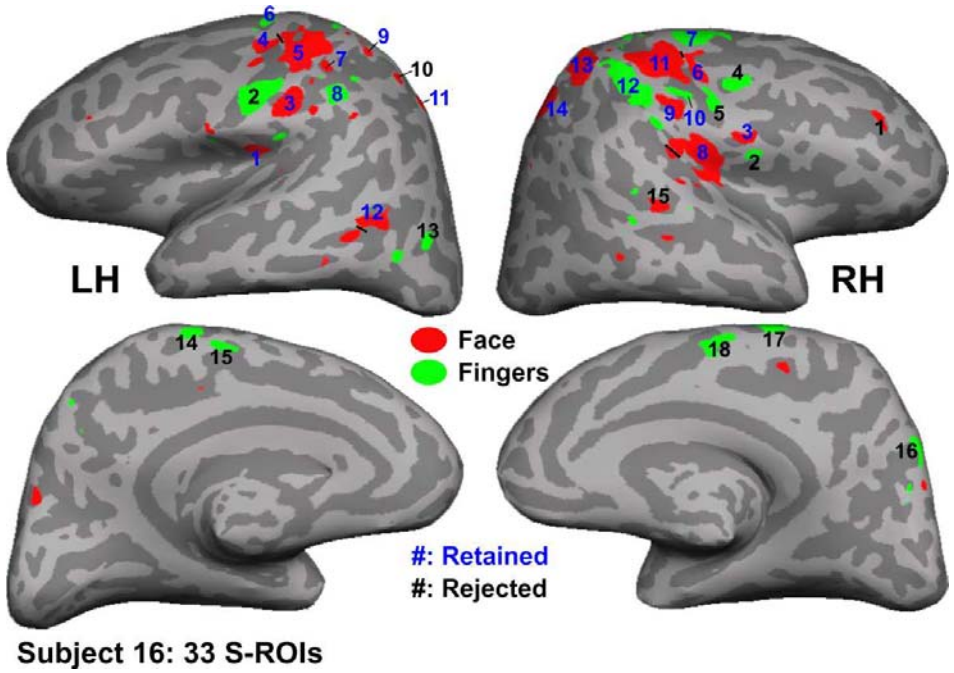

Fig. 2.S16: Selection of S-ROIs in Subject 16. See Table 2.S16 for retained and rejected S-ROIs. All conventions follow Fig. 2.S5.

Table 2.S1: Selection of S-ROIs in Subject 1 (Fig. 2.2).

Left hemisphere					Right hemisphere				
Region	S-ROI	Angle (°)	*L*-value	Rank	Region	S-ROI	Angle (°)	*L*-value	Rank
C	LH-2	53.49	1.47	9	C	RH-10	48.79	1.33	3
	LH-7	46.5	2.46	45		RH-12	51.07	1.38	4
	LH-8	67.18	2.63	53		RH-13	61.14	1.25	1
	LH-9	62.96	1.43	6		RH-31‡	197.61	2.2	35
	LH-10	45.86	1.92	29		RH-32	214.34	1.26	2
	LH-11	56.37	2.53	51		RH-33	197.38	1.67	18
	LH-19	188.78	1.94	30		RH-34	212.34	1.73	19
	LH-20	222.41	1.61	12	P	RH-14	41.55	1.86	24
	LH-21	212.06	1.46	8		RH-15	50.38	1.66	15
P	LH-12	46.91	1.66	16		RH-16	60.9	2.01	32
	LH-13	159.78	2.64	54		RH-35	206.63	1.67	17
	LH-14	74.16	2.41	42	I/T	RH-11	57.77	1.95	31
	LH-18	216.29	1.63	14		RH-17	68.48	2.34	39
I/T	LH-3	63.43	2.33	38		RH-18	32.05	2.12	33
	LH-4	71.49	1.74	21	F	RH-1‡	67.72	1.61	11
	LH-5	60.67	2.68	56		RH-2	128.62	2.76	59
	LH-6	58.51	2.25	36		RH-3	68.34	2.43	43
F	LH-1‡	66.05	1.53	10		RH-4‡	55.97	1.88	26
O	LH-15	59.18	2.73	58		RH-5	62.61	2.49	46
	LH-16	64.35	2.99	63		RH-6	125.73	2.91	62
	LH-17	142.21	2.67	55		RH-7	60.55	2.79	60
	LH-22	213.29	1.9	28		RH-8‡	64.04	1.88	25
	LH-23‡	191.22	2.19	34		RH-9	164.04	1.77	23
						RH-28	249.71	1.44	7
						RH-29	255.75	1.41	5
						RH-30‡	194.85	1.62	13
					O	RH-19	80.82	2.35	40
						RH-20‡	67.94	1.76	22
						RH-21	94.61	2.49	47
						RH-22	114.43	2.51	49
						RH-23	126.25	2.6	52
						RH-24	78.63	2.5	48
						RH-25‡	69.24	2.26	37
						RH-26	66.29	2.87	61
						RH-27	65.12	2.43	44
						RH-36	214.95	1.89	27
						RH-37	211.74	1.74	20
						RH-38	217.8	2.53	50
						RH-39	192.04	2.7	57
						RH-40	188.1	2.4	41

Total S-ROIs: 63.

S-ROIs sorted by brain regions: C: Pre- and post-central regions; P: posterior parietal regions; I/T: insular and temporal regions; F: frontal regions; O: other regions.

Unmarked: Retained S-ROIs. Shaded: Rejected S-ROIs due to high variability and/or deviant mean phase angles. Shaded ‡: S-ROIs included in constructing the initial group-average map (Fig. 2.10A) but rejected in the final group-average map (Fig. 2.10B).

Table 2.S2: Selection of S-ROIs in Subject 2 (Fig. 2.S2).

Left hemisphere					Right hemisphere				
Region	S-ROI	Angle (°)	L-value	Rank	Region	S-ROI	Angle (°)	L-value	Rank
	LH-2	66.67	1.71	32		RH-1	56.97	1.76	35
	LH-3	71.19	1.59	25		RH-2‡	55.84	1.63	30
	LH-4	18.68	2.49	47		RH-3	43.76	1.5	14
	LH-5	60.78	1.94	39	C	RH-8	74.59	1.51	16
C	LH-8	78.98	1.42	12		RH-18	248.65	1.56	21
	LH-12	245.32	1.63	28		RH-19	258.18	1.33	5
	LH-13	252.31	1.55	20		RH-24	255.74	2.29	45
	LH-14	259.19	1.58	24		RH-4	53.24	1.77	36
	LH-23	267.88	2.01	40		RH-5	55.51	1.34	7
	LH-6‡	64.29	1.61	27		RH-6	64.89	1.54	18
	LH-7	56.98	1.17	1	P	RH-7	59.82	1.53	17
P	LH-15	246.48	1.29	4		RH-21	248.44	1.56	22
	LH-16	252.92	2.06	43		RH-22	254.99	1.6	26
	LH-17	243.72	2.15	44		RH-23	251.7	2.01	41
	LH-24	243.58	1.75	34		RH-9	64.57	1.41	11
	LH-9	77.55	1.44	13		RH-10	54.24	2.02	42
	LH-10	60.42	1.36	9		RH-11	63.91	1.75	33
I/T	LH-11	56.13	1.4	10		RH-12	67.77	1.26	3
	LH-18	242.92	1.22	2	I/T	RH-13	48.94	1.79	37
	LH-19	236.74	1.33	6		RH-14	54.64	1.5	15
F	LH-1	53.92	2.66	49		RH-16	237.59	2.59	48
	LH-20	238.12	1.86	38		RH-17	237.59	1.36	8
O	LH-21	253.84	1.67	31		RH-20	249.34	1.55	19
	LH-22	245.05	1.56	23	O	RH-15	74.34	2.36	46
						RH-25‡	228.31	1.63	29

Total S-ROIs: 49. All conventions follow Table 2.S1.

Table 2.S3: Selection of S-ROIs in Subject 3 (Fig. 2.S3).

Left hemisphere					Right hemisphere				
Region	S-ROI	Angle (°)	L-value	Rank	Region	S-ROI	Angle (°)	L-value	Rank
C	LH-1	82.81	1.77	17	C	RH-1	65.68	1.47	5
	LH-3	63.42	1.79	19		RH-2	84	1.51	7
	LH-4	83.56	1.53	8		RH-9	239.64	1.39	3
	LH-5	76.2	1.27	1		RH-17	248.11	1.7	16
	LH-9	238.03	2.21	26	P	RH-3	64.92	1.55	9
	LH-10	241.05	2.16	25		RH-4	88.72	2.34	28
	LH-17	245.36	2.23	27		RH-10	237.79	1.37	2
P	LH-6	76.64	1.79	18		RH-11	233.81	1.58	12
	LH-7	73.42	2.96	35		RH-12	217.11	1.58	13
	LH-11	244.32	1.99	23	I/T	RH-5	63.43	2.55	32
	LH-13	237.33	2.48	30		RH-6	75.46	1.46	4
	LH-14	198.76	1.65	15		RH-13	241.67	1.49	6
	LH-15	213.27	2.53	31		RH-14	242.5	1.56	11
	LH-16	220.02	2.44	29	F	RH-8	212.74	2.87	33
I/T	LH-2	93.97	1.86	20	O	RH-7	109.01	2.96	34
	LH-8	91.62	3.8	36		RH-15	232.7	2.07	24
	LH-12	237.21	1.56	10		RH-16	247.36	1.64	14
O	LH-18	243.8	1.95	21					
	LH-19	263.84	1.98	22					

Total S-ROIs: 36. All conventions follow Table 2.S1.

Table 2.S4: Selection of S-ROIs in Subject 4 (Fig. 2.S4).

Left hemisphere					Right hemisphere				
Region	S-ROI	Angle (°)	L-value	Rank	Region	S-ROI	Angle (°)	L-value	Rank
C	LH-1	46.15	1.55	14	C	RH-1	76.04	1.7	19
	LH-2	69.98	1.46	10		RH-10	226.51	1.4	9
	LH-3	59.4	1.87	24	P	RH-3	72.18	1.26	5
	LH-6	51.54	1.48	13		RH-4	65.57	1.72	21
	LH-13	247.83	1.64	16		RH-8	244.71	1.58	15
	LH-14	220.07	1.68	18		RH-9	251.42	1.76	22
	LH-16	237.83	1.23	4	I/T	RH-2	87.9	1.71	20
P	LH-10	62.13	1.02	1		RH-5	62.22	1.93	25
	LH-11	49.95	1.65	17		RH-6	62.3	1.48	12
	LH-15	246.19	1.39	8	O	RH-7	77.02	2.64	28
I/T	LH-4	80.66	1.47	11		RH-11	246.79	1.22	2
	LH-5	76.14	1.29	6					
	LH-7	55.81	2.03	26					
	LH-8	61.53	1.37	7					
	LH-9	58.5	2.07	27					
O	LH-12	76.74	1.8	23					
	LH-17	237.82	1.23	3					

Total S-ROIs: 28. All conventions follow Table 2.S1.

Table 2.S5: Selection of S-ROIs in Subject 5 (Fig. 2.S5).

Left hemisphere					Right hemisphere				
Region	S-ROI	Angle (°)	L-value	Rank	Region	S-ROI	Angle (°)	L-value	Rank
C	LH-4	89.71	1.62	6	C	RH-2	97.24	1.65	7
	LH-5	92.14	1.35	2		RH-4	80.08	1.35	3
	LH-6	87.49	2.41	21		RH-5	87.76	1.2	1
	LH-7	237.74	1.55	4	P	RH-6	236.71	1.86	12
P	LH-8	220.16	2.04	16		RH-7	81.67	1.94	14
	LH-9	85.23	1.61	5		RH-8	100.78	2.24	19
	LH-10	98.42	2.47	22	I/T	RH-1	95.54	1.94	13
I/T	LH-2	86	1.7	9		RH-3	239.9	1.82	10
	LH-3	243.83	1.83	11		RH-9	85.42	2.84	25
	LH-11	66.49	2.21	18		RH-10	98.63	3.16	26
F	LH-1‡	74.74	1.68	8	O	RH-11	87.27	2.76	24
O	LH-12	82.24	2.09	17		RH-12	99.77	2.75	23
	LH-13	231.8	2.31	20		RH-13	95.74	1.96	15

Total S-ROIs: 26. All conventions follow Table 2.S1.

Table 2.S6: Selection of S-ROIs in Subject 6 (Fig. 2.S6).

Left hemisphere					Right hemisphere				
Region	S-ROI	Angle (°)	L-value	Rank	Region	S-ROI	Angle (°)	L-value	Rank
C	LH-5	75.9	2.38	10		RH-5	68.56	2.02	3
	LH-7	55	2.1	4		RH-6	66.08	2.38	9
	LH-8	72.25	2.5	13	C	RH-7	63.05	2.52	14
	LH-9	72.24	2.4	11		RH-8	65.3	1.96	2
P	LH-10	218.62	2.54	16		RH-9‡	74.31	2.54	15
	LH-11	200.38	2.35	8	P	RH-10	70.32	2.3	7
	LH-12	74.29	2.24	5		RH-11	223.53	1.39	1
I/T	LH-6	59.35	2.3	6	I/T	RH-4	66.12	2.72	19
	LH-13	79.57	2.72	18	F	RH-1	96.94	2.44	12
F	LH-1	108.46	4.07	28		RH-2‡	85.74	2.61	17
	LH-2	35.65	2.98	22		RH-3	84.92	3.63	27
	LH-3	100.87	2.94	21		RH-13	57.57	3.24	25
	LH-4	62.47	2.84	20		RH-14	48.03	3.06	24
	LH-14	51.93	3.63	26	O	RH-12	56.16	2.99	23

Total S-ROIs: 28. All conventions follow Table 2.S1.

Table 2.S7: Selection of S-ROIs in Subject 7 (Fig. 2.S7).

Left hemisphere					Right hemisphere				
Region	S-ROI	Angle (°)	L-value	Rank	Region	S-ROI	Angle (°)	L-value	Rank
C	LH-1	63.3	2.12	26	C	RH-1	74.37	1.62	8
	LH-2	288.76	1.42	4		RH-2	79.75	1.44	5
	LH-3	75.26	1.72	13		RH-3	85.23	1.98	23
	LH-4	73.35	1.63	11		RH-4	72.77	1.82	16
	LH-5	84.17	1.68	12		RH-5	61.67	1.75	14
	LH-7	58.12	1.5	6		RH-9	90.66	2.31	31
	LH-9‡	77.22	1.93	21		RH-10‡	82.67	2.02	24
P	LH-8	280.05	1.34	2	P	RH-8	286.2	1.87	18
	LH-10	65.98	1.32	1		RH-11	68.46	1.35	3
	LH-11	67.81	2.05	25		RH-12	60.31	1.8	15
	LH-12	61.54	1.62	10	I/T	RH-6	72.81	1.55	7
I/T	LH-6	78.14	1.62	9		RH-7	43.22	2.29	29
	LH-13	62.95	2.17	27		RH-13	59.14	2.34	32
	LH-15	62.09	2.6	38	O	RH-14	72.94	2.3	30
	LH-16	62.35	1.86	17		RH-15	52.67	2.39	33
	LH-17	65.55	1.89	19		RH-16	63.77	2.25	28
O	LH-14	70.3	2.51	36		RH-17‡	64.94	1.89	20
	LH-18	68.13	2.4	35		RH-18	65.94	2.54	37
	LH-19	66.17	2.39	34		RH-19‡	72	1.97	22
	LH-20	82.08	2.78	39					

Total S-ROIs: 39. All conventions follow Table 2.S1.

Table 2.S8: Selection of S-ROIs in Subject 8 (Fig. 2.S8).

Left hemisphere					Right hemisphere				
Region	S-ROI	Angle (°)	L-value	Rank	Region	S-ROI	Angle (°)	L-value	Rank
C	LH-2‡	214.66	2.27	13		RH-2	232.83	1.97	10
	LH-3	54.1	1.3	1		RH-3	45.2	2.63	18
	LH-4	49.76	1.37	3	C	RH-4	52.48	1.43	4
	LH-5	244.57	1.95	9		RH-5	253.15	1.52	6
P	LH-6	226.89	2.25	12		RH-6	265.35	2.52	16
I/T	LH-7	226.88	2.47	15	P	RH-7	222.57	1.89	7
	LH-8	50.98	1.32	2		RH-8	52.36	1.45	5
F	LH-1	43.67	2.62	17	I/T	RH-10	65.3	1.89	8
O	LH-9	N/A	N/A	22	F	RH-1	64.45	3.95	21
	LH-10	N/A	N/A	22		RH-9	221.26	3.39	20
	LH-11	213.26	2.19	11	O	RH-11	325.3	3.01	19
						RH-12	231.91	2.36	14

Total S-ROIs: 23. All conventions follow Table 2.S1.

Table 2.S9: Selection of S-ROIs in Subject 9 (Fig. 2.S9).

Left hemisphere					Right hemisphere				
Region	S-ROI	Angle (°)	L-value	Rank	Region	S-ROI	Angle (°)	L-value	Rank
	LH-2	66.96	1.93	16		RH-3	247.99	1.98	18
	LH-3‡	276.02	1.7	10		RH-4	278.53	1.81	13
	LH-4	66.52	1.48	4		RH-5	51.11	1.64	9
C	LH-5	250.78	1.61	8	C	RH-6	258.46	2.18	21
	LH-6	262.8	1.59	7		RH-7	56.54	1.78	12
	LH-8	63.68	1.46	3		RH-8	71.93	1.35	1
	LH-9	256.82	1.97	17		RH-10	249.15	1.99	19
	LH-7	254.33	1.87	14		RH-9	258.16	1.51	5
P	LH-10	51.37	1.78	11	P	RH-11	48.65	2.48	23
	LH-11	59.89	2.11	20		RH-12	54.03	1.88	15
F	LH-1‡	257.8	1.41	2	F	RH-1‡	262.38	1.54	6
						RH-2	269.4	2.39	22

Total S-ROIs: 23. All conventions follow Table 2.S1.

Table 2.S10: Selection of S-ROIs in Subject 10 (Fig. 2.S10).

Left hemisphere					Right hemisphere				
Region	S-ROI	Angle (°)	L-value	Rank	Region	S-ROI	Angle (°)	L-value	Rank
	LH-1	306.33	2.05	21		RH-2	269.13	1.62	11
	LH-2	297.40	1.73	14		RH-3	46.56	1.31	3
	LH-3	51.80	1.23	2	C	RH-4	41.91	1.45	4
C	LH-4	44.09	1.19	1		RH-5	36.83	1.45	5
	LH-5	317.27	1.93	20		RH-6	276.28	1.78	15
	LH-7	16.53	1.57	9		RH-7	329.91	2.46	25
	LH-8	24.8	1.59	10	P	RH-8	257.27	1.82	18
	LH-6	21.74	1.48	6		RH-9	34.26	1.63	13
	LH-9	268.17	1.5	7	I/T	RH-10	34.18	2.12	23
P	LH-10	34.07	1.62	12	F	RH-1	335.91	2.07	22
	LH-11	326.76	1.78	16	O	RH-11	245.7	2.54	26
	LH-12	57.35	1.55	8					
	LH-13	33.08	2.62	27					
I/T	LH-14	44.72	1.78	17					
O	LH-15‡	56.66	1.87	19					
	LH-16	3.86	2.36	24					

Total S-ROIs: 27. All conventions follow Table 2.S1.

Table 2.S11: Selection of S-ROIs in Subject 11 (Fig. 2.S11).

Left hemisphere					Right hemisphere				
Region	S-ROI	Angle (°)	L-value	Rank	Region	S-ROI	Angle (°)	L-value	Rank
C	LH-4	253.44	2.56	10	C	RH-3	259.5	2.75	15
	LH-5	80.05	2.23	7		RH-4	75.71	1.92	1
P	LH-6	249.13	2.54	9	P	RH-5	244.93	2.59	13
	LH-7	63.5	2.03	3		RH-6	260.21	2.21	6
I/T	LH-8	89.69	3.27	19		RH-7	70.94	1.93	2
F	LH-1‡	91.72	2.14	4		RH-8	265.92	2.95	17
	LH-2	88.72	2.65	14		RH-9	221.76	2.91	16
	LH-3	81.88	3.42	20		RH-10	215.64	3.15	18
					I/T	RH-2	89.67	2.23	8
						RH-11‡	86.92	2.57	11
					F	RH-1‡	95.86	2.18	5
					O	RH-12‡	85.89	2.58	12

Total S-ROIs: 20. All conventions follow Table S2.1.

Table 2.S12: Selection of S-ROIs in Subject 12 (Fig. 2.S12).

Left hemisphere					Right hemisphere				
Region	S-ROI	Angle (°)	L-value	Rank	Region	S-ROI	Angle (°)	L-value	Rank
C	LH-2	67.37	1.58	3	C	RH-3‡	241.23	2.64	18
	LH-3	229.71	2.69	20		RH-4	65.83	1.95	7
	LH-5	74.39	2.14	8		RH-5	69.65	1.77	6
P	LH-6	229.69	2.23	11		RH-7	234.31	2.22	10
	LH-7	71.59	1.26	2	P	RH-10	231.8	2.52	15
	LH-8	220.05	3.38	27		RH-11	79.83	1.61	4
I/T	LH-1	218.16	2.5	14		RH-12	222.89	2.69	19
	LH-4	66.44	1.08	1		RH-15	227.79	2.39	13
						RH-16	197.23	2.71	21
						RH-18	59.42	3.36	26
						RH-19	197.76	2.55	16
						RH-20	209.3	2.21	9
					I/T	RH-2	225.33	2.74	22
						RH-8	73.18	1.67	5
						RH-9	224.28	2.57	17
						RH-13	80.12	3.35	25
						RH-14	69.35	3.88	31
						RH-17	53.81	4.05	32
					F	RH-1	62.15	2.75	23
						RH-6	235.59	3.52	29
					O	RH-21	79.87	3.85	30
						RH-22	85.84	4.97	33
						RH-23	244.24	2.29	12
						RH-24	260.01	3.03	24
						RH-25	87.05	3.39	28

Total S-ROIs: 33. All conventions follow Table 2.S1.

Table 2.S13: Selection of S-ROIs in Subject 13 (Fig. 2.S13).

Left hemisphere					Right hemisphere				
Region	S-ROI	Angle (°)	*L*-value	Rank	Region	S-ROI	Angle (°)	*L*-value	Rank
C	LH-2	245.3	2.08	22	C	RH-3	70.6	1.51	9
	LH-3	246.92	1.49	6		RH-5	248.05	1.79	18
	LH-4	245.15	1.5	7		RH-6	241.88	1.54	11
	LH-5	72.18	1.59	15		RH-7	65.87	1.55	13
	LH-6	246.84	1.43	3	P	RH-8	242.68	1.51	8
P	LH-10	245.74	2.18	24		RH-9	70.57	1.26	2
	LH-11	245.37	1.61	16		RH-10	240.51	2.1	23
	LH-12	73.22	1.15	1	I/T	RH-2	243.84	2.2	25
	LH-13	236.84	1.79	17		RH-4	67.6	1.89	20
I/T	LH-7	78.82	1.54	10	F	RH-1	226.02	2.87	29
	LH-8	244.43	1.88	19	O	RH-11	90.42	1.47	4
	LH-9	234.94	2.6	28		RH-12	239.84	1.57	14
F	LH-1	262.39	2.2	26					
O	LH-14	243.66	1.99	21					
	LH-15	226.21	2.34	27					
	LH-16	76.92	1.54	12					
	LH-17	242.94	1.49	5					

Total S-ROIs: 29. All conventions follow Table 2.S1.

Table 2.S14: Selection of S-ROIs in Subject 14 (Fig. 2.S14).

Left hemisphere					Right hemisphere				
Region	S-ROI	Angle (°)	L-value	Rank	Region	S-ROI	Angle (°)	L-value	Rank
C	LH-3	69.66	2.01	12	C	RH-5	68.28	1.42	4
	LH-4	68.84	1.65	9		RH-6	76.95	2.2	14
	LH-5	244.3	2.25	16		RH-7	74.05	1.71	10
P	LH-6	267.36	1.65	8	P	RH-8	252.97	1.62	7
	LH-7	263.8	2.24	15		RH-9	76.3	1.32	2
	LH-8	68.87	1.26	1	I/T	RH-3	62.91	2.11	13
I/T	LH-1	263.1	1.32	3		RH-4	252.81	1.58	6
	LH-2	64.7	1.49	5	F	RH-1	71.82	2.69	17
						RH-2	46.06	1.77	11

Total S-ROIs: 17. All conventions follow Table 2.S1.

Table 2.S15: Selection of S-ROIs in Subject 15 (Fig. 2.S15).

Left hemisphere					Right hemisphere				
Region	S-ROI	Angle (°)	L-value	Rank	Region	S-ROI	Angle (°)	L-value	Rank
C	LH-2‡	277.66	1.03	1	C	RH-3‡	255.86	1.41	15
	LH-6	31.15	1.22	3		RH-4‡	56.93	1.41	14
	LH-7	36.72	1.29	6		RH-5	30.94	1.15	2
	LH-8	266.65	2.1	26		RH-6	41.29	1.39	13
P	LH-9	269.54	1.43	16	P	RH-7	258.6	1.76	23
	LH-10	265.62	1.34	9		RH-8	37.2	1.27	5
	LH-11	35.84	1.36	11		RH-9	259.39	1.64	21
	LH-12	262.9	1.26	4		RH-10	261.24	1.97	25
I/T	LH-13	29.89	1.53	19	I/T	RH-12	39.99	1.37	12
F	LH-1	272.2	1.3	7		RH-13	37.6	1.83	24
	LH-3	270.92	1.33	8	F	RH-1	266.09	2.2	29
	LH-4	266.41	1.45	17		RH-2	260.64	1.36	10
	LH-5‡	276.11	1.71	22		RH-11	269.03	2.1	27
O	LH-14	71.84	2.15	28	O	RH-14	269.06	1.51	18
	LH-15‡	275.51	1.57	20					

Total S-ROIs: 29. All conventions follow Table 2.S1.

Table 2.S16: Selection of S-ROIs in Subject 16 (Fig. 2.S16).

Left hemisphere					Right hemisphere				
Region	S-ROI	Angle (°)	L-value	Rank	Region	S-ROI	Angle (°)	L-value	Rank
C	LH-2	256.9	2.39	30	C	RH-5	259.29	2.57	32
	LH-3	69.49	1.4	8		RH-6	63.61	1.62	15
	LH-4	72.16	1.31	5		RH-9	62.48	1.47	11
	LH-5	69.91	1.23	3		RH-10	255.71	1.66	18
	LH-6	234.74	1.62	16		RH-11	67.18	1.36	6
P	LH-7	73.85	1.18	2	P	RH-12	246.35	1.08	1
	LH-8	244.24	1.91	23		RH-13	54.14	1.38	7
	LH-9	69.86	1.82	20		RH-14	64.12	1.58	14
	LH-10‡	39.65	1.9	22	I/T	RH-2	246.61	2.13	28
	LH-11	63.34	1.57	13		RH-3	64.78	1.46	10
I/T	LH-1	50.64	1.63	17		RH-8	52.02	1.41	9
	LH-12	50.98	1.53	12		RH-15‡	55.03	1.82	21
O	LH-13	260.59	2.31	29	F	RH-1	99.82	2.74	33
	LH-14	226.62	2.48	31		RH-4	235.6	1.95	24
	LH-15	239.65	2.02	26		RH-7	246.7	1.25	4
					O	RH-16‡	259.41	1.77	19
						RH-17	245.86	1.99	25
						RH-18	242.41	2.12	27

Total S-ROIs: 33. All conventions follow Table 2.S1.

2.7 References

Beauchamp, M.S., Yasar, N.E., Kishan, N., Ro T., 2007. Human MST but not MT responds to tactile stimulation. J. Neurosci. 27, 8261-8267. doi: 10.1523/JNEUROSCI.0754-07.2007.

Beckmann, C.F., 2012. Modelling with independent components. Neuroimage 62, 891-901. doi: 10.1016/j.neuroimage.2012.02.020.

Besle, J., Sánchez-Panchuelo, R.M., Bowtell, R., Francis, S., Schluppeck, D., 2013. Single-subject fMRI mapping at 7T of the representation of fingertips in S1: a comparison of event-related and phase-encoding designs. J. Neurophysiol. 109, 2293-2305. doi: 10.1152/jn.00499.2012.

Boynton, G.M., Engel, S.A., Heeger, D.J., 2012. Linear systems analysis of the fMRI signal. NeuroImage 62, 975-984. doi: 10.1016/j.neuroimage.2012.01.082.

Buxton, R.B., 2009. Introduction to Functional Magnetic Resonance Imaging: Principles and Techniques, second ed. Cambridge University Press, Cambridge.

Cox, R.W., 1996. AFNI: software for analysis and visualization of functional magnetic resonance neuroimages. Comput. Biomed. Res. 29, 162-173. doi: 10.1006/cbmr.1996.0014.

Dale, A.M., Fischl, B., Sereno, M.I., 1999. Cortical surface-based analysis. I. Segmentation and surface reconstruction. NeuroImage 9, 179-194. doi: 10.1006/nimg.1998.0395.

Disbrow, E., Roberts, T., Krubitzer, L., 2000. Somatotopic organization of cortical fields in the lateral sulcus of Homo sapiens: evidence for SII and PV. J. Comp. Neurol. 418, 1-21. doi: 10.1002/(SICI)1096-9861(20000228)418:1<1::AID-CNE1>3.0.CO;2-P.

Dresel, C., Parzinger, A., Rimpau, C., Zimmer, C., Ceballos-Baumann, A.O., Haslinger, B., 2008. A new device for tactile stimulation during fMRI. NeuroImage 39, 1094-1103. doi: 10.1016/j.neuroimage.2007.09.033.

Eickhoff, S.B., Grefkes, C., Fink, G.R., Zille, K., 2008. Functional lateralization of face, hand, and trunk representation in anatomically defined human somatosensory areas. Cereb. Cortex 18, 2820-2830. doi: 10.1093/cercor/bhn039.

Engel, S.A., Rumelhart, D.E., Wandell, B.A., Lee, A.T., Glover, G.H., Chichilnisky, E.J., Shadlen, M.N., 1994. fMRI of human visual cortex. Nature 369, 525. doi: 10.1038/369525a0.

Fink, G.R., Frackowiak, R.S., Pietrzyk, U., Passingham, R.E., 1997. Multiple nonprimary motor areas in the human cortex. J. Neurophysiol. 77, 2164-2174.

Fisher, N.I., 1993. Statistical Analysis of Circular Data, first ed. Cambridge University Press, Cambridge.

Fischl, B., Sereno, M.I., Tootell, R.B., Dale, A.M., 1999. High-resolution intersubject averaging and a coordinate system for the cortical surface. Hum. Brain Mapp. 8, 272-284. doi: 10.1002/(SICI)1097-0193(1999)8:4<272::AID-HBM10>3.0.CO;2-4.

Glasser, M.F., Coalson, T.S., Robinson, E.C., Hacker, C.D., Harwell, J., Yacoub, E., Ugurbil, K., Andersson, J., Beckmann, C.F., Jenkinson, M., Smith, S.M., Van Essen, D.C., 2016. A multi-modal parcellation of human cerebral cortex. Nature 536, 171-178. doi: 10.1038/nature18933.

Golaszewski, S.M., Seidl, M., Christova, M., Gallasch, E., Kunz, A.B., Nardone, R., Trinka, E., Gerstenbrand, F., 2012. Somatosensory stimulation in functional neuroimaging: a review. in: P. Bright (Ed.), Neuroimaging - Cognitive and Clinical Neuroscience. InTech, Rijeka, Croatia, pp. 333-352. doi: 10.5772/24003.

Grabska-Barwińska, A., Ng, B.S., Jancke, D., 2012. Orientation selective or not? - Measuring significance of tuning to a circular parameter. J. Neurosci. Methods 203, 1-9. doi: 10.1016/j.jneumeth.2011.08.026.

Graziano, M.S., Gandhi, S., 2000. Location of the polysensory zone in the precentral gyrus of anesthetized monkeys. Exp. Brain Res. 135, 259-266. doi: 10.1007/s002210000518.

Hagler, D.J. Jr., Riecke, L., Sereno, M.I., 2007. Parietal and superior frontal visuospatial maps activated by pointing and saccades. NeuroImage 35, 1562-1577. doi: 10.1016/j.neuroimage.2007.01.033.

Huang, R.S., Sereno, M.I., 2007. Dodecapus: An MR-compatible system for somatosensory stimulation. NeuroImage 34, 1060-1073. doi: 10.1016/j.neuroimage.2006.10.024.

Huang, R.S., Chen, C.F., Tran, A.T., Holstein, K.L., Sereno, M.I., 2012. Mapping multisensory parietal face and body areas in humans. Proc. Natl. Acad. Sci. U. S. A. 109, 18114-18119. doi: 10.1073/pnas.1207946109.

Jiang, F., Beauchamp, M.S., Fine, I., 2015. Re-examining overlap between tactile and visual motion responses within hMT+ and STS. NeuroImage 119, 187-196. doi: 10.1016/j.neuroimage.2015.06.056.

Levick, W.R., Thibos, L.N., 1982. Analysis of orientation bias in cat retina. J. Physiol. 329, 243-261. doi: 10.1113/jphysiol.1982.sp014301.

Mancini, F., Haggard, P., Iannetti, G.D., Longo, M.R., Sereno, M.I., 2012. Fine-grained nociceptive maps in primary somatosensory cortex. J. Neurosci. 32, 17155-17162. doi: 10.1523/JNEUROSCI.3059-12.2012.

Meier, J.D., Aflalo, T.N., Kastner, S., Graziano, M.S., 2008. Complex organization of human primary motor cortex: a high-resolution fMRI study. J. Neurophysiol. 100, 1800-1812. doi: 10.1152/jn.90531.2008.

Merabet, L.B., Swisher, J.D., McMains, S.A., Halko, M.A., Amedi, A., Pascual-Leone, A., Somers, D.C., 2007. Combined activation and deactivation of visual cortex during tactile sensory processing. J. Neurophysiol. 97, 1633-1641. doi: 10.1152/jn.00806.2006.

Miyamoto, J.J., Honda, M., Saito, D.N., Okada, T., Ono, T., Ohyama, K., Sadato, N., 2006. The representation of the human oral area in the somatosensory cortex: a functional MRI study. Cereb. Cortex 16, 669-675. doi: 10.1093/cercor/bhj012.

Penfield, W., Boldrey, E., 1937. Somatic motor and sensory representation in the cerebral cortex of man as studied by electrical stimulation. Brain 60, 389-443. doi: 10.1093/brain/60.4.389.

Ringach D.L., Shapley R.M., Hawken M.J., 2002. Orientation selectivity in macaque V1: diversity and laminar dependence. J. Neurosci. 22, 5639-5651.

Sereno, M.I., Huang, R.S., 2006. A human parietal face area contains aligned head-centered visual and tactile maps. Nat. Neurosci. 9, 1337-1343. doi:10.1038/nn1777.

Sereno, M.I., Dale, A.M., Reppas, J.B., Kwong, K.K., Belliveau, J.W., Brady, T.J., Rosen, B.R., Tootell, R.B., 1995. Borders of multiple visual areas in humans revealed by functional magnetic resonance imaging. Science 268, 889-893. doi: 10.1126/science.7754376.

Servos, P., Zacks, J., Rumelhart, D.E., Glover, G.H., 1998. Somatotopy of the human arm using fMRI. Neuroreport 9, 605-609. doi: 10.1097/00001756-199803090-00008.

Smith, S.M., Vidaurre, D., Beckmann, C.F., Glasser, M.F., Jenkinson, M., Miller, K.L., Nichols, T.E., Robinson, E.C., Salimi-Khorshidi, G., Woolrich, M.W., Barch, D.M., Uğurbil, K., Van Essen, D.C., 2013. Functional connectomics from resting-state fMRI. Trends Cogn. Sci. 17, 666-682. doi: 10.1016/j.tics.2013.09.016.

Tobimatsu, S., Zhang, Y.M., Kato, M., 1999. Steady-state vibration somatosensory evoked potentials: physiological characteristics and tuning function. Clin. Neurophysiol. 110, 1953-1958.

Tobimatsu, S., Zhang, Y.M., Suga, R., Kato, M., 2000. Differential temporal coding of the vibratory sense in the hand and foot in man. Clin. Neurophysiol. 111, 398-404.

Van Essen, D.C., Dierker, D.L., 2007. Surface-based and probabilistic atlases of primate cerebral cortex. Neuron 56, 209-225. doi:10.1016/j.neuron.2007.10.015.

Wall, M.B., Smith, A.T., 2008. The representation of egomotion in the human brain. Curr.

Biol. 18, 191-194. doi: 10.1016/j.cub.2007.12.053.

Zlatkina, V., Amiez, C., Petrides, M., 2016. The postcentral sulcal complex and the transverse postcentral sulcus and their relation to sensorimotor functional organization. Eur. J. Neurosci. 43, 1268-1283. doi: 10.1111/ejn.13049.

3 Unraveling the spatiotemporal brain dynamics during a reach-to-eat task

Ching-fu Chen[1], Kenneth Kreutz-Delgado[1,2], Martin I. Sereno[3,4], Ruey-Song Huang[2]*

[1]*Department of Electrical and Computer Engineering, University of California, San Diego, La Jolla, CA 92093, USA*

[2]*Institute for Neural Computation, University of California, San Diego, La Jolla, CA 92093, USA*

[3]*Department of Psychology and Neuroimaging Center, San Diego State University, San Diego, CA 92182, USA*

[4]*Experimental Psychology, University College London, London WC1H 0AP, UK*

*Address correspondence to:
Ruey-Song Huang
Institute for Neural Computation
University of California, San Diego
9500 Gilman Dr. #0559
La Jolla, CA 92093-0559
Phone/fax: (858) 822-5977
Email: rhuang@ucsd.edu

This chapter is under preparation for submitting to a peer-reviewed journal.

3.0 Abstract

Eating food with hands involves a sequence of action components, including orienting, reaching, grasping, and feeding. While the cortical representations of single action components have been mapped by human functional magnetic resonance imaging (fMRI) studies, little is known about the spatiotemporal dynamics among these representations during a continuous reach-to-eat task. In a phase-encoded fMRI experiment, subjects were scanned while they reached toward an image of food projected on a direct-view screen, grasped the 'virtual' food, and brought 'it' to their mouth within each periodic cycle. An initial Fourier-based analysis of fMRI time series revealed periodic signals and noise distributed across the cortical surface. Independent component analysis (ICA) was used to decompose each fMRI dataset into spatially independent components (ICs) containing periodic brain activations, periodic and aperiodic motion artifacts, and random noise. An ICA-pruned dataset was reconstructed following the rejection of ICs containing artifacts and noise. Time-frequency analysis was used to analyze and model the temporal characteristics of periodic signals and phases in each voxel. Circular statistics was then used to select voxels based on the spread of phase angles and estimate the mean phase angle of each voxel. By rendering and sorting the mean phase angles across the cortical surface, we show the real-time spatiotemporal brain

dynamics among the occipital, temporal, posterior parietal, primary sensorimotor, premotor, and supplementary motor cortices during a reach-to-eat task. While fMRI is generally known to have low temporal resolution, this study demonstrates that it is possible to resolve different activation latencies among brain regions during a reach-to-eat task.

Keywords: reaching, feeding, near-face space, time-resolved fMRI, phase-encoded design, periodic motion artifacts, independent component analysis, time-frequency analysis, circular statistics

3.1 Introduction

Eating food is one of the many daily activities that take place in the peripersonal space. A trivial task such as eating popcorn involves precise coordination among the sight, touch, movement, and proprioception. A typical reach-to-eat task comprises a sequence of action components: (1) orienting and attending to the food; (2) reaching toward the food; (3) grasping the food; and (4) transporting the food to the mouth (Flindall and Gonzalez, 2013; Foroud and Whishaw, 2012; Quinlan and Culham, 2015; Sacrey et al., 2012; Sveistrup et al., 2008). Over the last two decades, human neuroimaging studies have revealed several frontal and parietal regions that support different types of visually-guided actions, such as saccades, pointing, reaching, and grasping (see reviews in Culham and Valyear, 2006; Culham et al., 2006; Filimon, 2010; Grafton, 2010; Huang and Sereno, 2018; Sereno and Huang, 2014; Tunik et al., 2007; Vesia and Crawford, 2012). Furthermore, sensorimotor and multisensory representations of face, hands (fingers), and lips have been mapped in primary and association cortices using passive tactile and wide-field visual stimuli (e.g., see Carey et al., 2017; Chen et al., 2017; Huang and Sereno, 2007, 2018; Huang et al., 2012, 2017; Sereno and Huang, 2006). While the visual, tactile, motor, and action representations have been identified individually in functional magnetic resonance imaging (fMRI) studies, little is know about the

spatiotemporal dynamics among them during a continuous reach-to-eat task.

To map the cortical representations of action components and subcomponents in an fMRI experiment, previous studies have typically used randomized block designs – where each block consisted of the same action repeated multiple times (e.g., Filimon et al., 2007, 2009) – or event-related designs – where a single action or an action sequence constituted an event (Cavina-Pratesi et al., 2010, 2018; Gallivan et al., 2011, 2016; Rossit et al., 2013). Functional images have been analyzed using a general linear model (GLM) that computes the overall fit between the design matrix and the fMRI time series of each voxel (Ward, 2002). Brain regions specialized for a specific action component or sequence are then typically identified and differentiated from the others using a subtraction method (i.e., linear contrasts between conditions) and by comparing the magnitudes of peak hemodynamic responses within a time window following the event onset. However, the resulting 'static' map only shows distinct brain regions containing statistically significant activations without revealing the temporal sequence among them.

The methods just described do not take full advantage of the temporal resolution of standard fMRI, which at approximately one second, is good enough to begin to resolve differences in activation latency among brain regions underlying naturalistic cognitive, sensory, or motor processes (Ariani et al., 2018; Cunnington et al., 2005;

Formisano and Goebel, 2003; Formisano et al., 2002; Richter et al., 1997; Smolders et al., 2007; Sun et al., 2005; Weilke et al., 2001). In the present study, we used a phase-encoded design, also known as the traveling wave method, to investigate the spatio-temporal dynamics of brain activations during a reach-to-eat task in a periodic event-related fMRI experiment. The phase-encoded design was originally developed in order to make full use of the temporal precision of fMRI signals to map topological organization of visual, auditory, and somatosensory cortices in previous studies (Engel, 2012; Engel et al., 1994; Huang and Sereno, 2007; Sereno and Huang, 2006; Sereno et al., 1995; Talavage et al., 2004). It has also been used to map topological organization of the motor cortex by performing a sequence of movements (Carey et al., 2017; Sood and Sereno, 2016). In these studies, a Fourier transform is performed on the fMRI time series of each voxel. The power spectrum is used to measure activation significance, and then the phase angle at the stimulus or task frequency can be used to measure the temporal offset (i.e., delay) of significant periodic activations. The temporal sequence of activations among brain regions is then visualized by animating successive iso-phase contours (Sereno et al., 1995).

In this study, subjects reached toward an image of food projected on a direct-view screen, grasped the ‘virtual’ food, and brought ‘it’ to their mouth. These action

components took place at different time delays (phases) within each periodic cycle. A bite bar (for immobilizing the head) was not used because it would have blocked the hand-to-mouth movement. Consequently, fMRI time series contained periodic motion artifacts that were correlated with the periodic reach-to-eat movements. To resolve this confound, we used independent component analysis (ICA) to decompose fMRI data into spatially independent components (ICs) (McKeown et al., 1998a, 1998b, 2003). Each ICA-pruned fMRI dataset was reconstructed following the rejection of ICs containing periodic and aperiodic motion artifacts and random noise. We then used time-frequency analysis and circular statistics to model the temporal variability of periodic signals and phases of fMRI time series of each voxel (Chen et al., 2017). Voxels were selected based on the distribution of phases. By rendering and sorting the mean phase angles across the cortical surface, this study aims to unravel the real-time spatiotemporal brain dynamics in visual and sensorimotor cortices during a reach-to-eat task.

3.2 Materials and methods

3.2.1 Participants

Nine healthy right-hand dominant subjects (18-30 years; 3 males, 6 females) with normal or corrected-to-normal vision participated in this study. All subjects gave written informed consent according to protocols approved by the Human Research Protections Program of the University of California, San Diego (UCSD).

3.2.2 Experimental setup and stimuli

Each subject participated in a brief training session in a custom-built MRI simulator before an fMRI session. In both sessions, the subject lay supine with his/her head tilted forward inside a head coil, where the head was supported and constrained by foam padding. A back-projection screen was mounted ~15 cm in front of the subject's face, allowing the subject to directly view and touch the screen. Visual stimuli were programmed in the C language using the OpenGL Performer library (Huang et al., 2015), rendered at a resolution of 1024×768 pixels on a LCD projector (Dell 3300MP), and projected onto a region of ~35×26 cm (~98×82° field of view) (Fig. 3.1). Throughout the training and fMRI sessions, the subject fixated a central cross against a black background while attending to an image of snacks (size = ~28×28°; center = ~26° eccentrici-

ty) located in the lower right visual field. There were 16 periodic, evenly-spaced trials in each 256-s run. At the beginning (0 s) of each run, a new image appeared and signaled the onset of the first trial. The image stayed on the screen for 16 s and was then replaced by a different image randomly selected from six (Fig. 3.1), which signaled the onset of the second trial. Each subsequent image replacement signaled the onset of the next trial. Following the onset of each trial, the subject slowly reached toward the image, grasped the virtual snacks on the screen (with the thumb opposing the index, middle, and ring fingers), brought the virtual snacks into the mouth by touching both the upper and lower lips, and then rested the hand on the chest under the chin.

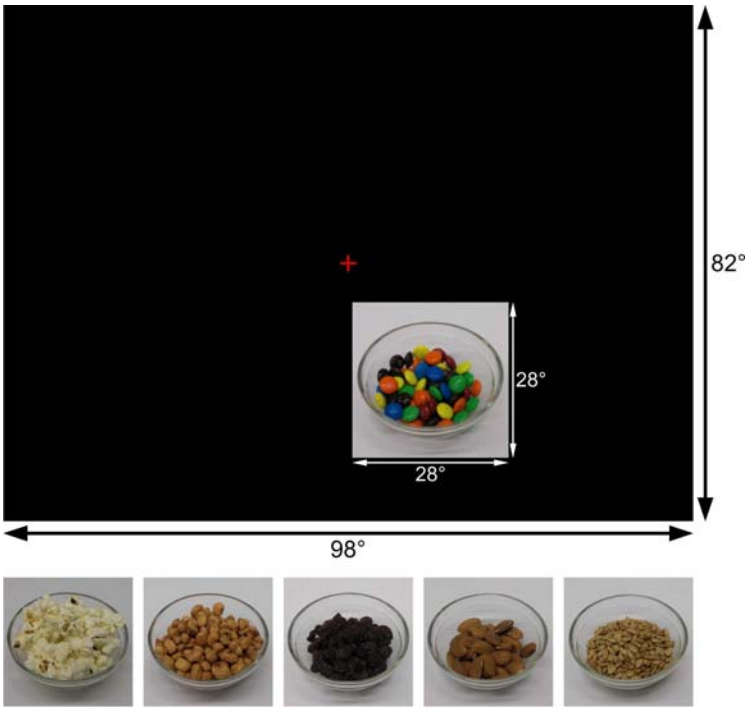

Fig. 3.1: Experimental design and stimuli. There were six images of different kinds of snacks. At the beginning of each 16-s cycle, a different image was randomly selected and shown in the lower right visual field for the entire cycle.

During the training session, the subject was informed that his/her task was similar to eating popcorn while watching a movie on a screen straight ahead, without directly looking at the popcorn in a container next to the lower face. In multiple 256-s runs, the subject practiced on keeping his/her head still while performing the sequence of reach-to-eat movements, which took 10-12 s across subjects. During the fMRI session, head movements were minimized by using foam padding.

3.2.3 Image acquisition and preprocessing

Subjects were scanned with an 8-channel head coil in a General Electric 3 T scanner at the Center for Functional MRI at UCSD. Two functional scans were acquired in each subject using a single-shot echo-planar imaging (EPI) sequence with the following parameters: bandwidth = 62.5 kHz; flip angle = 90°; TE = 30 ms; TR = 2000 ms; field of view = 200×200 mm; matrix = 64×64; voxel size = 3.125×3.125×3.5 mm; 31 axial contiguous slices; 128 TR per volume after discarding 8 dummy TRs. Two field map scans were then acquired with the same orientation and dimensions as the functional scans for correcting the geometrical distortion. Finally, an alignment scan was acquired using a fast spoiled gradient-echo (FSPGR) sequence at the same orientation as the functional images with the following parameters: field of view = 256×256 mm; matrix =

256×256; voxel size = 1×1×1.3 mm; 106 axial contiguous slices. In a different session, two additional sets of high-resolution structural images (FSPGR; field of view = 256×256 mm; matrix = 256×256; voxel size = 1×1×1 mm; 160-170 axial contiguous slices) were acquired for each subject.

The geometric distortion in the functional images was corrected using the field map scans and protocols provided by UCSD fMRI center (http://fmri.ucsd.edu/Howto/3T/fieldmap.html). Minor motion artifacts in the functional images were corrected using the *3dvolreg* tool of the Analysis of Functional NeuroImages (AFNI) software package (Cox, 1996). The cortical surfaces of each subject were reconstructed from averaging the high-resolution structural images using the FreeSurfer software package (Dale et al., 1999). Functional images were registered with the cortical surfaces by blink comparison between functional and structural images using an initial transformation matrix obtained by registering the alignment images to the high-resolution structural images.

3.2.4 Fourier-based analysis

To find task-related periodic brain activations, a 128-point discrete Fourier transform (DFT) is applied to the fMRI time series $x_m(t)$ of Voxel m by:

$$X_m(\omega) = \sum_{t=1}^{T} x_m(t)\exp(-j\omega t) = |X_m(\omega)|\exp[j\theta_m(\omega)], \quad (3.1)$$

where $X_m(\omega)$ is the complex component at frequency ω in the power spectra between 0-63 cycles per scan (cps), and $|X_m(\omega)|$ and $\theta_m(\omega)$ are the amplitude and phase angle respectively. The stimulus frequency is defined as ω_s (16 cps), and the remaining frequencies are defined as ω_n (52 bins between 0-63 cps; excluding 0-2, 15-17, 31-33, and 47-49 cps). The "signal" and "noise" are defined as the complex components $X_m(\omega)$ at ω_s and ω_n respectively. The ratio between the normalized signal energy and noise energy is obtained by (Dobie and Wilson, 1996):

$$F_m = \frac{|X_m(\omega_s)|^2 / dfs}{\left(\sum_{\omega_n} |X_m(\omega_n)|^2\right) / dfn}, \quad (3.2)$$

where $dfs = 2$ and $dfn = 104$ are the degrees of freedom of the signal and noise respectively. The *p*-value of F_m is estimated by the cumulative distribution function of the $F_{(2,104)}$ distribution. In the present study, voxels containing strong periodic signals ($\omega_s = 16$ cps) with $F_{(2,104)} > 4.82$ ($p < 0.01$, uncorrected) are retained and their phase angles $\theta_m(\omega_s)$ are color-coded on the cortical surface using FreeSurfer (Fig. 3.2).

3.2.5 Independent component analysis

Independent component analysis (ICA) is a statistical method for solving the blind source separation problem (Beckmann, 2012; Bell and Sejnowski, 1995; Calhoun and Adalı, 2006; Hyvärinen, 1999; McKeown et al, 1998b). Let $\mathbf{X} \in \Re^{P \times Q}$ be the matrix of the observed time series, which is the linear mixing of hidden (unknown) sources $\mathbf{C} \in \Re^{K \times Q}$. The rows of $\mathbf{C}$, $\mathbf{c}(1,:), \ldots, \mathbf{c}(K,:)$, are the independent sources (or independent components; ICs), which are independent non-Gaussian random variables. Hence,

$$\mathbf{X} = \mathbf{AC} = \sum_{k=1}^{K} \mathbf{a}_k \mathbf{c}(k,:), \tag{3.3}$$

where $\mathbf{A} = (\mathbf{a}_1, \ldots, \mathbf{a}_K) \in \Re^{P \times K}$ is the unknown mixing matrix with full column rank (i.e., $P \geq K$).

The objective of ICA is to find an unmixing matrix $\mathbf{W} \in \Re^{K \times P}$ such that $\hat{\mathbf{C}} = \mathbf{WX}$ is the best estimate of the hidden sources $\mathbf{C}$ by maximizing the non-Gaussianity or minimizing the mutual information between the sources using higher-order statistical moments. The unmixing matrix $\mathbf{W}$ is the pseudoinverse of $\mathbf{A}$, where $\mathbf{W} = \hat{\mathbf{A}}^{+}$. Hence, the sources $\mathbf{C}$ can be estimated by:

$$\hat{\mathbf{C}} = \mathbf{WX} = \hat{\mathbf{A}}^{+}\mathbf{X}. \tag{3.4}$$

The reconstructed signals can be represented as:

$$\hat{\mathbf{X}} = \hat{\mathbf{A}}\hat{\mathbf{C}} = \sum_{k=1}^{K} \hat{\mathbf{a}}_k \hat{\mathbf{c}}(k,:). \tag{3.5}$$

To reject artifact components ICs $l_1, \ldots, l_r$, their contributions to the observed signals can be removed by setting the $l_1^{th}, \ldots, l_r^{th}$ columns of $\hat{\mathbf{A}}$ to zero vectors, and a "clean" dataset is then reconstructed by:

$$\tilde{\mathbf{X}} = \sum_{\substack{k=1, \\ k \notin \{l_1, \ldots, l_r\}}}^{K} \hat{\mathbf{a}}_k \hat{\mathbf{c}}(k,:) = \hat{\mathbf{X}} - \sum_{\substack{l, \\ l \in \{l_1, \ldots, l_r\}}} \hat{\mathbf{a}}_l \hat{\mathbf{c}}(l,:). \tag{3.6}$$

ICA can be performed temporally or spatially on a dataset. In temporal ICA, each row of $\mathbf{X}$ is the observed time series, i.e., $\mathbf{X}$ is channel-by-time; whereas in spatial ICA, each column of $\mathbf{X}$ is the observed time series, i.e., $\mathbf{X}$ time-by-channel. For analyzing fMRI data, each 4-D (3-D volume by time) dataset is first reshaped into a 2-D matrix $\mathbf{X}$, where each column is the time series of a voxel and each row is obtained by reshaping each 3-D volume into a vector. Spatial ICA is then applied to decompose the matrix $\mathbf{X}$ into $\hat{\mathbf{X}} = \hat{\mathbf{A}}\hat{\mathbf{C}}$ (Eq. (3.5)), where each column of $\hat{\mathbf{A}}$ is the time series of an IC, and each rows in $\hat{\mathbf{C}}$ is the (spatial) component map (Beckmann, 2012; Calhoun and Adalı, 2006; Hyvärinen, 1999; McKeown et al, 1998b). Following artifact rejection, an ICA-pruned fMRI dataset is reconstructed using Eq. (3.6).

3.2.6 Time-frequency analysis

Time-frequency analysis can be applied to obtain the transition of the phase an-

gle in an fMRI dataset (Chen, 2017). For Voxel m, the fMRI time series $x_m(t)$ is multiplied by a moving window function $w(t-\tau)$ centered at time τ. The resulting time series is then subject to the discrete Fourier Transform:

$$X_m(\omega,\tau)=\sum_{t=1}^{T}\left[x_m(t)w(t-\tau)\right]\exp(-j\omega t)=\left|X_m(\omega,\tau)\right|\exp\left[j\theta_m(\omega,\tau)\right], \tag{3.7}$$

where the phase angle is defined as $\theta_m(\omega,\tau)$. The signal-to-noise ratio (SNR) at time τ can be obtained by:

$$F_m(\tau)=\left|S_m(\omega_s,\tau)\right|^2=\frac{\left|X_m(\omega_s,\tau)\right|^2/df_s}{\left(\sum_{\omega_n}\left|X_m(\omega_n,\tau)\right|^2\right)/df_n}, \tag{3.8}$$

and the complex component of SNR can be obtained by:

$$S_m(\omega_s,\tau)=\left|S_m(\omega_s,\tau)\right|\theta(\omega_s,\tau). \tag{3.9}$$

These procedures are repeated for all possible τ's to obtain a time series of the SNR, $S_m(\omega_s,t)$, and a time series of the phase angle, $\theta_m(\omega_s,t)$, at the stimulus frequency. For Voxel m in the ICA-pruned fMRI dataset $\tilde{\mathbf{X}}$, the time series of SNR, $\tilde{S}_m(\omega_s,t)$, and the time series of phase angle, $\tilde{\theta}_m(\omega_s,t)$, can be obtained using Eqs. (3.7)-(3.9).

3.2.7 Circular statistics

The distribution of an angular dataset, $\theta\in\{\theta_q\}_{q=1}^{Q}=\{\theta_1,\ldots,\theta_Q\}$ can be modeled using circular statistics. The angles are first converted into unit-length complex num-

bers, $z_q = \exp\left(j\theta_q\right)$. The first moment of the complex number is obtained by:

$$\mu_1 = \frac{1}{Q}\sum_{q=1}^{Q} z_q = \bar{r}_1 \exp\left(j\bar{\theta}\right), \tag{3.10}$$

where $\bar{r}_1$ is the mean resultant length, and $\bar{\theta}$ is the mean angle of this dataset (Fisher, 1993; Mardia and Jupp, 2000). Note that $0 \le \bar{r}_1 \le 1$.

To estimate the mean angle of a set of complex numbers with non-unit-length, $z \in \{z\}_{q=1}^{Q} = \{z_1, \ldots, z_Q\}$ with $z_q = r_q \exp\left(j\theta_q\right)$, the first sample moment can be obtained by (Chen et al, 2017; Grabska-Barwińska et al., 2012; Levick and Thibos, 1982; Ringach et al., 2002):

$$\mu_1 = \frac{\sum_{q=1}^{Q} z_q}{\sum_{q=1}^{Q} \left|z_q\right|} = \bar{r}_1 \exp\left(j\bar{\theta}\right), \tag{3.11}$$

where $\bar{\theta}$ and $\bar{r}_1$ are the mean angle and resultant length of the complex numbers.

The von Mises distribution is the circular analogy of the normal distribution (Fisher, 1993; Mardia and Jupp, 2000). The density function of the von Mises distribution, $VM\left(\phi,\kappa\right)$ is:

$$p\left(\Theta = \theta;\phi,\kappa\right) = \frac{1}{2\pi I_0\left(\kappa\right)} \exp\left[\kappa\cos\left(\theta - \phi\right)\right], \tag{3.12}$$

where ϕ is the mean angle, κ is the concentration parameter (analogous to $1/\sigma^2$ in the normal distribution), and $I_0\left(\kappa\right)$ is the modified Bessel function of order 0. If the angles in the dataset $\Theta = \{\theta_q\}_{q=1}^{Q} = \{\theta_1, \ldots, \theta_Q\}$ are independent samples from a $VM\left(\phi,\kappa\right)$ distri-

bution, ϕ can be estimated by using the mean angle of this dataset, $\overline{\theta}$, i.e., $\hat{\phi} = \overline{\theta}$. The concentration parameter κ can be estimated by using the mean resultant length, $\overline{r}_1$, i.e., $\hat{\kappa} = A(\overline{r}_1)$, where $A(\cdot)$ is a one-to-one mapping between $\overline{r}_1$ and $\hat{\kappa}$ (Fisher, 1993; Mardia and Jupp, 2000).

3.2.8 Modeling the spread of phase angle

Let Θ be a circular random variable and assume its mean angle and circular standard deviation are ϕ and ς respectively. The probability that Θ is in the interval between $\phi - \varsigma$ and $\phi + \varsigma$, $P(\phi - \varsigma \le \Theta \le \phi + \varsigma)$, depends on the values of ς (Fisher, 1993). However, it is possible to find a positive θ_c such that

$$P(\phi - \theta_c \le \Theta \le \phi + \theta_c) = q, \tag{3.13}$$

where q is a given probability value (Fisher, 1993). If the circular random variable Θ has the von Mises distribution, for a given q, θ_c can be calculated from the concentration parameter κ. For a fixed q, θ_c decreases as κ increases (Fisher, 1993; Mardia and Jupp, 2000).

Let $\Theta_1 = \{\tilde{\theta}_1(\omega_s, t)\}$ and $\Theta_2 = \{\tilde{\theta}_2(\omega_s, t)\}$, where $\tilde{\theta}_1(\omega_s, t)$ and $\tilde{\theta}_2(\omega_s, t)$ are the time series of phase angles of Voxels 1 and 2 of an ICA-pruned fMRI dataset. Assume the phase angles form two von Mises distributions $VM(\phi_1, \kappa_1)$ and $VM(\phi_2, \kappa_2)$ respec-

tively. If $\tilde{\theta}_{c,1} > \tilde{\theta}_{c,2} > 0$ and $P\left(\phi_1 - \tilde{\theta}_{c,1} \le \Theta_1 \le \phi_1 + \tilde{\theta}_{c,1}\right) = P\left(\phi_2 - \tilde{\theta}_{c,2} \le \Theta_2 \le \phi_2 + \tilde{\theta}_{c,2}\right)$, the phase angles in $\tilde{\theta}_1(\omega_s, t)$ are more disperse and the periodic signals in the corresponding SNR time series $\tilde{S}_1(\omega_s, t)$ are considered to be less stable (with higher phase jitter) (Chen, 2017).

3.2.9 Data processing pipeline

For each functional scan, an initial map of periodic activations was obtained by Fourier-based analysis (see Section 3.2.4), as demonstrated for a representative subject (Fig. 3.2). To remove artifacts and random noise, spatial ICA was applied to each of 18 fMRI datasets ($n = 9$) using the FastICA algorithm (Hyvärinen, 1999; Hyvärinen and Oja, 2000), which was implemented in the FSL (FMRIB Software Library) *MELODIC* (Multivariate Exploratory Linear Optimized Decomposition into Independent Components) toolbox (Beckmann and Smith, 2004). Each 4-D fMRI dataset of size 64×64×31×128 was reshaped into a matrix of size 128×126976, and then decomposed into an ICA dataset containing 30-54 spatial ICs across scans and subjects. For each ICA dataset, ICs were manually labeled based on their spatial activation maps and time courses (Figs. 3.3-3.6) (McKeown et al, 1998b). ICs containing strong periodic and aperiodic motion artifacts and random noise were removed from the ICA dataset, and a new

fMRI dataset was reconstructed in the original volume-time domain (Eq. (3.6)).

Following artifact rejection, the entire time series $\tilde{x}(t)$ of each voxel in the reconstructed fMRI dataset was subject to a 128-point discrete Fourier transform using Eq. (3.1), and the statistical significance of periodic signals at the stimulus frequency ($\omega_s = 16$ cps) was assessed using Eq. (3.2) (see Section 3.2.4). Voxels with $F_{(2,104)} > 4.82$ ($p < 0.01$, uncorrected) were retained and further subject to time-frequency analysis using a 32-point Chebyshev window (60 dB sidelobe attenuation; step size = 1 pt) in Eq. (3.7). For each voxel, a time series of the SNR, $\tilde{S}(\omega_s, t)$, and a time series of the phase angle, $\tilde{\theta}(\omega_s, t)$, at the stimulus frequency were then obtained using Eqs. (3.8)-(3.9) (see Section 3.2.6).

The phase angles in the time series $\tilde{\theta}(\omega_s, t)$ are assumed to be the von Mises distribution $VM(\hat{\phi}, \hat{\kappa})$, in which $\hat{\phi}$ is the mean angle of $\tilde{\theta}(\omega_s, t)$, and $\hat{\kappa}$ is estimated from the resultant length of $\tilde{\theta}(\omega_s, t)$ (see Section 3.2.7). The value of q in Eq. (3.13) was empirically set to 0.6827 (see Section 3.2.8). Voxels with $\theta_c \leq 30°$ (equivalent to $\kappa \geq 4$; Mardia and Jupp, 2000) were retained because they were considered to contain stable periodic activations (Fig. 3.7). For each voxel, the resulting mean phase angle $\hat{\phi}$ was painted on the surface using FreeSurfer (Fig. 3.8).

3.3 Results

The analyses and results are illustrated in detail for Scan 1 of Subject 1 as follows, and for the remaining datasets in the Supplementary Information.

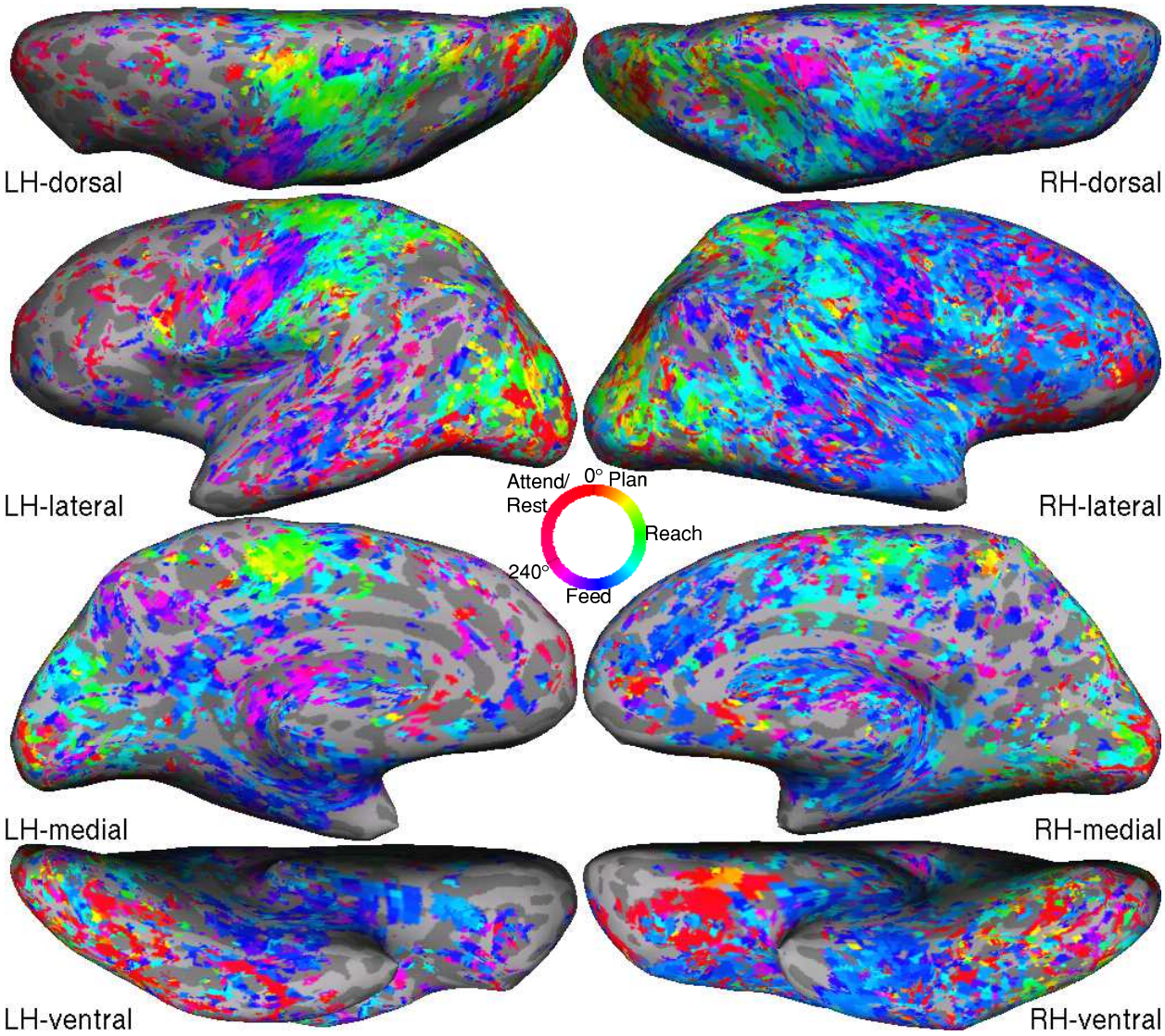

Fig. 3.2: Phase maps obtained by Fourier-based analysis. Different stages (phases) during the reach-to-eat task are color-coded as indicated by the color ring (full cycle = 16 s).

3.3.1 Fourier-based analysis

A liberal statistical threshold ($F_{(2,104)} > 4.82$, $p < 0.01$, uncorrected) was selected to show an initial activation map obtained by Fourier-based analysis (Fig. 3.2). This map show noisy activations distributed all over the cortical surface, especially in the right hemisphere. Some of the strong periodic activations at the orbital frontal lobe and anterior temporal lobe could be motion artifacts not corrected by volume registration (AFNI *3dvolreg*). These artifacts are still present even at a high statistical threshold. To reject these artifacts, the dataset was then subject to independent component analysis and circular statistical analysis, and the results are shown as follows.

3.3.2 Independent component analysis

Independent component analysis of an fMRI dataset revealed ICs containing task-related brain periodic activation, periodic and aperiodic motion artifacts, and random noise. Task-related ICs are identified and retained based on strong periodic activations within the brain region in 2-D images (Fig. 3.3). For example, surface-based maps of IC-10 show periodic activations in the primary sensorimotor cortex, premotor cortex, supplementary motor cortex, V6/V6A, and MT+, predominantly in the left hemisphere (Fig. 3.4).

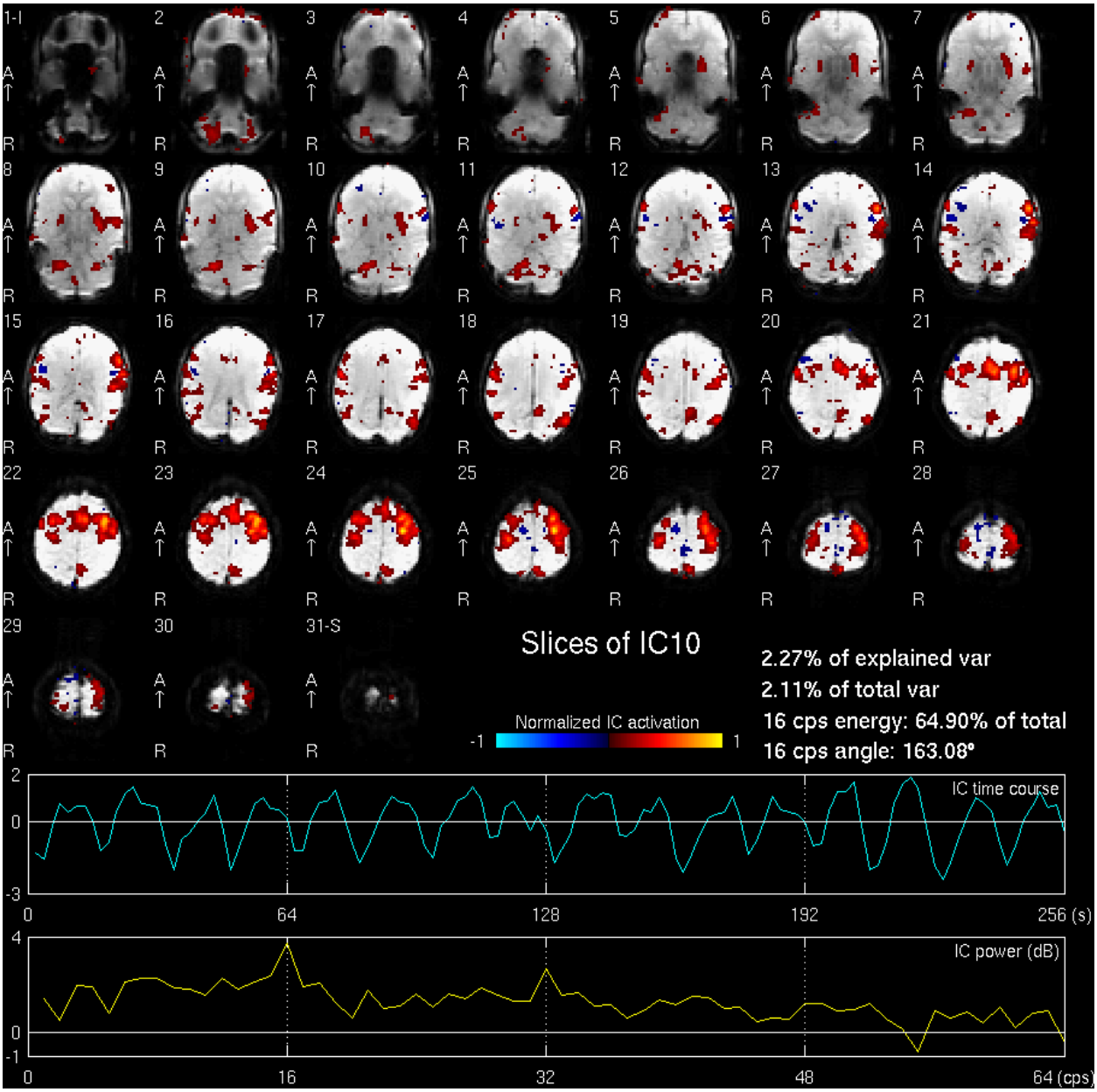

Fig. 3.3: An example of a brain-activation component (IC-10). Upper panels: 31 slices of functional images overlaid with normalized IC activations, as color-coded by the color bar. Lower panels: time course (cyan) and power spectrum (yellow) of IC-10. The IC time course exhibits strong periodic activation, as indicated by the peak at 16 cps in the power spectrum.

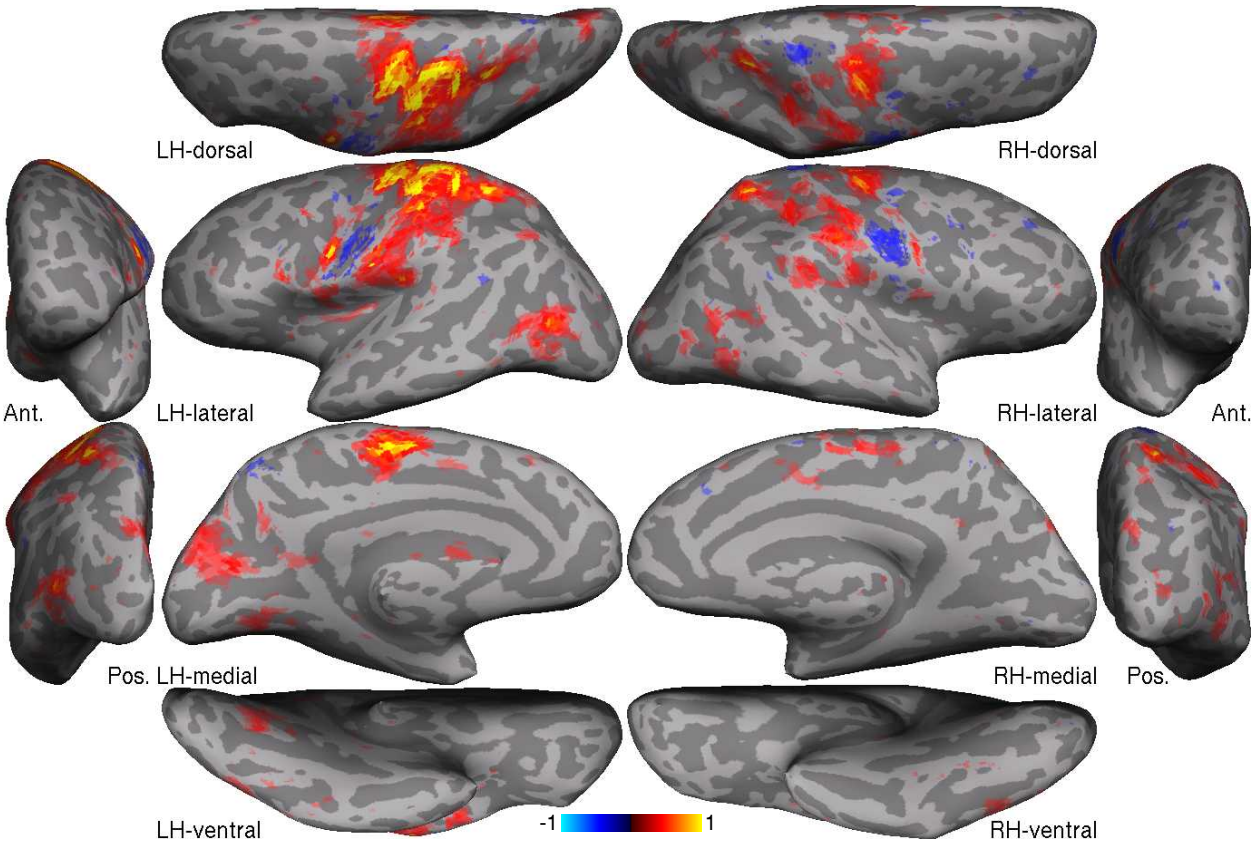

Fig. 3.4: Surface-based activation maps of IC-10. Normalized IC activations are color-coded by the color bar.

Artifact ICs are identified and rejected based on their spatial activation maps and time courses. For example, IC-1 that contains strong periodic activations at the right anterior and left posterior edges of the brain is considered to be motion artifacts (Fig. 3.5). Surface-based activation maps of IC-1 show activations located at the lateral anterior frontal cortex, orbital frontal cortex, and anterior temporal cortex (Fig. 3.6). These activations are likely to result from periodic head movements during the reach-to-eat task. Other ICs containing aperiodic motion artifacts at brain edges or random noise scattered within the brain were also identified. In total, 36 ICs containing artifacts or noise

were rejected to reconstruct a new dataset using Eq. (3.6).

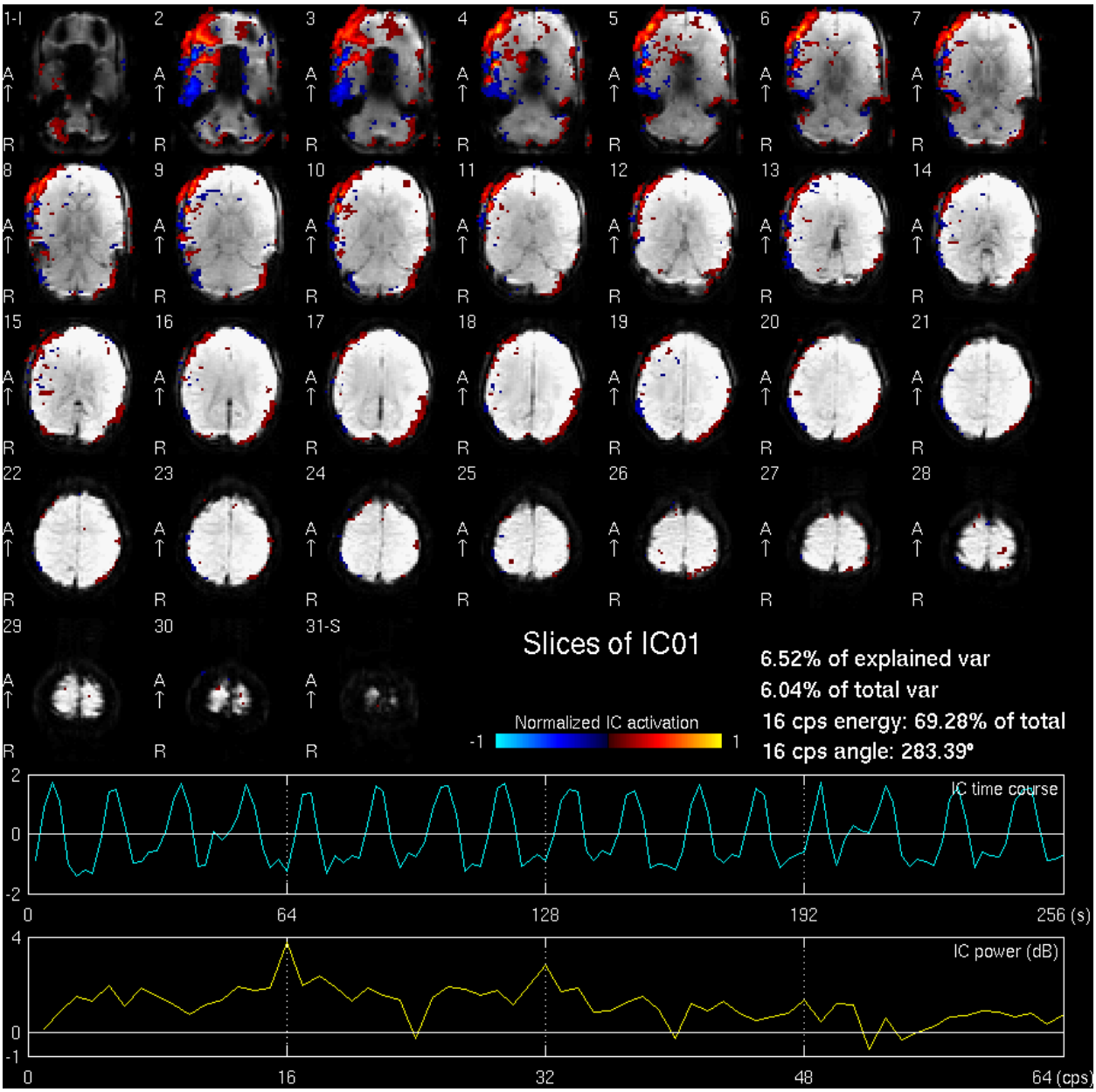

Fig. 3.5: An example of an artifact component (IC-1). All conventions follow Fig. 3.3. The time course of IC-1 also exhibits strong periodic activation, as indicated by the peak at 16 cps in the power spectrum.

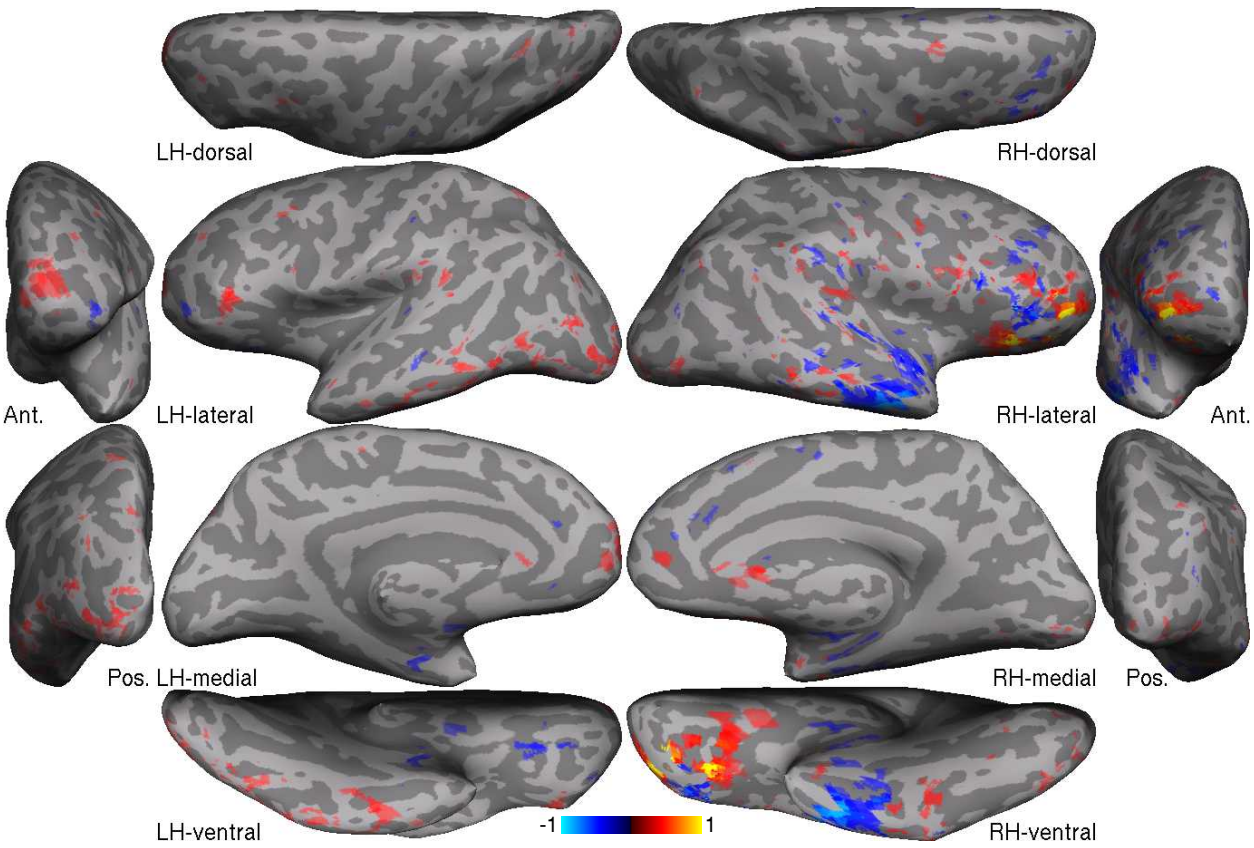

Fig. 3.6: Surface-based activation maps of IC-1. All conventions follow Fig. 3.4.

3.3.3 Circular statistics

Time-frequency and circular statistical analyses were applied to the ICA-pruned dataset (Sections 3.2.6 and 3.2.7). Voxels with $\theta_c \leq 30°$ and with $q = 0.6827$ in Eq. (3.13) were retained (Sections 3.2.8). The spread of phase angles of each retained voxel is displayed on the cortical surface (Fig. 3.7), where the yellow and red regions are considered to contain stable periodic signals (low phase jitter) activated by the reach-to-eat task. These regions include the premotor cortex, primary sensorimotor cor-

tex, secondary somatosensory cortex, supplementary motor area, middle temporal regions, areas V6/V6A, far peripheral portion of V1-V3, and ventral occipital cortex. Lastly, the estimated mean phase angle $\hat{\phi}$ of each retained voxel was painted on the cortical surface (Fig. 3.8).

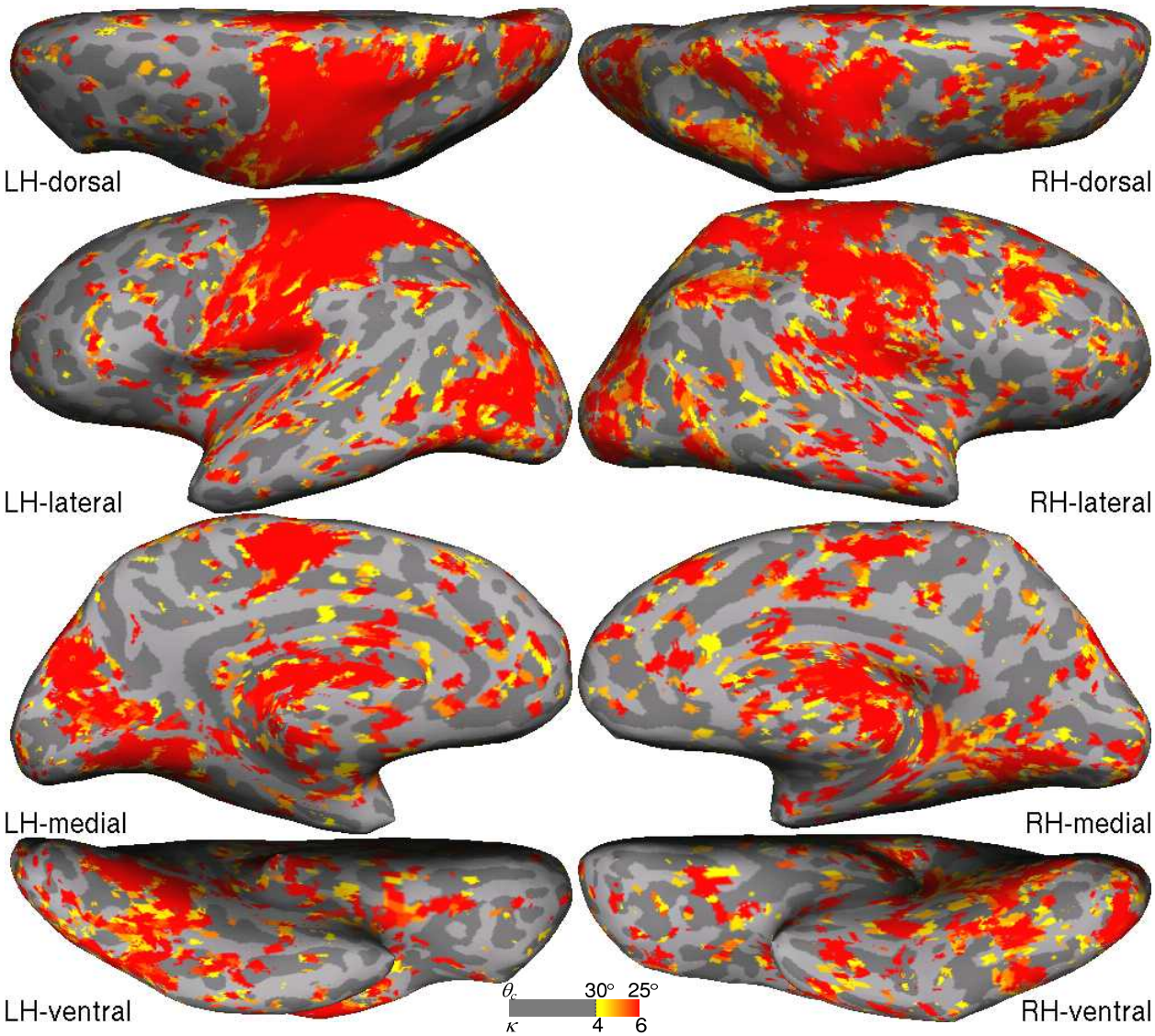

Fig. 3.7: Surface-based maps of the spread of phase angles. Voxels with $\theta_c \leq 30°$ (θ_c in Eq. (3.13) with $q = 0.6827$) are retained and rendered on the cortical surface.

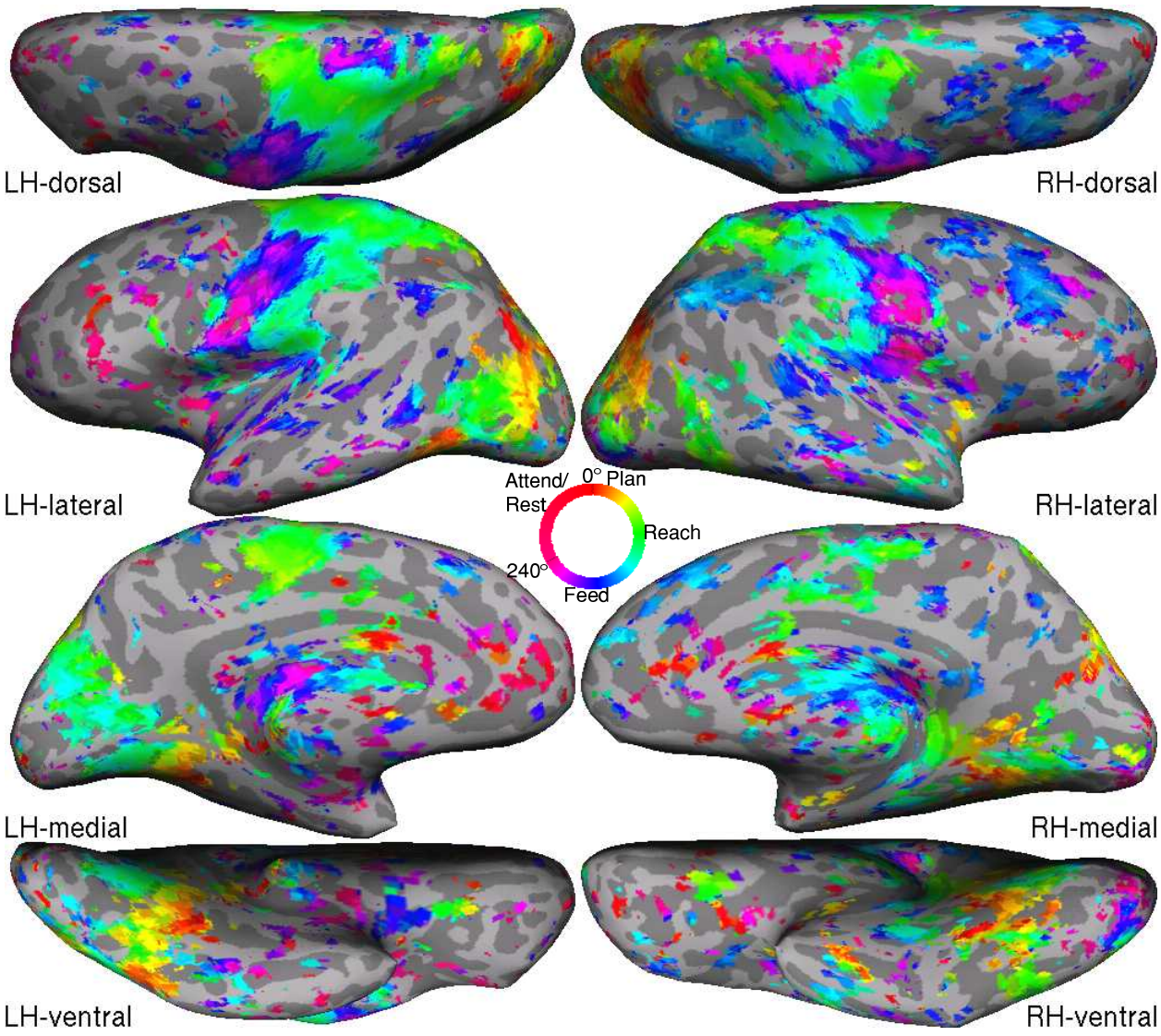

Fig. 3.8: Surface-based maps of estimated mean phase angle. All conventions including the color ring follow Fig. 3.2. During each cycle of the reach-to-eat task, brain activations begin in visual areas (red/yellow regions), advance into area MT+ and parietal arm/hand representations (green), and finally enter the face and lip representations in primary sensorimotor cortex (blue/magenta).

3.4 Discussion

The reach-to-eat task is routine yet essential for everyone at all ages in daily life (Flindall and Gonzalez, 2013; Foroud and Whishaw, 2012; Quinlan and Culham, 2015; Sacrey et al., 2012; Sveistrup et al., 2008). Some populations with neurological disorders or brain injuries exhibit impaired movements while eating (Doan et al., 2008; Foroud and Whishaw, 2010; Hung et al., 2012). Due to technical constraints and limited space in the MRI scanner, few fMRI studies have attempted to map the neural substrates of the reach-to-eat task in healthy or clinical populations. In the current study, we demonstrated the experimental design and setup for investigating the spatiotemporal brain dynamics during a continuous reach-to-eat task in healthy adults. Head motion artifacts in functional images are a major concern for sensorimotor fMRI experiments in all populations. A number of preventive measures have been attempted to minimize head movements. First, subjects can be trained to remain completely still while performing motor tasks within a mock MRI scanner before they participate in the real fMRI experiment. Second, head movements can be reduced by bracing the shoulder and upper arm while allowing restricted forearm movements away from the head (Cavina-Pratesi et al., 2010, 2018; Gallivan et al., 2011, 2016; Rossit et al., 2013). Third, the head can be immobilized using foam pads, thermoplastic sheets, and/or a bite bar with individual

dental impression (Chen et al., 2017; Filimon et al., 2007, 2009; Huang et al., 2012, 2017).

In the present study, we recruited experienced subjects who had previously participated in multiple fMRI experiments and been trained to stay motionless during the scan. We used sufficient foam padding to stabilize the head during experimental setup. To clear the pathway for hand-to-mouth movements, we did not use thermoplastic sheets or bite bars. Across subjects, the time series of six motion parameters (output of AFNI *3dvolreg*) showed minor periodic displacement in the superior-inferior (S/I) and anterior-posterior (A/P) directions, which were temporally correlated with the reach-to-eat movement. There was little to no displacement in the left-right (L/R) direction, suggesting the head was well stabilized laterally by the foam padding. Minor head movements in the S/I and A/P directions were unavoidable because eating food in a natural setting involves the coordination among the head, trunk, arm, and hand (Foroud and Whishaw, 2012; Hung et al., 2012; Sveistrup et al., 2008; van der Kamp and Steenbergen, 1999). While the subject was instructed to keep the head still, it was not possible to completely prevent the head from involuntary leaning forward to align the mouth with the incoming food. Although not preferable, allowing minor but correctable motion artifacts would make it possible to investigate the neural mechanism of head advancement

toward the food during a realistic reach-to-eat task. Furthermore, the task-correlated motion artifacts also provide additional information for data analysis (see discussion immediately below).

Here, we corrected motion artifacts in two stages: (1) volume registration by rigid body transformation (AFNI *3dvolreg*), and (2) independent component analysis (ICA) using the FastICA algorithm (Hyvärinen, 1999; Hyvärinen and Oja, 2000). Volume registration yielded the time series of estimated head movements in six degrees of freedom, which revealed not only the linear trends but also periodic fluctuations of head movements. Across subjects, these time series showed gradual linear drifts without abrupt motion, suggesting that all subjects were able to remain immobile during the experiment. However, volume registration (AFNI *3dvolreg*) was unable to correct and remove periodic motion artifacts correlated with the reach-to-eat movement. Subsequently, independent component analysis of the volume-registered fMRI dataset revealed components with task-related periodic brain activations, components with periodic and aperiodic motion artifacts, and components with scattered random noise. Periodic motion artifacts usually occurred at the edge between the brain and non-brain regions, as shown in axial slices (Fig. 3.5). These types of artifacts were likely to result from minor head displacement in the posterior-anterior direction and head pitch movement while the

hand approached the mouth (as discussed above). For ICs containing task-related periodic activations distributed across different brain regions, future studies will be needed to analyze and interpret the spatiotemporal patterns of each IC in detail. In the present study, we have only removed ICs containing artifacts and noise and reconstructed a single ICA-pruned dataset in with the original dimensions.

Previous event-related fMRI studies have used GLM-based designs and analyses to map brain regions that are involved in visually-guided actions, such as reaching, grasping, and pointing (e.g., Cavina-Pratesi et al., 2010, 2018; Gallivan et al., 2011, 2016; Rossit et al., 2013). The typical duration of each action event is about 2-4 s. Event-related activation in a brain region can be characterized by a hemodynamic response function (HRF), which revels when the activation rises, peaks, falls, undershoots, and returns to the baseline. However, conventional methods using a time-fixed model typically compare the peak magnitude rather than the latency of HRF across different conditions (actions) and brain regions. While time-resolved fMRI studies have used time-shifted models to reveal different activation latencies across brain regions (Formisano et al., 2002; Liao et al., 2002; Weilke et al., 2001), the time delays used in these models are limited to the multiples of a fixed TR (e.g., 2 s, 4 s, 6 s, 8 s and so on in the current study).

In the present study, we used a phase-encoded design and Fourier-based analysis to resolve the sequential activations among brain regions during a continuous reach-to-eat task. Fourier transform of fMRI time series reveals the phase angle (or delay) of periodic activations at 16 cycles per scan (16 s per cycle). Although the 16-s period was shorter than typically used in a phase-encoded mapping experiment (e.g., 32 s or 64 s), the resulting phase angles were continuously distributed around the full cycle (0 to 2π). Furthermore, the 16-s period is sufficient for the subject to slowly perform a natural, self-paced, and continuous reach-to-eat task, following a single cue of action onset (a different image of snacks). While it is possible to present an explicit visual or auditory cue for each action component (attention, reaching, grasping, and feeding), it is unnatural to perform a discontinuous reach-to-eat task with frequent pauses in a longer period (e.g., 30 s). On the other hand, one of the disadvantages of a continuous self-paced task is that the timing of movements could vary slightly from trial to trial. In the present study, we were unable to record the subject's hand and head movements behind the direct-view screen. However, we showed that it is possible to analyze the timing and regularity of task-correlated head movements using the time series of motion parameters generated by the AFNI *3dvolreg* tool. Across scans and subjects, the time series of A/P head displacement exhibited strong periodic signals at the task frequency (16 cps), which

suggested that the timing of movements was consistent across trials within each scan.

Because fMRI has low temporal resolution and limited samples, conventional linear methods typically estimate the overall fit between the design matrix and the entire time series of each voxel. In our previous and present studies, we demonstrated that time-frequency analysis can be used to reveal the temporal characteristics of periodic fMRI signals (Chen et al., 2017). Circular statistics was then used to evaluate the stability of periodic signals by modeling the spread of phase angles and estimate the mean phase angles of each voxel. The resulting phase map shows periodic activations distributed across the occipital, middle temporal, posterior parietal, primary and secondary somatosensory, primary motor, premotor, and supplementary motor cortices (Fig. 3.8). The overall extent of these activations is consistent with the regions activated by executed reaching combined with the regions activated by passive stimulation to the hands, face, and lips in previous studies (Filimon et al., 2007, 2009; Huang and Sereno, 2007, 2018; Huang et al., 2012). While previous studies have only shown static statistical maps of these sensorimotor representations, the current study further revealed the spatiotemporal dynamics within the extent of significant activations. The temporal order of activations among brain regions was consistent with the action sequence of the reach-to-eat task, which consists of the following stages: (1) attending to and detecting a dif-

ferent image activated scene selective areas including PPA and OPA (reddish regions); (2) planning and executing reaching toward the image activated parts of the premotor cortex, supplementary motor area, superior parietal cortex, and lateral occipital cortex (yellowish to greenish regions); (3) grasping activated areas peripheral V1-V3, V6/V6A, SMA, MT+, LIP+, VIP+, SI/MI, AIP, face and hand SI/SII (greenish regions); and (4) feeding activated face and lip representations in the primary sensorimotor cortex (bluish to pinkish). These activation patterns are best illustrated using a surface-based movie of iso-phase contours (Sereno and Huang, 2006), in an approach similar to tracking the progression of rainfall over time and space on Doppler weather radar maps. Although fMRI signals were acquired with 8 TRs in each 16-s cycle in the present study, the resulting phase movie suggested that it is possible to estimate activation phase angles at a higher resolution (7.5 frames/s or 15 frames/TR; 120 angles/cycle). For example, a traveling wave of activation was observed along the superior to inferior parts of the left postcentral gyrus between 2-4 s (within one TR).

3.5 Acknowledgments

This work was supported by the National Institutes of Health (R01 MH081990 to M.I.S. and R.-S.H.), Royal Society Wolfson Research Merit Award and Wellcome Trust

to M.I.S., and UC San Diego Frontiers of Innovation Scholars Program (FISP) Project Fellowships to C.-f.C.

The materials in chapter are preparing for submission: Chen, C.F., Kreutz-Delgado, K., Sereno, M.I., Huang, R.S.: Unraveling the spatiotemporal brain dynamics during a reach-to-eat task. In this research, I conducted the experiments and analyzed the data. I also refined the circular statistics we used in our previous research. I want to thank Doctor Ruey-Song Huang for the guidance of the direction of the research and Professor Kenneth Kreutz-Delgado for making mathematical statements more rigorous. Also thank Professor Marty Sereno for FreeSurfer support and comments on the manuscript.

3.6 References

Ariani, G., Oosterhof, N.N., Lingnau, A., 2018. Time-resolved decoding of planned delayed and immediate prehension movements. Cortex 99, 330-345.

Beckmann, C.F., 2012. Modelling with independent components. NeuroImage 62, 891-901.

Beckmann, C.F., Smith, S.M., 2004. Probabilistic independent component analysis for functional magnetic resonance imaging. IEEE Trans. Med. Imaging 23, 137-152.

Bell, A.J., Sejnowski, T.J., 1995. An information-maximization approach to blind separation and blind deconvolution. Neural Comput. 7, 1129-1159.

Calhoun, V.D., Adalı, T., 2006. Unmixing fMRI with independent component analysis. IEEE. Eng. Med. Biol. Mag. 25, 79-90.

Carey, D., Krishnan, S., Callaghan, M.F., Sereno, M.I., Dick, F., 2017. Functional and quantitative MRI mapping of somatomotor representations of human supralaryngeal vocal tract. Cereb. Cortex 27, 265-278.

Cavanna, A.E., Trimble, M.R., 2006. The precuneus: a review of its functional anatomy and behavioural correlates. Brain 129, 564-583.

Cavina-Pratesi, C., Monaco, S., Fattori, P., Galletti, C., McAdam, T.D., Quinlan, D.J., Goodale, M.A., Culham, J.C., 2010. Functional magnetic resonance imaging reveals the neural substrates of arm transport and grip formation in reach-to-grasp actions in humans. J. Neurosci. 30, 10306-10323.

Cavina-Pratesi, C., Connolly, J.D., Monaco, S., Figley, T.D., Milner, A.D., Schenk, T., Culham, J.C., 2018. Human neuroimaging reveals the subcomponents of grasping, reaching and pointing actions. Cortex. 98, 128-148.

Chen, C.F., Kreutz-Delgado, K., Sereno, M.I., Huang, R.S., 2017. Validation of periodic fMRI signals in response to wearable tactile stimulation. NeuroImage 150, 99-111.

Cox, R.W., 1996. AFNI: software for analysis and visualization of functional magnetic resonance neuroimages. Comput. Biomed. Res. 29, 162-173.

Culham, J.C., Cavina-Pratesi, C., Singhal, A., 2006. The role of parietal cortex in visuomotor control: what have we learned from neuroimaging? Neuropsychologia 44, 2668-2684.

Culham, J.C., Valyear, K.F., 2006. Human parietal cortex in action. Curr. Opin. Neurobiol. 16, 205-212.

Cunningham, D.A., Machado, A., Yue, G.H., Carey, J.R., Plow, E.B., 2013. Functional somatotopy revealed across multiple cortical regions using a model of complex motor task. Brain Res. 1531, 25-36.

Cunnington, R., Windischberger, C., Moser, E., 2005. Premovement activity of the pre-supplementary motor area and the readiness for action: studies of time-resolved event-related functional MRI. Hum. Mov. Sci. 24, 644-656.

Dale, A.M., Fischl, B., Sereno, M.I., 1999. Cortical surface-based analysis. I. Segmentation and surface reconstruction. NeuroImage 9, 179-194.

Doan, J.B., Melvin, K.G., Whishaw, I.Q., Suchowersky, O., 2008. Bilateral impairments of skilled reach-to-eat in early Parkinson's disease patients presenting with unilateral or asymmetrical symptoms. Behav. Brain Res. 194, 207-213.

Dobie, R.A., Wilson, M.J., 1996. A comparison of t test, F test, and coherence methods of detecting steady-state auditory-evoked potentials, distortion-product otoacoustic emissions, or other sinusoids. J. Acoust. Soc. Am. 100, 2236-2246.

Engel, S.A., 2012. The development and use of phase-encoded functional MRI designs. NeuroImage 62, 1195-1200.

Engel, S.A., Rumelhart, D.E., Wandell, B.A., Lee, A.T., Glover, G.H., Chichilnisky, E.J., Shadlen, M.N., 1994. fMRI of human visual cortex. Nature 369, 525.

Filimon, F., 2010. Human cortical control of hand movements: parietofrontal networks

for reaching, grasping, and pointing. Neuroscientist 16, 388-407.

Filimon, F., Nelson, J.D., Hagler, D.J., Sereno, M.I., 2007. Human cortical representations for reaching: mirror neurons for execution, observation, and imagery. NeuroImage 37, 1315-1328.

Filimon, F., Nelson, J.D., Huang, R.S., Sereno, M.I., 2009. Multiple parietal reach regions in humans: cortical representations for visual and proprioceptive feedback during on-line reaching. J. Neurosci. 29, 2961-2971.

Fischl, B., Sereno, M.I., Tootell, R.B., Dale, A.M., 1999. High-resolution intersubject averaging and a coordinate system for the cortical surface. Hum. Brain Mapp. 8, 272-284.

Fisher, N.I., 1993. Statistical Analysis of Circular Data, first ed. Cambridge University Press, Cambridge.

Flindall, J.W., Gonzalez, C.L., 2013. On the evolution of handedness: evidence for feeding biases. PLoS One 8:e78967.

Formisano, E., Goebel, R., 2003. Tracking cognitive processes with functional MRI mental chronometry. Curr. Opin. Neurobiol. 13, 174-181.

Formisano, E., Linden, D.E., Di Salle, F., Trojano, L., Esposito, F., Sack, A.T., Grossi, D., Zanella, F.E., Goebel, R., 2002. Tracking the mind's image in the brain I: time-resolved fMRI during visuospatial mental imagery. Neuron 35, 185-194.

Foroud, A., Whishaw, I.Q., 2010. Reaching-to-eat in humans post-stroke: fluctuating components within a constant pattern. Behav. Neurosci. 124, 851-867.

Foroud, A., Whishaw, I.Q., 2012. The consummatory origins of visually guided reaching in human infants: a dynamic integration of whole-body and upper-limb movements. Behav. Brain Res. 231, 343-355.

Gallivan, J.P., Johnsrude, I.S., Flanagan, J.R., 2016. Planning ahead: Object-directed sequential actions decoded from human frontoparietal and occipitotemporal net-

works. Cereb. Cortex 26, 708-730.

Gallivan, J.P., McLean, D.A., Smith, F.W., Culham, J.C., 2011. Decoding effector-dependent and effector-independent movement intentions from human parieto-frontal brain activity. J. Neurosci. 31, 17149-17168.

Grafton, S.T., 2010. The cognitive neuroscience of prehension: recent developments. Exp. Brain Res. 204, 475-491.

Grabska-Barwińska, A., Ng, B.S., Jancke, D., 2012. Orientation selective or not? – Measuring significance of tuning to a circular parameter. J. Neurosci. Methods 203, 1-9.

Huang, R.S., Chen, C.F., Sereno, M.I., 2015. Neural substrates underlying the passive observation and active control of translational egomotion. J. Neurosci. 35, 4258-4267.

Huang, R.S., Chen, C.F., Sereno, M.I., 2017. Mapping the complex topological organization of the human parietal face area. Neuroimage.Huang, R.S., Chen, C.F., Tran, A.T., Holstein, K.L., Sereno, M.I., 2012. Mapping multisensory parietal face and body areas in humans. Proc. Natl. Acad. Sci. USA 109, 18114-18119.

Huang, R.S., Sereno, M.I., 2007. Dodecapus: An MR-compatible system for somatosensory stimulation. NeuroImage 34, 1060-1073.

Huang, R.S., Sereno, M.I., 2018. Multisensory and Sensorimotor Maps. in: G.Vallar, H.B.Coslett (eds.), The Parietal Lobe. Neurological and Neuropsychological Deficits (Handbook of Clinical Neurology). Elsevier, Amsterdam, Netherlands Netherlands. pp. 141-161.

Hung, Y.C., Henderson, E.R., Akbasheva, F., Valte, L., Ke, W.S., Gordon, A.M., 2012. Planning and coordination of a reach-grasp-eat task in children with hemiplegia. Res. Dev. Disabil. 33, 1649-1657.

Hyvärinen, A., 1999. Fast and robust fixed-point algorithms for independent component analysis. IEEE Trans. Neural. Netw. 10, 626-634.

Hyvärinen, A., Oja, E., 2000. Independent component analysis: algorithms and applications. Neural Netw. 13, 411-430.

Levick, W.R., Thibos, L.N., 1982. Analysis of orientation bias in cat retina. J. Physiol. 329, 243-261.

Liao, C.H., Worsley, K.J., Poline, J.B., Aston, J.A., Duncan, G.H., Evans, A.C., 2002. Estimating the delay of the fMRI response. NeuroImage 16, 593-606.

Mardia, K.V., Jupp, P.E., 2000. Directional Statistics. John Wiley & Sons, Hoboken, New Jersey, USA.

McKeown, M.J., Hansen, L.K., Sejnowsk, T.J., 2003. Independent component analysis of functional MRI: what is signal and what is noise? Curr. Opin. Neurobiol. 13, 620-629.

McKeown, M.J., Jung, T.P., Makeig, S., Brown, G., Kindermann, S.S., Lee, T.W., Sejnowski, T.J., 1998a. Spatially independent activity patterns in functional MRI data during the stroop color-naming task. Proc. Natl. Acad. Sci. USA 95, 803-810.

McKeown, M.J., Makeig, S., Brown, G.G., Jung, T.P., Kindermann, S.S., Bell, A.J., Sejnowski, T.J., 1998b. Analysis of fMRI data by blind separation into independent spatial components. Hum. Brain Mapp. 6, 160-188.

Quinlan, D.J., Culham, J.C., 2015. Direct comparisons of hand and mouth kinematics during grasping, feeding and fork-feeding actions. Front Hum. Neurosci. 9, 580.

Richter, W., Andersen, P.M., Georgopoulos, A.P., Kim, S.G., 1997. Sequential activity in human motor areas during a delayed cued finger movement task studied by time-resolved fMRI. Neuroreport 8, 1257-1261.

Ringach D.L., Shapley R.M., Hawken M.J., 2002. Orientation selectivity in macaque V1: diversity and laminar dependence. J. Neurosci. 22, 5639-5651.

Rossit, S., McAdam, T., McLean, D.A., Goodale, M.A., Culham, J.C., 2013. fMRI reveals a lower visual field preference for hand actions in human superior parieto-

occipital cortex (SPOC) and precuneus. Cortex 49, 2525-2541.

Sacrey, L.A., Karl, J.M., Whishaw, I.Q., 2012. Development of visual and somatosensory attention of the reach-to-eat movement in human infants aged 6 to 12 months. Exp. Brain Res. 223, 121-136.

Sereno, M.I., Dale, A.M., Reppas, J.B., Kwong, K.K., Belliveau, J.W., Brady, T.J., Rosen, B.R., Tootell, R.B., 1995. Borders of multiple visual areas in humans revealed by functional magnetic resonance imaging. Science 268, 889-893.

Sereno, M.I., Huang, R.S., 2006. A human parietal face area contains aligned head-centered visual and tactile maps. Nat. Neurosci. 9, 1337-1343.

Sereno, M.I., Huang, R.S., 2014. Multisensory maps in parietal cortex. Curr. Opin. Neurobiol. 24, 39-46.

Smolders, A., De Martino, F., Staeren, N., Scheunders, P., Sijbers, J., Goebel, R., Formisano, E., 2007. Dissecting cognitive stages with time-resolved fMRI data: a comparison of fuzzy clustering and independent component analysis. Magn. Reson. Imaging 25, 860-868.

Sood, M.R., Sereno, M.I., 2016. Areas activated during naturalistic reading comprehension overlap topological visual, auditory, and somatotomotor maps. Hum. Brain Mapp. 37, 2784-2810.

Sun, F.T., Miller, L.M., D'Esposito, M., 2005. Measuring temporal dynamics of functional networks using phase spectrum of fMRI data. NeuroImage 28, 227-237.

Sveistrup, H., Schneiberg, S., McKinley, P.A., McFadyen, B.J., Levin, M.F., 2008. Head, arm and trunk coordination during reaching in children. Exp. Brain Res. 188, 237-247.

Talavage, T.M., Sereno, M.I., Melcher, J.R., Ledden, P.J., Rosen, B.R., Dale, A.M., 2004. Tonotopic organization in human auditory cortex revealed by progressions of frequency sensitivity. J. Neurophysiol. 91, 1282-1296.

Tunik, E., Rice, N.J., Hamilton, A., Grafton, S.T., 2007. Beyond grasping: representation of action in human anterior intraparietal sulcus. NeuroImage 36 Suppl. 2, T77-86.

van der Kamp, J., Steenbergen, B., 1999. The kinematics of eating with a spoon: bringing the food to the mouth, or the mouth to the food? Exp. Brain Re.s 129, 68-76.

Vesia, M., Crawford, J.D., 2012. Specialization of reach function in human posterior parietal cortex. Exp. Brain Res. 221, 1-18.

Virji-Babul, N., Moiseev, A., Cheung, T., Weeks, D., Cheyne, D., Ribary, U., 2010. Spatial-temporal dynamics of cortical activity underlying reaching and grasping. Hum. Brain Mapp. 31, 160-171.

Ward, B.D., 2002. Deconvolution analysis of fMRI time series data. AFNI 3dDeconvolve documentation. Medical College of Wisconsin, Milwaukee, WI, USA.

Wasson, P., Prodoehl, J., Coombes, S.A., Corcos, D.M., Vaillancourt, D.E., 2010. Predicting grip force amplitude involves circuits in the anterior basal ganglia. NeuroImage 49, 3230-3238.

Weilke, F., Spiegel, S., Boecker, H., von Einsiedel, H.G., Conrad, B., Schwaiger, M., Erhard, P., 2001. Time-resolved fMRI of activation patterns in M1 and SMA during complex voluntary movement. J Neurophysiol 85, 1858-1863.

Zlatkina, V., Amiez, C., Petrides, M., 2016. The postcentral sulcal complex and the transverse postcentral sulcus and their relation to sensorimotor functional organization. Eur. J. Neurosci. 43, 1268-1283.

4 Mapping the complex topological organization of the human parietal face area

Ruey-Song Huang[1*], Ching-fu Chen[2], Martin I. Sereno[3,4]

[1]*Institute for Neural Computation, University of California, San Diego, La Jolla, CA 92093, USA*

[2]*Department of Electrical and Computer Engineering, University of California, San Diego, La Jolla, CA 92093, USA*

[3]*Birkbeck/UCL Centre for NeuroImaging (BUCNI), London WC1E 7HX, UK*

[4]*Department of Psychology and Neuroimaging Center, San Diego State University, San Diego, CA 92182, USA*

*Address correspondence to:
Ruey-Song Huang
Institute for Neural Computation
University of California, San Diego
9500 Gilman Dr. #0559
La Jolla, CA 92093-0559
Phone/fax: (858) 822-5977
Email: rhuang@ucsd.edu

This chapter has been published in NeuroImage *Volume 163 (2017), pages 459-470.*

4.0 Abstract

The macaque monkey ventral intraparietal area (VIP) contains neurons with aligned visual-tactile receptive fields anchored to the face and upper body. Our previous fMRI studies using standard head coils found a human parietal face area (VIP+ complex; putative macaque VIP homologue) containing superimposed topological maps of the face and near-face visual space. Here, we construct high signal-to-noise surface coils and used phase-encoded air puffs and looming stimuli to map topological organization of the parietal face area at higher resolution. This area is consistently identified as a region extending between the superior postcentral sulcus and the upper bank of the anterior intraparietal sulcus (IPS), avoiding the fundus of IPS. Using smaller voxel sizes, our surface coils picked up strong fMRI signals in response to tactile and visual stimuli. By analyzing tactile and visual maps in our current and previous studies, we constructed a set of topological models illustrating commonalities and differences in map organization across subjects. The most consistent topological feature of the VIP+ complex is a central-anterior upper face (and upper visual field) representation adjoined by lower face (and lower visual field) representations ventrally (laterally) and/or dorsally (medially), potentially forming two subdivisions VIPv (ventral) and VIPd (dorsal). The lower visual field representations typically extend laterally into the anterior IPS to adjoin human area

AIP, and medially to overlap with the parietal body areas at the superior parietal ridge. Significant individual variations are then illustrated to provide an accurate and comprehensive view of the topological organization of the parietal face area.

Keywords: near-face space, superior parietal cortex, multisensory maps, human VIP+ complex, topological models

4.1 Introduction

One of the primary functions of the posterior parietal cortex (PPC) is to integrate information across different sensory modalities. Single-unit recording studies have shown that neurons in the macaque ventral intraparietal area (VIP) respond to visual, tactile, auditory, and vestibular stimulation (Avillac et al., 2005, 2007; Bremmer et al., 2002; Chen et al., 2011; Colby et al., 1993; Duhamel et al., 1991, 1998; Schlack et al., 2005). In particular, area VIP contains neurons with aligned visual-tactile receptive fields (RFs) that are anchored to different regions on the face and upper body (Duhamel et al., 1991, 1998). However, detailed cortical maps of these bimodal RFs in macaques have been difficult to establish because of: (1) the location at the fundus of the intraparietal sulcus (IPS), (2) the small extent – about 5 mm in each dimension, and (3) unavoidable uncertainty in precisely locating depth electrode recording locations across long-lasting chronic awake-behaving recording experiments. Nevertheless, more recent studies in macaques have hinted that there might be multiple subdivisions of macaque VIP (Gattass et al., 2005; Guipponi et al., 2013; Lewis and Van Essen, 2000a, 2000b; Patel et al., 2010).

In humans, a region in the IPS was found to respond to visual, tactile, and auditory motion stimuli in functional magnetic resonance imaging (fMRI) experiments (Brem-

mer et al., 2001). We subsequently identified a multisensory parietal face area (a putative human homologue of macaque area VIP) in a similar though slightly more superior location, extending between the superior postcentral sulcus and the anterior IPS, by presenting wide-field videos and optic flow stimuli immediately in front of the subject's face and by delivering air puffs to randomized locations on the face in fMRI experiments (Huang and Sereno, 2007; Sereno and Huang, 2006). We then used phase-encoded paradigms (Engel, 2012; Sereno et al., 1995) to further define the rough retinotopic and somatotopic organization within that area. A direct overlay of visual and tactile maps on the same cortical surface revealed at least one aligned multisensory representation of the contralateral visual hemifield and contralateral hemiface in each hemisphere (e.g., the lower right visual field representation overlaps with the right chin, and so on upward in the visual field and on the face). Initial evidence suggested that this area might contain multiple aligned visual-tactile representations (e.g., see Subject 2 in Fig. 4 and Subject 6 in Fig. 6 in Sereno and Huang, 2006). However, the imaging resolution (3.1×3.1×4 mm voxels) in our previous studies was insufficient to discern the subdivisions in all of the subjects (see Supplementary material). While it is straightforward to acquire functional images at a higher spatial resolution (e.g., 2×2×2 mm or smaller voxels), the signal-to-noise ratio (SNR) in periodic fMRI signals drops significantly with

smaller voxels when using standard head coils in 3 Tesla MRI scanners (Hoffmann et al., 2009). In phase-encoded mapping experiments, successful reconstruction of detailed retinotopic or somatotopic maps depends on precise estimation of the phase angles of periodic signals with high SNR in individual voxels (Chen et al., 2017). This makes mapping in small, higher-level cortical regions particularly challenging because the SNR there is generally lower than that in the early unisensory areas.

In this study, we developed surface coil arrays to refine the detailed topological organization within the human parietal face area with a spatial resolution and SNR higher than is typically achieved by using standard head coils in 3 Tesla scanners. The smaller-sized (resulting in higher SNR) surface coil arrays were placed directly over the superior parietal region (resulting in additional SNR increase from increased proximity to the cortex) to compensate for the loss of SNR due to much smaller voxel volume and then hand-tuned individually for each subject. In the first experiment, an MR-compatible tactile stimulation device (the 12-channel air-puff “Dodecapus” manifold in Huang and Sereno, 2007) was mounted above the surface coils to deliver phase-encoded tactile stimuli around the face. In the second experiment, phase-encoded looming visual stimuli were projected onto a wide-field direct-view screen while phase-encoded tactile stimuli were delivered to the face via a wearable mask containing built-in air tubes and nozzles

(Chen et al., 2017; Huang et al., 2012). These experiments clearly revealed one and often two or more subdivisions within the parietal face area across hemispheres and subjects. Intersubject spherical morphing and surface-based complex-valued group-averaging techniques were used to summarize the location and extent of the parietal face area in relation to neighboring unisensory and multisensory areas in the superior parietal cortex. To demonstrate interhemispheric and intersubject variability in the topological organization of the parietal face area, we compare results from the current study with single-subject maps (most previously unpublished) from our previous studies acquired using standard head coils (Huang and Sereno, 2007, 2013; Huang et al., 2012; Sereno and Huang, 2006). Finally, we construct a set of topological models of the parietal face area to illustrate consistent and variable topological features observed within and across subjects.

4.2 Materials and Methods

4.2.1 Participants

Ten healthy adults (age 20-42, 5 female) with normal or corrected-to-normal vision participated in the new high-SNR surface-coil experiments. All subjects gave informed consent according to protocols approved by the Human Research Protections Program of the University of California, San Diego (UCSD). Five subjects (3 female) participated in Experiment 1, and the other five subjects (2 female) participated in Experiment 2. Data of two subjects in Experiment 2 were rejected due to severe motion artifacts or absence of significant activation in both hemispheres. For comparison with data acquired using standard 8-channel head coils, the Supplementary material includes published and unpublished single-subject maps from our previous studies (Huang and Sereno, 2007, 2013; Huang et al., 2012; Sereno and Huang, 2006). In total, visual and/or tactile maps of 26 distinct subjects are illustrated in this study.

4.2.2 Devices

We built MR-compatible devices to allow radio-frequency signal acquisition to be integrated with tactile and visual stimulation on and near the face (Fig. 4.1; for details of tactile stimulation devices, see Huang and Sereno, 2007 and Huang et al., 2012). The

signal acquisition system consisted of two 8-cm receive-only surface coils, a figure-8 passive detuning coil, and a bank of 8 preamplifiers (Fig. 4.1C; designed and fabricated by Larry May, development engineer at the UCSD Center for fMRI). The two-element surface coils were mounted symmetrically on the back of a baseball helmet (with its anterior part cut off) anchored to a supporting cradle. To reduce signal crosstalk between the two surface coils, the figure-8 coil was situated over them, partially overlapping both. The locations of active surface coils were determined empirically and iteratively in multiple pilot structural scans to ensure maximum image intensity in bilateral superior parietal cortex across subjects (Fig. 4.1D). Before each fMRI session, surface coils were individually fine-tuned while the subject was on a scanner bed pulled out of the MRI room. During the tuning of coil #1, radio-frequency reflection from coil #2 was attenuated by shorting it with a 50-ohm terminator. Variable capacitors on coil #1 were tuned using a spectrum analyzer (HP 8565A, Hewlett Packard) to achieve a maximum signal gain at the resonance frequency (peak at 127.72 MHz of our nominal 3-Tesla MRI scanners). The tuning procedure was then applied to coil #2 while coil #1 was being shorted. This back-and-forth procedure was repeated until maximum possible gain on both coils was achieved. Subject-specific hand-tuning of coils provides third, independent SNR advantage over standard head coils (beyond SNR increases due to a smaller coil size and

closer placement to the cortex).

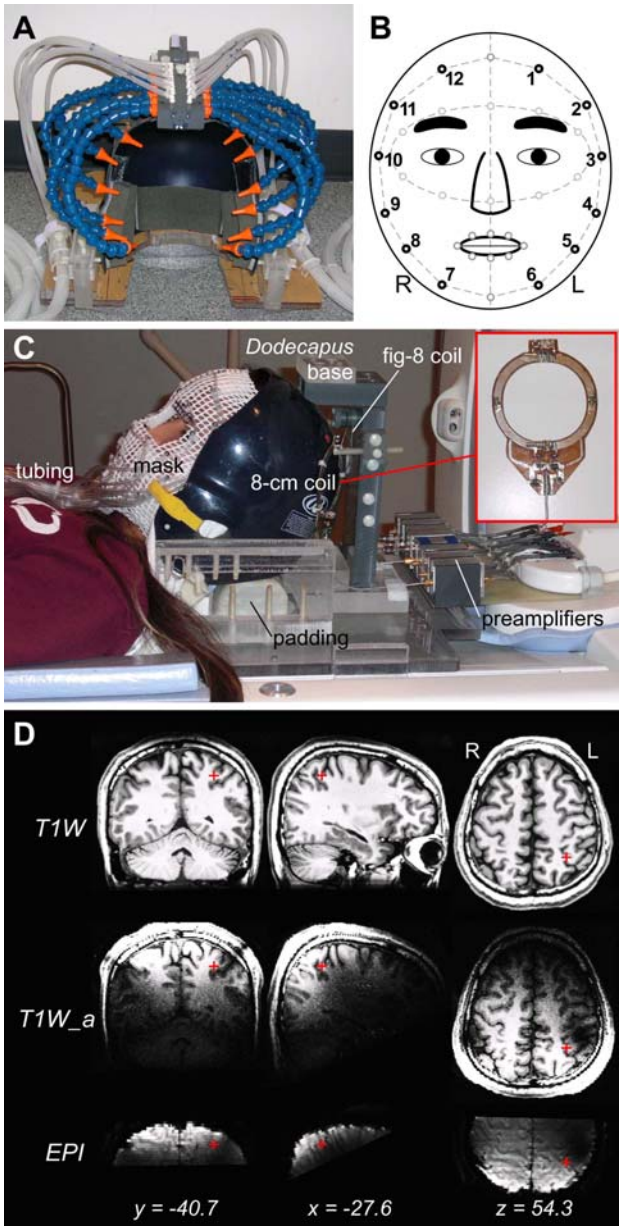

Fig. 4.1: MRI-compatible devices for radio-frequency signal acquisition and tactile stimulation. (**A**) Dodecapus manifold mounted above a baseball helmet for Experiment 1. (**B**) A schematic of stimulation sites (black circles) on the face in both experiments. (**C**) Integration of wearable tactile stimulation (mask) and surface coils for Experiment 2. (**D**) Location of the parietal face area (red cross) in the left hemisphere of Subject 1. T1W: T1-weighted structural images (average of two image sets); T1W_a: T1-weighted alignment images; EPI: functional images.

4.2.3 Experimental Design and Setup

Experiment 1

Somatotopic organization within the parietal face area was mapped using phase-encoded stimuli delivered by the Dodecapus tactile stimulation system (Huang and Sereno, 2007). The Dodecapus manifold was firmly mounted above the helmet on a base bolted down to the supporting cradle (Fig. 4.1A and C). The subject lay supine on the scanner bed with his/her head tilted forward (supported by foam padding underneath the head and neck) inside the helmet. Each “leg” (Loc-Line Modular Hose; Lockwood Products, Inc., OR) of the Dodecapus manifold was manually adjusted to aim its nozzle at one of twelve locations evenly distributed around the face, avoiding the eyes, nose, and mouth (locations #1 to #12 in Fig. 4.1B). In each of two repeated 512-s scans, a sequence of air puffs (with gaps between successive puffs) was delivered to location #1 at the left forehead for 5.33 s, and then to each of the subsequent locations (locations #2 to #12) within a 64-s cycle (8 cycles total). Within each 5.33-s period at each location, each 100-ms air puff was followed by a gap of 100 ms (80% probability) or 200 ms (20% probability). At the end of each 5.33-s period, an incomplete air puff or gap was terminated at the current location, and a full 100-ms air puff was delivered to the next location. Before the subject was moved into the scanner bore, tactile stimuli

were tested for at least a full cycle to ensure that they could be clearly felt at each location on the face. The air puffs were described by subjects as easily detectable but pleasant. During functional scans, all subjects were instructed to close their eyes in complete darkness and covertly attend to the pulsation pattern and the locations of air puffs on their face.

Experiment 2

In the second experiment, retinotopic and somatotopic organization within the parietal face area was mapped in four 512-s scans (two visual followed by two tactile scans) within the same fMRI session. To prevent occlusion and clear near-face space for a close-up screen, phase-encoded tactile stimuli (air puffs) were delivered to 12 locations around the face via plastic tubes embedded on a wearable mask custom molded for each subject (Fig. 4.1B and C; Chen et al., 2017; Huang et al., 2012). Each mask was made of X-Lite thermoplastic sheets with a grid of ~0.5×0.5 cm. Flexible air tubes were attached to the outside of the mask and were each terminated with an elbow fitting (Part No. FTPP-L210NP; Omega Engineering, Inc., OR) to redirect airflow perpendicularly to the face through a mesh opening. The open end of the elbow was approximately 5 mm above each stimulation site on the skin of the face. The other end of each tube was connected via quick connectors (Part No. SMM01, SMF01; Colder Products Com-

pany, MN) to a bundle of 25-ft tubes, which extended through a wave guide and then connected to the stimulus control system located in the MRI console room (see Fig. S1 in Huang et al., 2012). Fiducial points marked on the mask during face molding were used to precisely align them with the corresponding points on the face (e.g., eyebrows) during experimental setup. After testing tactile stimuli on the face for at least a full cycle, the subject was moved to the isocenter within the scanner bore and a direct-view screen was then installed about 15 cm directly in front of the subject's eyes. Visual stimuli were back-projected by an LCD projector (Dell 3300MP; 1024 × 768 pixels) onto a 35×26 cm screen region, yielding a field of view of ~100×80°. In each of two repeated visual scans, phase-encoded looming balls appeared at a polar angle that advanced in a counterclockwise direction periodically (Supplementary Figure 4.S1; also see details in Methods – Visual Mapping Paradigm and Fig. S6 in Huang et al., 2012). Subjects were instructed to fixate a central cross while attending to each looming ball apparently passing by their faces. Subjects were also required to press a key on a fiber-optic response pad (Current Designs, Inc.) when a white ball randomly turned red in 20% of all trials. All apparatus and setup remained unchanged following two visual scans, except that the projector was turned off. In each of two repeated tactile scans, tactile stimuli with the same design and parameters as in Experiment 1 were then delivered to the

face via the mask while the subject closed his/her eyes in complete darkness.

In both experiments, compressible foam padding was firmly inserted into the gap between the head and the helmet to restrict head movements. All subjects had previously participated in multiple sessions of fMRI experiments and were experienced in remaining motionless without using a bite-bar. Subjects were instructed to attempt to remain motionless in the helmet during the entire scanning session.

4.2.4 Data acquisition

Subjects were scanned in a General Electric 3 Tesla scanner at the UCSD Center for Functional MRI. Each subject participated in an fMRI session consisting of 2-4 functional scans and one anatomical alignment scan, which were all acquired using the custom-built surface coils (Fig. 4.1C). Functional images were acquired with a single-shot echo-planar imaging (EPI in Fig. 4.1D; bandwidth = 62.5 kHz) pulse sequence with the following parameters: (1) Experiment 1: TR = 2 s, TE = 35.4 ms, flip angle = 90°, FOV = 200×200 mm, 16 axial slices, thickness = 2.6 mm, gap = 0 mm, in-plane voxel size = 1.56×1.56 mm, matrix = 128×128, 256 images per slice (512 s per scan); (2) Experiment 2: TR = 2 s, TE = 35.9 ms, flip angle = 90°, FOV = 192×192 mm, 15 axial slices, thickness = 2.4 mm, gap = 0 mm, in-plane voxel size = 1.5×1.5 mm, matrix =

128×128, 256 images per slice (512 s per scan). In both experiments, alignment images were acquired at the same orientation as functional images by a fast spoiled gradient echo (FSPGR) pulse sequence: FOV = 256×256 mm, 106 axial slices, thickness = 1.3 mm, in-plane voxel size = 1×1 mm, and matrix = 256×256 (T1W_a in Fig. 4.1D). In a different session, each subject was scanned using a standard 8-channel head coil, and two sets of high-resolution structural images were acquired by an FSPGR pulse sequence with parameters: FOV = 256×256 mm, 160 axial slices, voxel size = 1×1×1 mm, and matrix = 256×256 (T1W in Fig. 4.1D). For each subject, cortical surfaces were reconstructed from the registered average of these two image sets using the FreeSurfer package (Dale et al., 1999; Fischl et al., 1999a).

4.2.5 Data analysis

Functional images were motion-corrected and then registered to the last functional scan immediately before the alignment scan using the *3dvolreg* tool of the Analysis of Functional NeuroImages (AFNI) package (Cox, 1996). For each voxel, a time-point-wise average was applied to the time series (256 sample points) of two repeated functional scans of the same stimulation modality. For each voxel, linear trends were removed from the averaged time series (256 sample points), and a power spectrum

(128 bins between 0-127 cycles/scan) was obtained by discrete Fourier transform:

$$X_m(\omega) = \sum_{t=1}^{256} x_m(t) e^{-j\omega t} = \left|X_m(\omega)\right| e^{j\theta_m(\omega)}, \quad (4.1)$$

in which $x_m(t)$ is the time series in voxel m, and $X_m(\omega)$, $\left|X_m(\omega)\right|$, and $\theta_m(\omega)$ are the complex component, amplitude, and phase angle at frequency ω. The "signal" in the power spectrum is defined as the complex component at the stimulus frequency ($\omega_s = 8$ cycles/scan) while the "noise" is defined as the complex components at the remaining frequencies ($\omega_n = 0-127$ cycles/scan; excluding 0-2, 7-9, 15-17, 23-25, and 32 cycles/scan). For a voxel m, an *F*-statistic (F_m) was estimated from the ratio between the signal energy $\left|X_m(\omega_s)\right|^2$ and the average of noise energy $\left|X_m(\omega_n)\right|^2$:

$$F_m = \frac{\left|X_m(\omega_s)\right|^2 \Big/ df_s}{\left(\sum_{\omega_n} \left|X_m(\omega_n)\right|^2\right) \Big/ df_n}. \quad (4.2)$$

A *p*-value was then estimated by considering the degrees of freedom (*df*) of signal ($df_s = 2$ for real and imaginary parts at the stimulus frequency) and noise ($df_n = 230$ for the remaining frequencies) in F_m. For a voxel m, a complex number $\left(F_{m,\mathrm{r}}, F_{m,\mathrm{i}}\right)$ incorporating both *F*-statistic and phase angle, $\theta_m(\omega)$, was computed by $F_{m,\mathrm{r}} = f_m \cos(\theta_m(\omega))$ and $F_{m,\mathrm{i}} = f_m \sin(\theta_m(\omega))$, where f_m is the square root of F_m. Voxels with an *F*-statistic higher than a single threshold were selected and projected onto corresponding vertices on the cortical surfaces using FreeSurfer. The phase angle, $\theta_m(\omega)$, and f_m of each

vertex were indicated by color hue and saturation, according to a color wheel representing the contralateral hemiface (or visual hemifield) (Figs. 4.2 and 4.3).

The distribution of signal phase angles within each sROI is characterized using circular statistics (Chen et al., 2017). For a vertex v in an sROI r with V vertices corresponding to stimulus modality s, the phase angle, $\theta_{v,s}$, was first converted to the corresponding complex number, $z_{v,s} = \exp\left(j\theta_{v,s}\right)$. The mean phase angle in this sROI, $\overline{\theta}_s^{(r)}$, was then obtained by (Fisher, 1993):

$$\overline{z}_s^{(r)} = \frac{1}{V}\sum_{v=1}^{V} z_{v,s} = \frac{1}{V}\sum_{v=1}^{V} \exp\left(j\theta_{v,s}\right) = \exp\left(j\overline{\theta}_s^{(r)}\right). \tag{4.3}$$

For vertices activated by both visual and tactile stimuli within an sROI, r, the association between the phase angles of two modalities, s_1 and s_2, was described by a bimodal circular correlation coefficient, $\rho_{12}^{(r)}$, defined as (Jammalamadaka and SenGupta, 2001):

$$\rho_{12}^{(r)} = \frac{\sum_{v=1}^{V}\left[\sin\left(\theta_{v,s_1} - \overline{\theta}_{s_1}^{(r)}\right)\sin\left(\theta_{v,s_2} - \overline{\theta}_{s_2}^{(r)}\right)\right]}{\sqrt{\left[\sum_{v=1}^{V}\sin^2\left(\theta_{v,s_1} - \overline{\theta}_{s_1}^{(r)}\right)\right]\left[\sum_{v=1}^{V}\sin^2\left(\theta_{v,s_2} - \overline{\theta}_{s_2}^{(r)}\right)\right]}}. \tag{4.4}$$

A *p*-value of $\rho_{12}^{(r)}$ was then estimated from the distribution of $\sqrt{V}\frac{\sqrt{\hat{\lambda}_{20}\hat{\lambda}_{02}}}{\sqrt{\hat{\lambda}_{22}}}$ (Jammalamadaka and SenGupta, 2001), where

$$\hat{\lambda}_{ij} = \frac{1}{V}\sum_{v=1}^{V}\left[\sin^i\left(\theta_{v,s_1} - \overline{\theta}_{s_1}^{(r)}\right)\sin^j\left(\theta_{v,s_2} - \overline{\theta}_{s_2}^{(r)}\right)\right]. \tag{4.5}$$

When V is large, $\sqrt{V}\frac{\sqrt{\hat{\lambda}_{20}\hat{\lambda}_{02}}}{\sqrt{\hat{\lambda}_{22}}}\rho_{12}^{(r)}$ forms a standard normal distribution; thus, the signifi-

cance of $\rho_{12}^{(r)}$ can be verified under the null hypothesis $\rho_{12}^{(r)} = 0$. If the phase angles of vertices in the overlapping region of an sROI r in response to two different stimulus modalities s_1 and s_2 are independent, $\rho_{12}^{(r)} = 0$; but the reverse may not be true.

4.3 Results

4.3.1 Surface coil performance and sROI measurement

The signal gain of each surface coil was individually tuned prior to each fMRI session, but the resulting functional images did not always exhibit exactly symmetric distribution of SNR in both hemispheres (Fig. 4.1D; also see surface-based SNR maps in Supplementary Figure 4.S2). In sessions where a comparable SNR was measured bilaterally, some subjects only show significant periodic activation ($p < 0.05$, uncorrected) at the superior parietal cortex in one hemisphere. While technical limits of coil tuning (e.g., intrinsic gain of electronic components) could partially account for the interhemispheric imbalance, it is common to observe that a higher-level topological area may be missing a partial to complete hemifield representation unilaterally in phase-encoded mapping experiments due to temporally uneven distribution of attention throughout the scan (e.g., see Hagler et al., 2007; Huang et al., 2012). Here, we only show positive results with somatotopic maps rendered on eight hemispheres of five subjects in Experiment 1 (Fig. 4.2), and aligned retinotopic and somatotopic maps rendered on three right hemispheres of three subjects in Experiment 2 (Fig. 4.3). Tables 4.1 and 4.2 summarize the peak activation location (Talairach coordinates), surface area, volume (voxels), and statistics for each sROI outlined in Figs. 4.2 and 4.3. Across subjects in both experi-

ments, the parietal face area was identified as a contiguous region located at the superior postcentral sulcus, slightly extending onto the postcentral gyrus in some subjects. Across subjects, the surface area of each sROI ranges from 114 to 496 mm^2 (equivalent to a square area of about 10.7×10.7 to 22.3×22.3 mm), and the total volume of all voxels enclosed in each sROI ranges from 394 to 1276 mm^3.

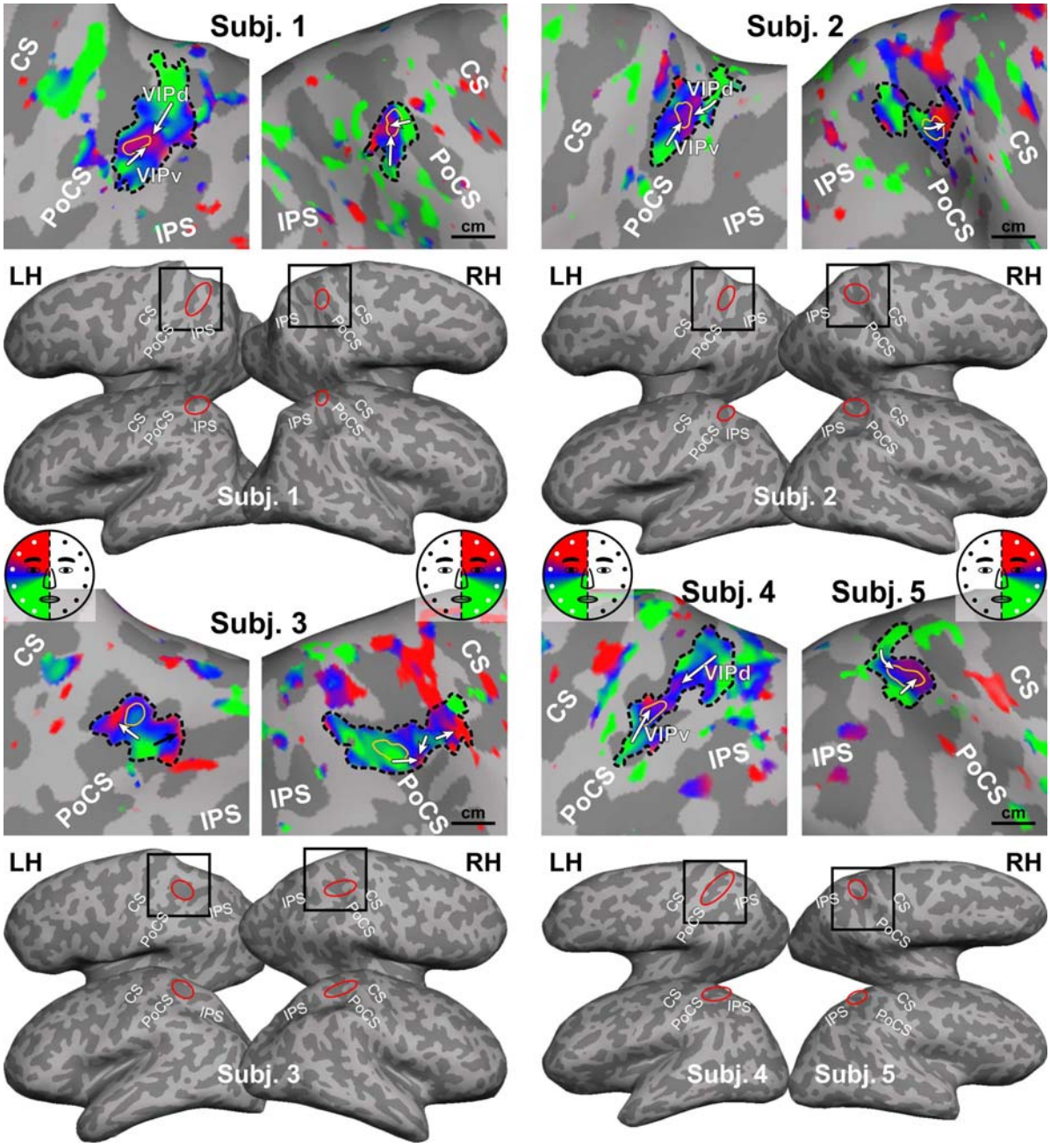

Fig. 4.2: Somatotopic maps of five subjects in Experiment 1. All maps were rendered with the same statistical threshold ($F_{2,230} = 3.035$, $p = 0.05$, uncorrected). Black box: location of each close-up map on the dorsal-lateral cortical surface; Red ellipse: location of the parietal face area on each cortical surface; Dashed black contour: an sROI of the parietal face area; Thin yellow contour: the peak activation region within an sROI; A white or black arrow: a lower-to-upper progression of the contralateral hemiface representation (see color wheel); CS: central sulcus; PoCS: postcentral sulcus; IPS: intraparietal sulcus; LH/RH: left/right hemisphere.

Table 4.1: Measurements and statistics of sROIs in Experiment 1.

	sROI				Peak activation region			
Subject / hemisphere	Surface area (mm^2)	Vertices	Voxels	Total volume (mm^3)	Surface area (mm^2)	Voxels	Average Talairach coordinates	Average *p*-value*
1 / LH	361	606	201	1276.4	14.8	8	(-27.6, -40.7, 54.3)	6.6×10^{-10}
1 / RH	121.1	300	96	609.6	14.7	13	(33.7, -35.8, 53.5)	6.4×10^{-11}
2 / LH	173.9	313	105	666.8	14	10	(-28.6, -39.7, 61.0)	2.0×10^{-10}
2 / RH	114.2	262	80	508	19	14	(27.0, -41.9, 56.3)	2.9×10^{-11}
3 / LH	192.2	220	62	393.7	16.2	7	(-21.5, -38.1, 58.3)	4.6×10^{-7}
3 / RH	287.7	641	200	1270	22.6	7	(26.3, -37.8, 50.4)	1.9×10^{-16}
4 / LH	275.5	532	171	1085.9	18.1	9	(-19.7, -35.8, 39.7)	9.3×10^{-5}
5 / RH	144.5	286	131	831.9	33.6	7	(23.1, -39.5, 70.5)	1.1×10^{-9}

See corresponding sROI (dashed black contours) and peak activation regions (thin yellow contours) in Fig. 4.2.

Volume per voxel: 6.35 mm^3; *: FDR corrected.

Table 4.2: Measurements and statistics of sROIs in Experiment 2.

	sROI				Peak activation region				Visual-tactile alignment	
Subject / Modality	Surface Area (mm^2)	Vertices	Voxels	Total volume (mm^3)	Surface Area (mm^2)	Voxels	Average Talairach coordinates	Average *p*-value*	Overlapping vertices (%)†	Circular correlation coefficient, *p*-value‡
6 / Visual	222.3	545	172	928.8	15.6	18	(34.3, -37.5, 64.6)	9.7×10^{-10}	82.2	0.38, $p < 4.03\times10^{-11}$
6 / Tactile					14	16	(31.1, -38.0, 65.8)	1.3×10^{-14}		
7 / Visual	496.4	1012	118	637.2	13.5	8	(32.1, -41.8, 62.5)	7.5×10^{-15}	30.93	0.66, $p = 0$
7 / Tactile					20.3	10	(35.0, -43.3, 63.1)	3.8×10^{-5}		
8 / Visual	176.6	347	96	518.4	14.9	13	(24.0, -36.9, 57.7)	1.0×10^{-5}	78.1	0.06, $p = 1$ (n.s.)
8 / Tactile					14.1	10	(24.3, -37.3, 58.1)	0		

See corresponding sROI (dashed black contours) and peak activation regions (thin yellow contours) in Fig. 4.3.

Volume per voxel: 5.4 mm^3; *: FDR corrected; †: percentage of vertices in an sROI with $p < 0.05$ (uncorrected) in both modalities; ‡: Bonferroni-corrected *p*-value estimated from overlapping vertices only; n.s.: not significant.

4.3.2 BOLD signal changes

Supplementary Figures 4.S3 and 4.S4 show time courses of blood-oxygen-level dependent (BOLD) signals averaged across voxels enclosed in each peak activation region (outlined in a thin yellow contour) within each sROI (outlined in a dashed black contour) in Figs. 4.2 and 4.3; also see measurements and statistics of sROIs in Tables 4.1 and 4.2. To better characterize the BOLD signal change in response to periodic stimulation, a waveform was reconstructed by inverse Fourier transforming the periodic components (harmonics: 8, 16, and 24 cycles per scan) on the power spectrum of the average BOLD signal in each peak activation region. Across subjects and stimulus modalities, the peak-to-peak signal change of the reconstructed periodic waveform (thick gray curves in Figs. 4.S3 and 4.S4) ranges from 0.74 to 2.59%. To demonstrate the maximum temporal SNR that surface coils can achieve, Supplementary Figures 4.S5 and 4.S6 show the original time course and a waveform reconstructed from the periodic components in a single voxel identified with the highest peak-to-peak signal change (ranging from 1.8 to 14.8%) within each peak activation region in Figs. 4.2 and 4.3.

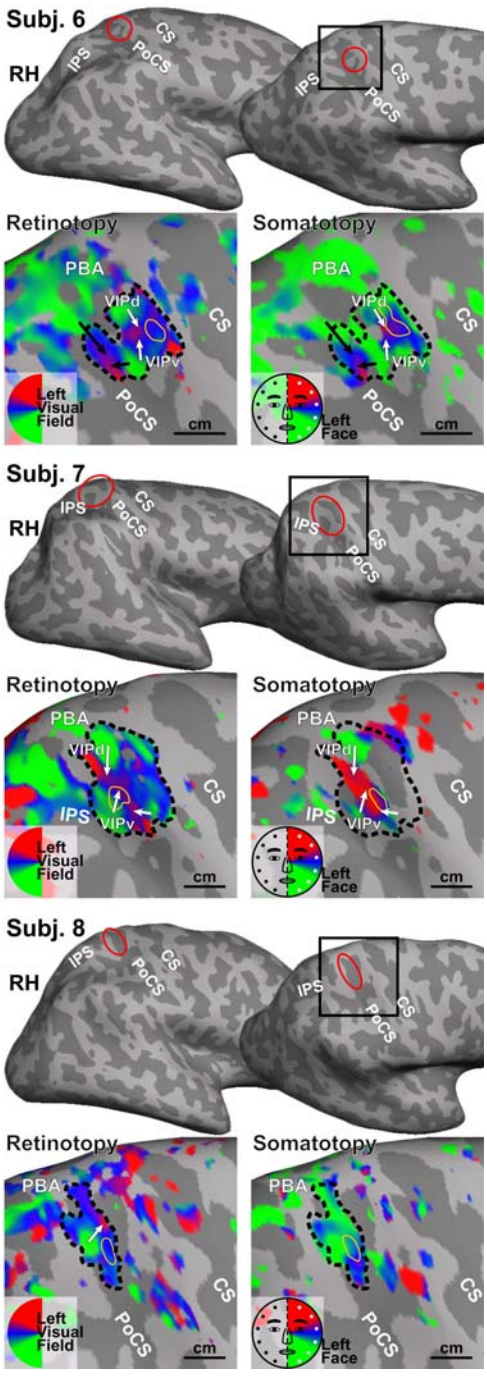

Fig. 4.3: Retinotopic and somatotopic maps of three subjects in Experiment 2. All maps were rendered with the same statistical threshold ($F_{2,230} = 3.035$, $p = 0.05$, uncorrected). Each sROI is outlined in the retinotopic map and then superimposed on the somatotopic map. PBA: parietal body areas. Other conventions as in Fig. 4.2.

4.3.3 Average location and extent

To illustrate intersubject variability in location and extent of the parietal face area in Figs. 4.2 and 4.3, activation maps of each subject were spherically morphed to the *fsaverage* sphere in FreeSurfer package using a sulcus-based criterion and then back-sampled to the cortical surfaces of a representative subject (Fig. 4.4A; see methods in Fischl et al., 1999b; Hagler et al., 2007). The contour of each sROI was outlined from each morphed map and then superimposed on the same cortical surface. Surface-based group-average maps of lip, face, finger, shoulder, and leg representations as well as maps of video-driven visual cortex from our other studies (Huang and Sereno, 2007, 2013, 2018; Huang et al., 2012) were back-sampled onto the same cortical surfaces in Fig. 4.4A. Across subjects, the parietal face area is consistently found at the superior part of the postcentral sulcus, where it extends anteriorly to border the finger (hand) representations in the primary somatosensory cortex (S-I) at the superior postcentral gyrus; inferiorly and laterally to adjoin the parietal hand/finger area (human homologue of macaque anterior intraparietal area [AIP]; Borra et al., 2008; Culham et al., 2003; Guipponi et al., 2013; Jastorff et al., 2010); and medially/superiorly to overlap with the parietal body areas (PBA, including shoulder and leg representations; Huang et al., 2012). In the group-average visual maps (Fig. 4.4A), the parietal face area is located at the ante-

riormost end of the superior-parietal stream (one of the dorsal visual streams) activated by wide-field videos or simulated egomotion (Huang and Sereno, 2013, 2018; Huang et al., 2015; Sereno and Huang, 2014).

Table 4.3: Classification of single-subject maps by topological types.

Type	Modality	Figure	Subject #
1.0	Tactile	S7	9, 10, 11
		S8	2^{v}, 2^{v}, 9, 12^{v}, 13^{v}, 14^{v}
	Visual	S10	5^{v}, 8^{v}, 12
1.1	Tactile	S7	12
		S8	5, 5
	Visual	S9	13^{v}
		S10	1^{v}, 2^{v}, 14^{v}, 17^{v}, 19^{v}
1.2	Visual	S9	11, 12^{v}, 25^{v}
		S10	9, 11, 18, 25^{v}
1.3	Visual	S9	5^{v}, 19^{v}, 20
2.0	Tactile	S7	1, 1, 2^{v}, 4
		S8	7^{v}, 11^{v}
	Visual	S9	1, 2^{v}, 4, 15
		S10	7^{v}, 13^{v}, 16^{v}, 20^{v}
2.1	Tactile	S8	1^{v}, 1^{v}
2.2	Tactile	S7	2^{v}
	Visual	S9	22, 24^{v}
2.3	Tactile	S7	3^{v}, 3^{v}
		S8	6^{v}
	Visual	S9	3^{v}, 9^{v}, 10, 16^{v}, 17, 18, 21^{v}, 23^{v}
		S10	6^{v}, 24^{v}, 26^{v}
None	Tactile	S7	13, 14
		S8	3, 3, 8, 10
	Visual	S9	14
		S10	3, 10, 15, 21, 23

See topological types in Fig. 4.4B. Subject #: head-coil session; Subject #: surface-coil session; Subject $\#^{v}$ or $\#^{v}$: type variation.

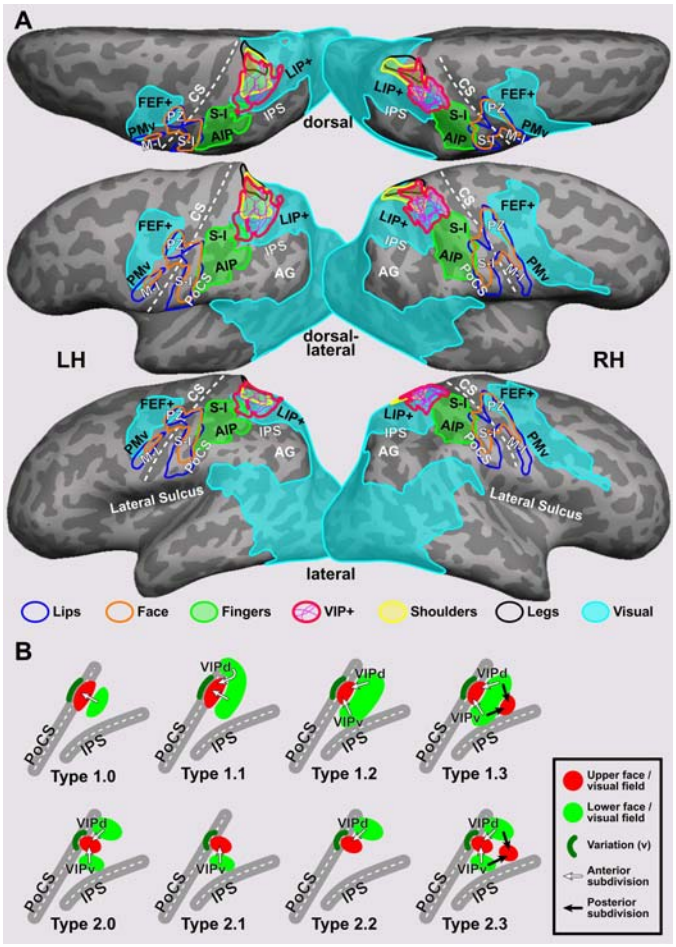

Fig. 4.4: Location, extent, and models of the parietal face area. (**A**) The cortical surfaces of Subject 1 were overlaid with contours of the parietal face area sROI spherically morphed from four left hemispheres and seven right hemispheres of eight subjects in Figs. 4.2 and 4.3. A thin magenta contour indicates the border of a single-subject sROI, and a thick magenta contour indicates the common external border of all sROI. Group-average contours of lip, face, and finger (hand) representations in the primary somatosensory cortex (S-I) and parietal body areas (PBA; including shoulder and leg representations) were obtained by passive tactile stimulation in previous studies (Huang et al., 2012; Huang and Sereno, 2007). Group-average contours of video-driven visual cortex were obtained from Huang and Sereno (2018). (**B**) Schematic topological models of the parietal face area (VIP+ complex) in the left hemisphere (see single-subject maps in Fig. 4.S7-4.S10 and map classification in Table 4.3). FEF+: frontal eye field complex; PZ: polysensory zone; PMv: ventral premotor cortex; M-I: primary motor cortex; AIP: anterior intraparietal area; LIP+: human homologue of macaque area LIP; AG: angular gyrus. Other abbreviations as in text and Fig. 4.2.

4.3.4 Topological organization

Results of topological mapping are illustrated in detail for one representative subject in each experiment (Figs. 4.2 and 4.3), and then compared within and across subjects in the following sections. In Experiment 1, the parietal face area in each hemisphere of Subject 1 is identified as a contiguous sROI showing significant periodic activation (thresholded at $F_{2,230} = 3.035$, $p = 0.05$, uncorrected) at the superior part of the postcentral sulcus (PoCS), as indicated by a red ellipse over the inflated cortical surface in lateral and dorsal-lateral views (Fig. 4.2). Its location among neighboring sulci is consistent across the left and right hemispheres. Detailed somatotopic organization in each sROI is shown in a close-up view of the superior parietal lobule (as indicated by a black square over the dorsal-lateral surface). Here, we consider each sROI a compound map (cluster) without delineating borders that separate its potential subdivisions. An arrow is used to illustrate a continuous polar-angle progression from the lower face (colored in green) to upper face (colored in red) representations on the cortical surface. The sROI in Subject 1's left hemisphere (LH) contains two clear contralateral hemiface subdivisions, with their upper face representations adjoining each other centrally and two separate lower face representations extending ventrally (laterally) and dorsally (medially), which are tentatively labeled VIPv (ventral) and VIPd (dorsal) (see Discussion). The

sROI in Subjects 1's right hemisphere (RH) contains two small hemiface subdivisions, with their upper face representations adjoining each other centrally and lower face representations extending ventrally (laterally) and dorsal-anteriorly. The ventral subdivision is consistent with subdivision VIPv in the left hemisphere, while the dorsal-anterior subdivision is less commonly observed across subjects (see topological types in *Intersubject consistency and variability* below).

In Experiment 2, the parietal face area in the right hemisphere of Subject 6 is identified as an sROI containing aligned retinotopic and somatotopic maps of contralateral visual-tactile space at the superior postcentral sulcus (as indicated by a red ellipse in Fig. 4.3). The topological organization within this sROI shows two separated upper visual field (upper face) representations and two separated lower visual field (lower face) representations, which form a total of four aligned visual-tactile subdivisions, including VIPd and VIPv (indicated by white arrows) and two additional subdivisions posterior to both (indicated by black arrows; see Discussion). The overall overlap between retinotopic and somatotopic maps within this sROI is 82.2%, as estimated by the percentage of surface vertices showing significant activation ($F_{2,230} > 3.035$, $p < 0.05$, uncorrected) in response to both visual and tactile stimuli (Table 4.2). The degree of polar-angle alignment between retinotopic and somatotopic maps within this sROI is 0.38

($p < 4.03 \times 10^{-11}$, Bonferroni-corrected; Table 4.2), which is a bimodal circular correlation coefficient estimated from the overlapping vertices (see *Data analysis*).

4.3.5 Intersubject consistency and variability

The topological organization of the parietal face area exhibited high interhemispheric and intersubject variability in a moderate-sized group of subjects scanned with a high SNR method. Subjects (hemispheres) showing consistent topological features are summarized in groups. First, Subjects 2 (RH), 3 (LH), and 5 (RH) show a major hemiface representation with the upper face located anterior to the lower face representation. Second, Subjects 1 (LH), 2 (LH), 4 (LH), 6 (RH), and 7 (RH) show at least two hemiface (or visual hemifield) representations, namely VIPv and VIPd, where their upper face representations adjoin each other centrally and two separate lower face representations extend ventrally (laterally) and dorsally (medially). Third, Subjects 1 (RH), 3 (RH), and 8 (RH) show complex organization inconsistent with either of the above two groups. These results confirm that the parietal face area contains one or more subdivisions, as suggested in our previous studies (Sereno and Huang, 2006, 2014).

To better model the complex topological organization of the parietal face area across subjects, we reanalyzed visual and/or tactile maps in 23 subjects from our previ-

ous studies (Huang and Sereno, 2007, 2013; Huang et al., 2012; Sereno and Huang, 2006). Five subjects overlapped with the current study, which allowed us to measure within-subject and between-coil-type variability (see *Within-subject reproducibility*). Maps of 26 distinct subjects from the current and previous studies are sorted by their topological features in each hemisphere, as shown in Supplementary Figures 4.S7-4.S10 and summarized in Table 4.3. Within and across subjects, topological maps of the parietal face area (VIP+ complex) situated between the postcentral sulcus (PoCS) and intraparietal sulcus (IPS) are classified into two base types (Types 1.0 and 2.0), each with three subtypes (Fig. 4.4B). Without creating more types, we use "v" to indicate slight variations (adding or missing partial representations) on an existing base type or subtype; and use "none" to indicate unclassifiable maps (Figs. 4.S7-4.S10 and Table 4.3). One of the commonly observed variations is a small lower face (or visual field) representation situated anterior to the upper face (or visual field) representation at the superior PoCS, as indicated by a dark-green crescent in Fig. 4.4B. For each base type and its subtypes, detailed topological features are illustrated as follows.

Type 1.0 exhibits a single hemiface (or visual hemifield) map with the upper face (or visual field) representation situated anterior to the lower face (or visual field) representation (e.g., Subject 9 in Figs. 4.S7 and 4.S8). The posterior lower face (or visual

field) representation may extend dorsally (medially) to form Type 1.1 (e.g., Subject 5 in Fig. 4.S8), or extend both dorsally (medially) and ventrally (laterally) to form Type 1.2 (e.g., Subject 11 in Fig. 4.S9). Type 1.3 exhibits a second upper face (or visual field) representation situated posterior to a continuous strip of lower face (or visual field) representation, forming four lower-to-upper progressions (e.g., Subject 20 in Fig. 4.S9). The anterior subdivisions of VIP+ complex are indicated by white arrows, while the posterior subdivisions are indicated by black arrows (Figs. 4.4B, 4.S7-4.S10; see Discussion).

Type 2.0 exhibits a central upper face (or visual field) representation adjoined by two separate lower face (or visual field) representations ventrally (laterally) and dorsally (medially), e.g., Subject 1 in Fig. 4.S7. Missing either one of the lower face (visual field) representations in Type 2.0 forms Type 2.1 (e.g., Subject 1 in Fig. 4.S8) or Type 2.2 (e.g., Subject 22 in Fig. 4.S9). Type 2.3 exhibits a second upper face (or visual field) representation situated posterior to the VIPd/VIPv complex in Type 2.0, forming four lower-to-upper progressions (e.g., Subject 18 in Fig. 4.S9). Notably, Type 2.3 differs from Type 1.3 only in that its dorsal and ventral lower face (or visual field) representations are separated from each other (Fig. 4.4B; see Discussion).

4.3.6 Within-subject reproducibility

To demonstrate within-subject reproducibility of topological organization across sessions, we compare maps of the parietal face area acquired by surface coils (current study; in red boxes) and 8-channel head coils (previous studies; in blue boxes) within each of five subjects (Figs. 4.S7-4.S10). In Subject 1, the sROI in either hemisphere shows roughly the same activation location and extent (dashed black contours) as well as consistent topological organization in somatotopic maps that were acquired using different kinds of coils in different sessions (paired LH maps in Fig. 4.S7: Type 2.0; paired RH maps in Fig. 4.S8: Type 2.1v). In Subject 2, the sROI in either hemisphere shows consistent activation location and extent across sessions (paired LH maps in Fig. 4.S7; paired RH maps in Fig. 4.S8). However, the ventral lower face representation is missing from the LH head-coil map (Type 2.2v; Fig. 4.S7), which is present in the LH surface-coil map (Type 2.0v). In Subject 2's right hemisphere, the anterior portion the sROI (dashed black contours) shows a single subdivision that is consistent across sessions (both Type 1.0v in paired RH maps). In Subject 3, the left sROI shows consistent activation location across sessions (paired LH maps in Fig. 4.S7). However, the surface-coil map subtends only the ventral (lateral) portion of the head-coil map (as indicated by dashed black contours), and shows two consistent lower-to-upper face pro-

gressions (an incomplete Type 2.3v map). The right sROI of Subject 3 subtends an elongated region across the superior PoCS, with a slight offset across sessions (paired RH maps in Fig. 4.S8). However, neither map shows clear topological organization (Type: none). In Subject 5, the right sROI shows aligned activation location and extent as well as consistent topological organization across sessions (both Type 1.1; paired RH maps in Fig. 4.S8). Additionally, the left sROI of Subject 4 shows a consistent activation location and extent (with a slight offset) as well as consistent topological organization (Type 2.0) across sessions and modalities (see surface-coil tactile map in Fig. 4.S7 and head-coil visual map in Fig. 4.S9; head-coil tactile map unavailable).

4.4 Discussion

4.4.1 Macaque area VIP

Topological mapping of higher level areas in the posterior parietal cortex of non-human primates is challenging for single-unit recording studies, especially in awake behaving animal experiments. In particular, macaque area VIP is a small region located at the fundus of the IPS, making it difficult to reconstruct a VIP map from numerous recording sites distributed across slices and recording sessions spread over months or years. Recent monkey neuroimaging studies have begun to map detailed organization of the IPS at higher resolutions (~1.5 to 2 mm) and to display the results on inflated or flattened cortical surfaces (Guipponi et al., 2013; Patel et al., 2010).

4.4.2 High-resolution mapping with surface coils

In humans, the parietal face area occupies a cortical patch (sROI) of about 10×10 to 20×20 mm in the superior postcentral sulcus, and the total volume of voxels enclosed in each sROI is about 1000 mm^3 or less, as suggested by data in the current study (Tables 4.1 and 4.2). The imaging resolution (e.g., 3.1×3.1×4 mm) used in our previous studies was insufficient to clearly resolve some of the subdivisions in the parietal face area (Figs. 4.S7-4.S10; Huang and Sereno, 2007; Huang et al., 2012; Sereno

and Huang, 2006). It is straightforward to increase the imaging resolution by reducing the in-plane voxel size and slice thickness. However, SNR in the fMRI time course is also reduced roughly proportional to voxel volume, everything else held constant (Buxton, 2009; Hoffmann et al., 2009). The voxel volumes in the current study are less than 1/6 of those in our previous studies. Small, closely-placed, and hand-tuned surface coils have three potential SNR advantages: (1) smaller-sized coils receive less noise from other parts of the brain; (2) coil placement closer to the brain increases signals; and (3) subject-specific coil tuning further boosts signal gain. These three factors help compensate for the loss of SNR at smaller voxel volumes. However, there are several potential factors (e.g., imbalanced signal gains, crosstalk between coils) that can reduce the SNR of coil arrays, which may account for the weak or absent activation unilaterally in some of the subjects (negative results not shown).

In subjects showing high SNR in the superior parietal cortex (Fig. 4.S2), the peak activation region within each sROI shows a peak-to-peak signal change comparable to or higher than the 1-2% signal change commonly observed in fMRI experiments using standard voxel sizes (3-5 mm in each dimension). In this context, it is important to note that that all phase-encoded signals are essentially 'subtractions' – for a periodic signal to appear at all, one map position (polar angle) has to beat all other map positions. In

each subject in Experiment 2, the peak activation regions in visual and tactile scans closely overlapped with each other and they both exhibited a large (differential) signal change with high statistical significance (Figs. 4.3, 4.S4, 4.S6; Table 4.2). This provides direct evidence for aligned visual-tactile representations in the parietal face area at a high spatial resolution (5.4 mm^3 vs. standard 27-36 mm^3 per voxel). This is, however, still too coarse a resolution to determine whether multisensory signals come from the same columns or neurons, as has nevertheless been found to be the case in single-unit studies.

4.4.3 Locating human area VIP

In recent human fMRI studies, a number of confusingly differently located and differently named locations in between the postcentral sulcus and the anterior IPS have been proposed as the site of a putative human homologue (pVIP) of macaque area VIP. We discuss these in two groups, posterior and anterior.

Several studies have used optic flow stimuli (i.e., visual-only stimuli) to activate multiple areas in or near the anterior IPS (IPS5 in Konen and Kastner, 2008; VIP in Wall and Smith, 2008; pVIP in Cardin and Smith, 2010; IPSmot in Pitzalis et al., 2013). Another study showed that an area located at the confluence of the anterior IPS and PoCS

was activated by vibrotactile stimulation of the posterior neck muscles (VIP in Fasold et al., 2008; their left VIP appears more posterior than their right VIP). The locations of these five areas (four defined by visual stimuli only and one by vibrotactile stimuli only) overlap the posterior-lateral edge of the multisensory parietal face area identified in our previous and current studies (Sereno and Huang, 2006; Huang et al., 2012). However, none of these areas were shown to have aligned multisensory (visual and tactile) responses to stimuli near or on the face, which is critical to the functional definition of area VIP, as established by previous invasive studies in macaque monkeys (Avillac et al., 2005, 2007; Duhamel et al., 1998; Schlack et al., 2005). In addition, the visual stimuli used in the human fMRI studies typically extended to only 10 degrees (or less) of eccentricity. Based on previous invasive studies in macaque monkeys, the use of these limited visual stimuli may have substantially underestimated the full extent of pVIP in humans.

Other studies have used either vibrotactile only or visual stimuli only (motion or videos) to activate a more anterior set of areas situated between the superior postcentral sulcus and the upper bank of the anterior IPS (e.g., antIPS in Sunaert et al., 1999; DIPSA in Orban et al., 2006 and Ferri et al., 2015; 2v in Fasold et al., 2008; p2v in Cardin and Smith, 2010; VIP in Smith et al., 2012; pVIP in Furlan et al., 2014; DIPS in Holt

et al., 2014), which overlap the anterior-superior portion of the parietal face area as defined in our previous and current studies.

In sum, because multiple areas in the human IPS and PoCS have been found to respond to visual motion, including optic flow stimuli (e.g., Helfrich et al., 2013; Huang et al., 2015; Konen and Kastner, 2008; Orban et al., 2006; Pitzalis et al., 2013; Sunaert et al., 1999; and others), the location of the human parietal face area (or pVIP) can only be definitely confirmed if a visual-motion-responsive area also responds to tactile, auditory, and/or vestibular stimuli (e.g., Bremmer et al., 2001; Eger et al., 2015; Huang et al., 2012; Sereno and Huang, 2006).

Another confusing issue is the name VIP itself, the ventral intraparietal area. The name originally signified its location in the depths of the macaque monkey IPS. In humans, however, the relatively enlarged inferior parietal lobule (most notably the angular gyrus) results in a medial and posterior displacement of the posterior IPS areas (Sereno and Huang, 2014). Consequently, the probable human homologue of macaque lateral intraparietal area (LIP) is actually located on the “medial” bank of the IPS (Konen and Kastner, 2008; Sereno et al., 2001). Because the human parietal face area (pVIP) is situated somewhat anterior to the expanded angular gyrus, it has been displaced somewhat anteriorly but less further medially compared with the LIP+ (IPS-x; putative human

homologues of macaque area LIP), so that it ends up being slightly lateral to LIP+ (Fig. 4.4A). However, despite these plastic deformations, the general neighbor relations between somatosensory cortex, multisensory cortex, and predominantly visual cortex are preserved.

In the current study, we used spherical morphing and complex-valued surface-based group map averaging techniques to summarize the location and extent of the topologically organized parietal face area across subjects with respect to neighboring unisensory and multisensory areas on the same cortical surfaces (Fig. 4.4A). In the group-average visual maps, one of the dorsal visual retinotopic streams emanating from occipital cortex stretches along the IPS and ends at the parietal face area, which extends between the superior postcentral sulcus and the upper bank of anterior IPS (Huang and Sereno, 2013, 2018; Sereno and Huang, 2014). Thus, from a retinotopic point of view, pVIP is the anterior-most set of a large number of retinotopic areas that extend all the way back to V1.

The anterior border of the human VIP+ complex as defined here essentially reaches the finger (hand) representations in S-I (areas 3a, 3b, 1, and 2). Though we could not completely rule out the possible presence of a thin area in between without additional, high resolution somatosensory mapping, its theoretical extent would have to

be quite narrow. Moving laterally along the postcentral sulcus in the group-average tactile maps, the parietal face area is adjoined by a parietal finger/hand area important for grasping, the human homologue of macaque area AIP (Fig. 4.4A; Borra et al., 2008; Culham et al., 2003; Filimon et al., 2007, 2009; Guipponi et al., 2013; Jastorff et al., 2010). Finally, moving medially, the human VIP+ complex directly adjoins (in fact, slightly overlaps) the parietal body areas (including shoulder and leg representations; Huang et al., 2012), which extend up to the midline (Fig. 4.4A). The parietal finger/hand area is not typically activated by wide-field visual stimuli presented in eye-centered coordinates with the hands at rest alongside the body. The parietal body areas partially overlap the parietal face area and lower-field-driven multisensory cortex at the superiormost ridge of the superior parietal lobule. Taken together, the neighboring unisensory and multisensory areas (LIP+, AIP, S-I [fingers/hand], and parietal body areas in Fig. 4.4A) can be used to precisely define the location of the parietal face area, with its center located superior-medial to the anterior IPS and within the superior postcentral sulcus. Finally, the center of human parietal face area is more heavily myelinated than surrounding areas (Sereno et al., 2012) as originally recognized by Flechsig (1920).

Post-mortem studies have defined another set of differently named cortical areas that partly overlap the parietal face area as defined here. These include areas 7PC and

5L as defined by cytoarchitectonic mapping in humans (Scheperjans et al., 2008a, 2008b). Though these names are different, it is important to point out that no existing literature provides solid evidence for a second area in the human IPS with the necessary multisensory characteristics that define area VIP. Finally, recent dense microelectrode mapping experiments in S-I (3a, 3b, 1, 2) and area 5 summarized several competing parcellations of the IPS in macaque monkeys (Seelke et al., 2012). One way to avoid adding to the ever growing pile of names might be to define the human parietal face and body areas as homologous to macaque areas VIP and 5/PE combined (see Figure 1 in Seelke et al., 2012), which would fit in with them extending anteriorly to directly adjoin area 2 (in S-I) at the postcentral gyrus.

4.4.4 Models of topological organization

Our previous fMRI experiments demonstrated rough topological organization and potential subdivisions within the parietal face area using voxel volumes similar to those used in most cognitive fMRI experiments (Sereno and Huang, 2006). At a higher imaging resolution in the current study, we were able to confirm the existence of one or more topological representations of the contralateral hemiface and visual hemifield within each sROI of the parietal face area across subjects (Figs. 4.2 and 4.3). It is important to

note that topological maps in human PPC generally exhibit substantial interhemispheric (within subject) and intersubject variability as demonstrated in many previous fMRI studies (Hagler et al., 2007; Helfrich et al., 2013; Hoffmann et al., 2009; Huang et al., 2012; Konen and Kastner, 2008; Schluppeck et al., 2005; Sereno and Huang, 2006; Swisher et al., 2007). To guide the interpretation of complex topological organization in human PPC, most studies have shown activation maps overlaid with hand-drawn borders of potential subdivisions (e.g., IPS-1 to IPS-5) for one to a few representative subjects. However, some of the annotated subdivisions were actually missing partial to full hemifield representations. Many human mapping studies have implicitly adopted the assumption that every subject should have the same set of areas with the same set of neighbors. It is clear from dense microelectrode mapping experiments in anesthetized non-human primates that areas are quite variable between individuals (e.g., see Sereno et al., 2015). Imposing a simplified single model (e.g., the IPS-x model) with highly-smoothed, regular-shaped subdivision contours on the observed complex maps defeats the purpose of using high-resolution imaging (e.g., Meier et al., 2008). Furthermore, when maps are averaged across human subjects using surface-based methods, the putative subdivisions in the IPS region become much more difficult to see (e.g., see Huang and Sereno, 2013, 2018), clearly indicating that there is substantial intersubject varia-

tion.

Here, we construct a set of schematic topological models to summarize the different kinds of topological organization of the human parietal face area (VIP+ complex) that we have observed across a large number of single-subject maps in our current and previous studies (Figs. 4.2, 4.3, 4.S7-4.S10; Huang and Sereno, 2007, 2013; Huang et al., 2012; Sereno and Huang, 2006). Topological maps of the parietal face area can be first classified into two major type categories (Fig. 4.4B). Type 1.0 and subtypes exhibit an anterior upper face (or visual field) representation adjoined posteriorly by a lower face (or visual field) representation. Type 2.0 and subtypes exhibit a central upper face (or visual field) representation adjoined by two separate lower face (or visual field) representations ventrally (laterally) and dorsally (medially). Subtypes are formed by expansion (e.g., Types 1.1 and 1.2), subtraction (e.g., Types 2.1 and 2.2), and/or addition (e.g., Types 1.3 and 2.3) of subdivisions in the base types. To keep a minimal model set, slight variation on an existing base type or subtype is indicated by “v” in Figs. 4.S7-4.S10 and Table 4.3. Maps of Types 1.3 and 2.3, slightly differ from each other, exhibit the most complex topological patterns with four lower-to-upper progressions of hemiface or visual hemifield (Figs. 4.4B, 4.S7-4.S10; also see Sereno and Huang, 2014). To be conservative, we only label the anterior subdivisions (VIPv and VIPd; as indicated by

white arrows) that consistently appear in most types. The posterior subdivisions (as indicated by black arrows) may adjoin or overlap with subdivisions of the LIP+ complex, which would need to be confirmed in future studies using a wide-field version of the delayed saccade task (Sereno et al., 2001).

It is important to note that the purpose of topological models and map annotations is to guide the interpretation and understanding the complex and variable topological organization in higher-level cortex, but these models cannot replace the underlying "original" maps. The exact locations, borders (contours), polar-angle gradient orientations (arrows), subdivisions labels, and topological types of these maps remain tentative, and they can/will be iteratively revised. For example, the left sROI of Subject 9 in Fig. 4.S9 can be classified as Type 2.3v (a full complex model) or Type 2.0v (neglecting minor variations in the posterior parts). As another example, the left sROI of Subject 10 in Fig. 4.S7 can be classified as Type 1.0 or Type 2.1, by slightly rotating the polar-angle gradient orientation (arrow) to match that in either type (Fig. 4.4B).

Within and across subjects, the most distinct and consistent feature of the parietal face area (VIP+ complex) is an anteriorly-centrally located upper face (or visual field) representation, which is adjoined by lower face (or visual field) representations ventrally (laterally) and/or dorsally (medially). This topology forms two potential subdivisions,

VIPv (ventral) and VIPd (dorsal), in the VIP+ complex. These names were chosen to indicate that they are not necessarily homologous to subdivisions VIPm (medial) and VIPl (lateral) that have been proposed for macaque area VIP (Lewis and Van Essen, 2000a, 2000b). The lower visual field representation of VIPv extends ventrally/laterally into the anterior IPS to adjoin the parietal hand area (human area AIP), while the lower visual field representation of VIPd extends dorsally/medially to overlap with the parietal body areas at the superior end of the postcentral sulcus (Fig. 4.4; Huang et al., 2012). The lower visual field representations extending from either side of the VIP+ complex, particularly on the dorsal-medial side (VIPd), are present in almost every single-subject map (Fig. 4.S9 and 4.S10). These visual field representations provide additional topological contexts for locating the parietal face area amongst the neighboring unisensory and multisensory areas discussed above (Fig. 4.4A; also see group-average retinotopic maps in Huang and Sereno, 2018; Sereno and Huang, 2014).

4.4.5 Future studies

While the current study only mapped the polar angle coordinate of the contralateral hemiface and visual hemifield, our previous study of wide-field, average retinotopy including both polar angle and eccentricity has suggested that the parietal face area and

nearby areas contain a representation that emphasizes the far periphery (Huang and Sereno, 2013). Future high-resolution mapping studies of eccentricity representation in the parietal face area using wide-field phase-encoded visual stimuli will be needed to refine these observations. Finally, two-dimensional somatotopic mapping of the face using high-density tactile stimuli delivered via a wearable grid will be required to determine how visual eccentricity relates to face somatotopic 'eccentricity' in the parietal face area in future studies (Chen et al., 2017; Huang and Sereno, 2010; Huang et al., 2012; Moulton et al., 2009; Sereno and Huang, 2010).

4.5 Conclusions

High-resolution imaging has identified the human parietal face area as a small region lying inside the superior postcentral sulcus and extending posteriorly to the upper bank of the anterior IPS, rather than in the depths of the IPS (as might be suggested by the name of macaque area VIP). This region is situated slightly lateral to the human LIP+ complex rather than medial to it (again, as might have been suggested by macaque area names LIP and VIP). Using voxel volumes smaller than typically used in cognitive neuroimaging studies, and small, closely-placed, hand-tuned surface coils, we were able to receive strong BOLD signal changes from the parietal face area in response to both air puffs (physical contacts) delivered to the face and wide-field looming objects approaching the face (simulated contacts). The parietal face area's strong sensitivity to these multisensory stimuli in near-face space suggests that it plays an important role in detecting objects intruding into one's peripersonal space; and when they are perceived as potential threats, it is known to participate in promptly initiating and guiding defensive movements (Graziano and Cooke, 2006). Furthermore, the parietal face area plays an important role in multisensory integration and coordination of movements in near-face space (Avillac et al., 2007; Filimon et al., 2007, 2009; Sereno and Huang, 2014). Tactile and visual stimuli with a progressive change in polar angle

around the face activated one or more maps of the contralateral hemiface and visual hemifield in the parietal face area. Across a large number of subjects in our current and previous studies, the topological organization of VIP+ complex consistently shows a anteriorly-centrally located upper face (or visual field) representation adjoined by lower face (or visual field) representations ventrally (laterally) and/or dorsally (medially), forming two potential subdivisions (VIPv and VIPd). Future studies are required to investigate their functional roles in perception and action in peripersonal space (Sereno and Huang, 2014).

4.6 Acknowledgments

This work was supported by the National Institutes of Health (R01 MH081990 to M.I.S. and R.-S.H.), Royal Society Wolfson Research Merit Award and Wellcome Trust to M.I.S., and UC San Diego Frontiers of Innovation Scholars Program (FISP) Project Fellowships to C.-f.C. We thank Eric C. Wong, Larry May, and other faculty and staff at the UCSD Center for Functional MRI for coil development and MRI support.

This chapter, in full, is a reprint of Huang, R.S., Chen, C.F., Sereno, M.I., 2017. Mapping the complex topological organization of the human parietal face area. NeuroImage 163:459-470. The dissertation author used circular statistics to investigate the association of phase angles in the fMRI signals in a voxel responding to visual and tactile stimuli. Also thank Professor Marty Sereno for FreeSurfer support and comments on the manuscript.

4.7 Supplementary materials

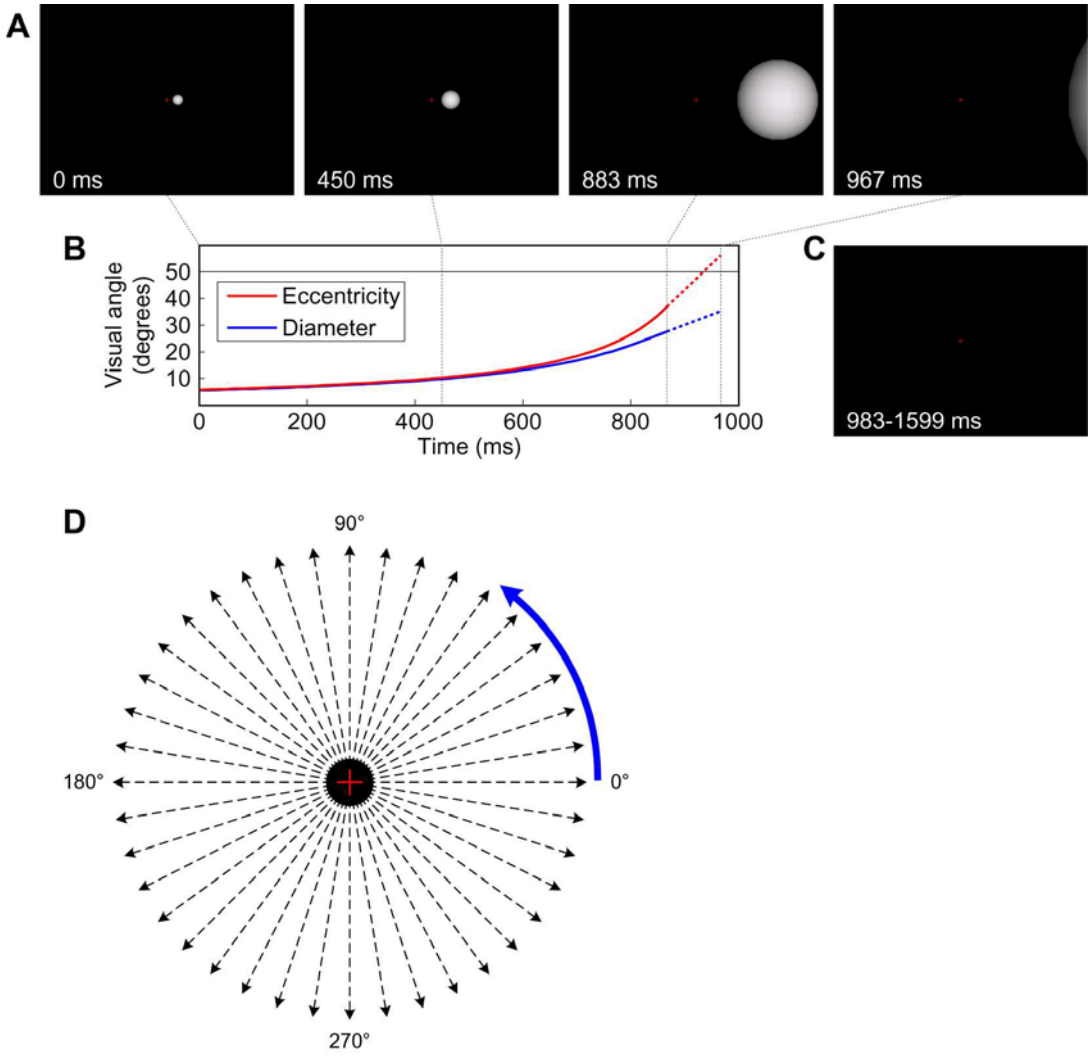

Fig. 4.S1: Looming stimuli in Experiment 2. (**A**) Key frames of stimuli in a representative trial where a looming ball approaches along the horizontal meridian (0°). (**B**) Time courses of eccentricity and diameter of the looming ball. (**C**) Fixation cross against a black background after the ball completely disappears at 983ms. (A-C) reproduced from Huang et al. (2012) with permission. (**D**) Schematic trajectories of the looming ball in a 64-s cycle (40 trials/cycle; trials start at 0°, with a 9° increment per trial in the counterclockwise direction).

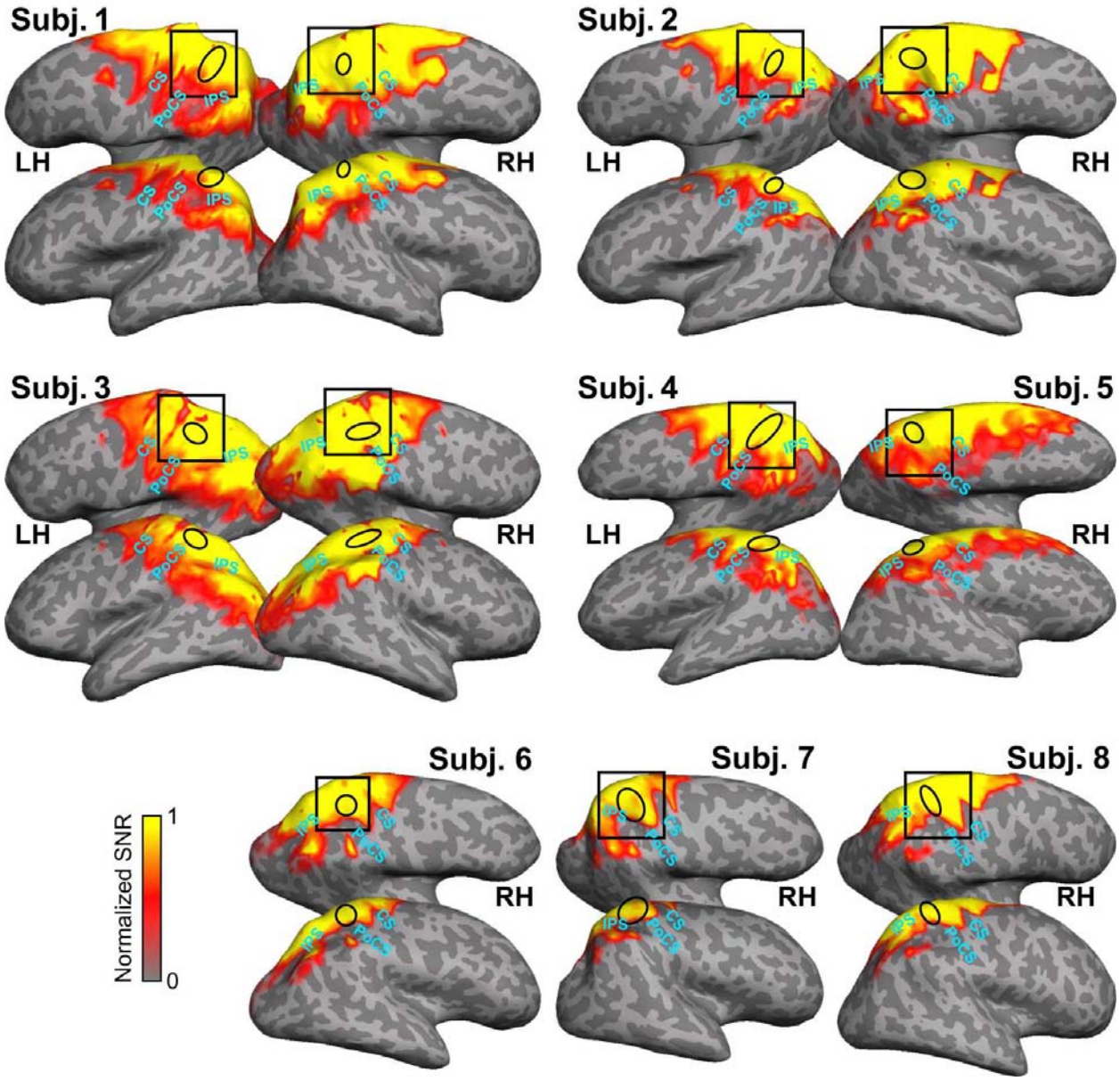

Fig. 4.S2: Surface-based maps showing distribution of SNR in functional scans. All maps and sROIs are displayed in the same views as those in Figs. 4.2 and 4.3. For each voxel, the normalized SNR is obtained by computing the ratio between the average image intensity (averaged across time course per voxel) and background noise (standard deviation of a non-brain region with 10×10 voxels), and then normalized (between 0 and 1) using a sigmoid function.

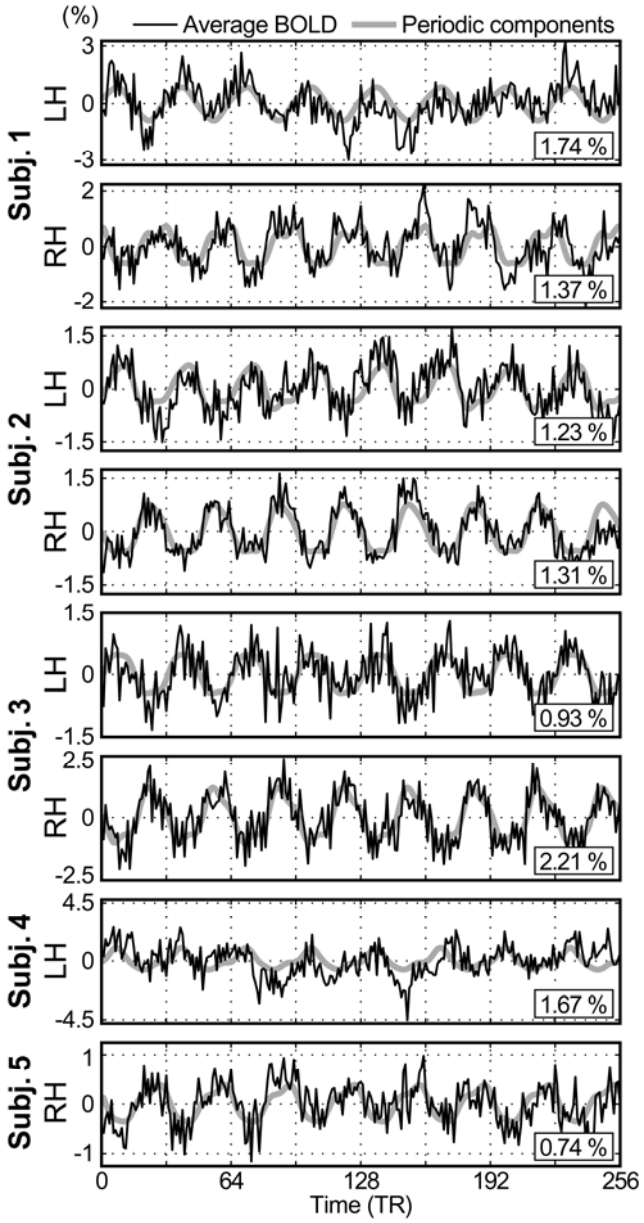

Fig. 4.S3: Time courses of BOLD signals averaged across voxels enclosed in the peak activation region within each sROI in Fig. 4.2. Each thick gray curve represents a periodic waveform reconstructed from the periodic components (harmonics: 8, 16, and 24 cycles per scan) on the Fourier spectrum, with it peak-to-peak signal change indicated in percentage at the lower right corner.

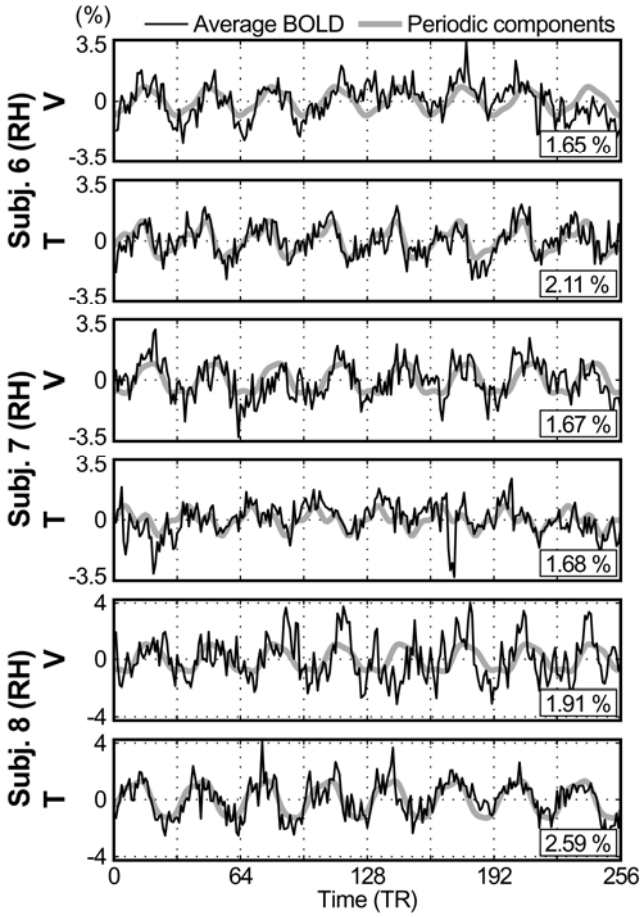

Fig. 4.S4: Time courses of BOLD signals averaged across voxels enclosed in the peak activation region within each sROI in Fig. 4.3. V: visual map (retinotopy); T: tactile map (somatotopy). Other conventions as in Fig. 4.S3.

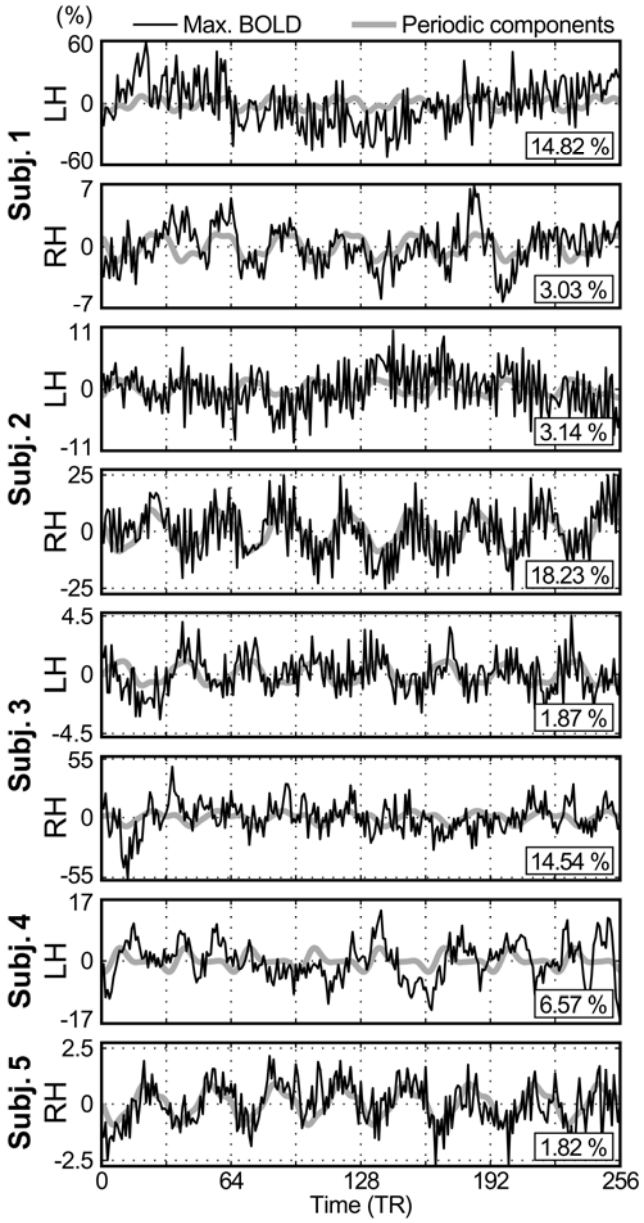

Fig. 4.S5: Time course of a single voxel (enclosed in the peak activation region within each sROI in Fig. 4.2) showing the highest peak-to-peak signal change in the periodic waveform (gray curve) reconstructed from the periodic components (harmonics: 8, 16, and 24 cycles per scan) on the Fourier spectrum. Other conventions as in Fig. 4.S3.

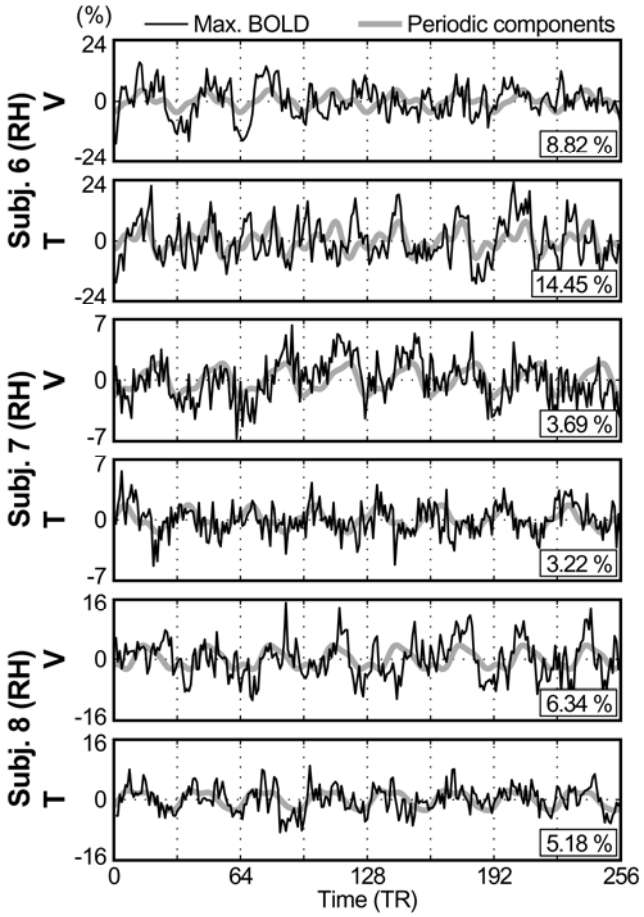

Fig. 4.S6: Time course of a single voxel (enclosed in the peak activation region within each sROI in Fig. 4.3) showing the highest peak-to-peak signal change in the periodic waveform (gray curve) reconstructed from the periodic components (harmonics: 8, 16, and 24 cycles per scan) on the Fourier spectrum. Other conventions as in Fig. 4.S4.

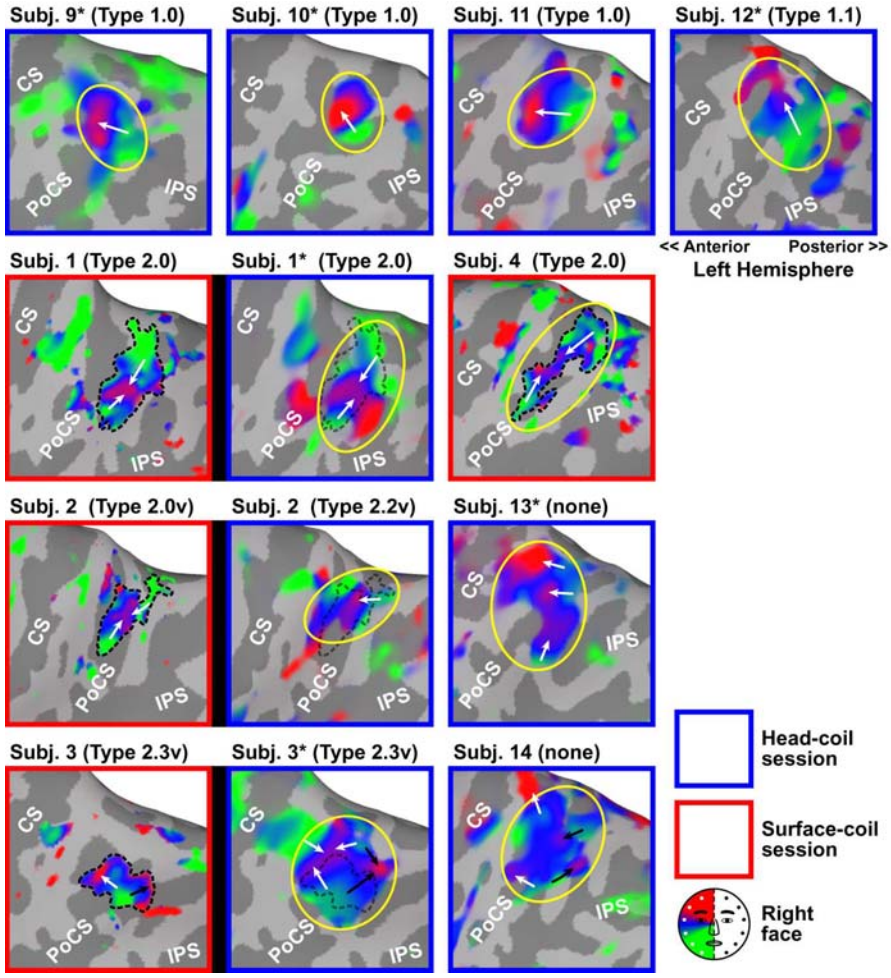

Fig. 4.S7: Somatotopic maps of the parietal face area in the left hemispheres of 10 subjects. Each yellow circle outlines the approximate extent of the parietal face area in a subject whose retinotopic map is also present in Fig. 4.S9. Paired maps in head-coil and surface-coil sessions of the same subject are bound together with a black bar. Dashed black contour: sROI of parietal face area in the surface-coil session; White arrow: anterior subdivision; Black arrow: posterior subdivision; CS: central sulcus; PoCS: postcentral sulcus; IPS: intraparietal sulcus; v: variations on a topological type; *: previously published data (Huang and Sereno, 2007; Sereno and Huang, 2006).

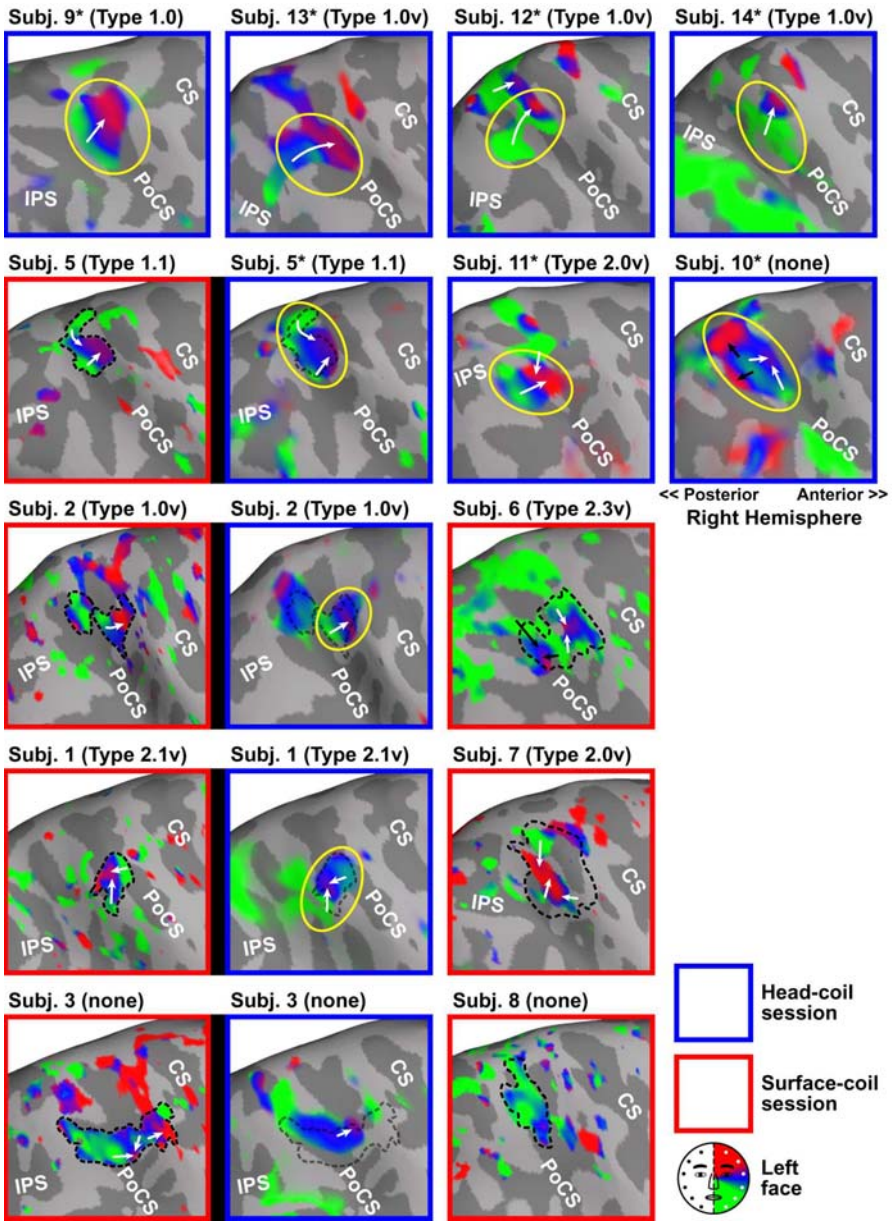

Fig. 4.S8: Somatotopic maps of the parietal face area in the right hemispheres of 13 subjects. Each yellow circle outlines the approximate extent of the parietal face area in a subject whose retinotopic map is also present in Fig. 4.S10. *: previously published data (Huang and Sereno, 2007; Sereno and Huang, 2006). Other conventions as in Fig. 4.S7.

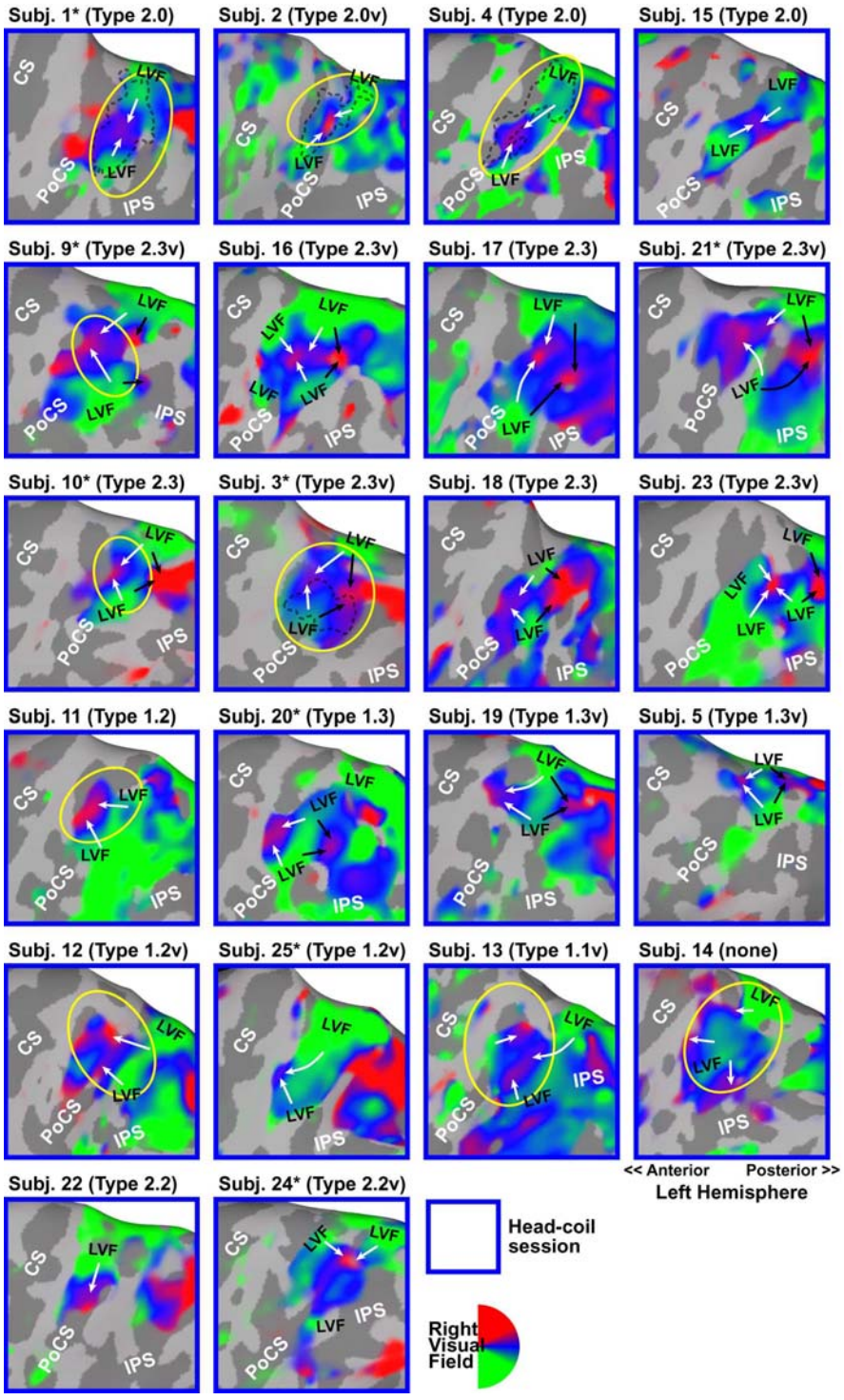

Fig. 4.S9: Retinotopic maps of the parietal face area in the left hemispheres of 22 subjects. Yellow circles: see somatotopic maps of corresponding subjects in Fig. 4.S7; LVF: lower visual field; *: previously published data (Huang et al., 2012; Sereno and Huang, 2006). Other conventions as in Fig. 4.S7.

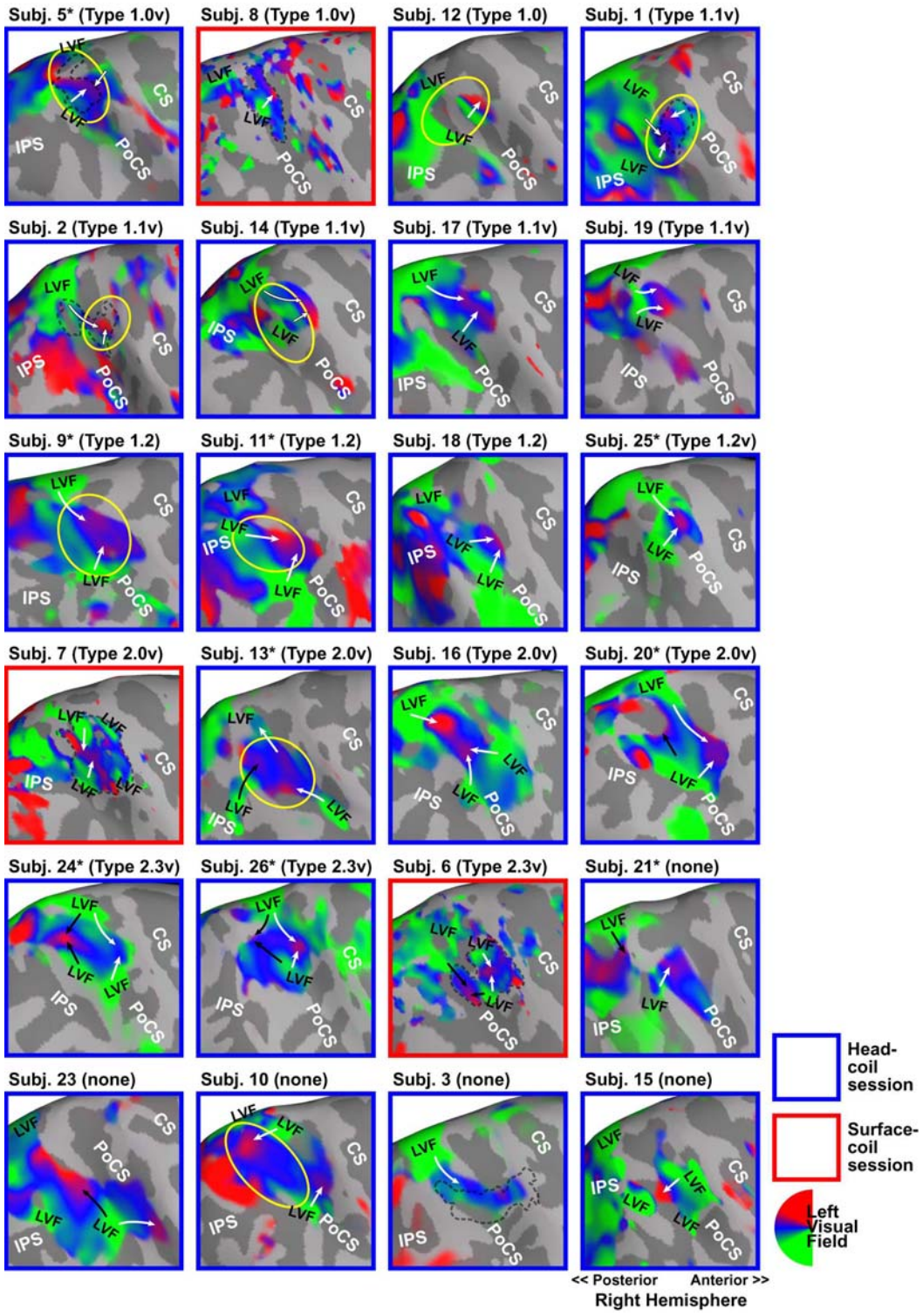

Fig. 4.S10: Retinotopic maps of the parietal face area in the right hemispheres of 24 subjects. Yellow circles: see somatotopic maps of corresponding subjects in Fig. 4.S8; LVF: lower visual field; *: previously published data (Huang et al., 2012; Sereno and Huang, 2006). Other conventions as in Fig. 4.S7.

4.8 References

Avillac, M., Ben Hamed, S., Duhamel, J.R., 2007. Multisensory integration in the ventral intraparietal area of the macaque monkey. J. Neurosci. 27, 1922-1932.

Avillac, M., Deneve, S., Olivier, E., Pouget, A., Duhamel, J.R., 2005. Reference frames for representing visual and tactile locations in parietal cortex. Nat. Neurosci. 8, 941-949.

Borra, E., Belmalih, A., Calzavara, R., Gerbella, M., Murata, A., Rozzi, S., Luppino, G., 2008. Cortical connections of the macaque anterior intraparietal (AIP) area. Cereb. Cortex 18, 1094-1111.

Bremmer, F., Klam, F., Duhamel, J.R., Ben Hamed, S., Graf, W., 2002. Visual-vestibular interactive responses in the macaque ventral intraparietal area (VIP). Eur. J. Neurosci. 16, 1569-1586.

Bremmer, F., Schlack, A., Shah, N.J., Zafiris, O., Kubischik, M., Hoffmann, K., Zilles, K., Fink, G.R., 2001. Polymodal motion processing in posterior parietal and premotor cortex: a human fMRI study strongly implies equivalencies between humans and monkeys. Neuron 29, 287-296.

Buxton, R.B., 2009. Introduction to Functional Magnetic Resonance Imaging: Principles and Techniques, second ed. Cambridge University Press, Cambridge, United Kingdom. ISBN: 978-0-521-89995-6.

Cardin, V., Smith, A.T., 2010. Sensitivity of human visual and vestibular cortical regions to egomotion-compatible visual stimulation. Cereb. Cortex 20, 1964-1973.

Chen, A., DeAngelis, G.C., Angelaki, D.E., 2011. A comparison of vestibular spatiotemporal tuning in macaque parietoinsular vestibular cortex, ventral intraparietal area, and medial superior temporal area. J. Neurosci. 31, 3082-3094.

Chen, C.F., Kreutz-Delgado, K., Sereno, M.I., Huang, R.S., 2017. Validation of periodic fMRI signals in response to wearable tactile stimulation. NeuroImage 150, 99-111.

Colby, C.L., Duhamel, J.R., Goldberg, M.E., 1993. Ventral intraparietal area of the macaque: anatomic location and visual response properties. J. Neurophysiol. 69, 902-914.

Cox, R.W., 1996. AFNI: software for analysis and visualization of functional magnetic resonance neuroimages. Comput. Biomed. Res. 29, 162-173.

Culham, J.C., Danckert, S.L., DeSouza, J.F., Gati, J.S., Menon, R.S., Goodale, M.A., 2003. Visually guided grasping produces fMRI activation in dorsal but not ventral stream brain areas. Exp. Brain Res. 153, 180-189.

Dale, A.M., Fischl, B., Sereno, M.I., 1999. Cortical surface-based analysis. I. Segmentation and surface reconstruction. NeuroImage 9, 179-194.

Duhamel, J.R., Colby, C.L., Goldberg, M.E., 1991. Congruent representation of visual and somatosensory space in single neurons of monkey ventral intraparietal cortex (area VIP). in: Paillard, J. (Ed.), Brain and Space. Oxford University Press, Oxford, UK, pp. 223-236. ISBN: 978-0-19-854284-1.

Duhamel, J.R., Colby, C.L., Goldberg, M.E., 1998. Ventral intraparietal area of the macaque: congruent visual and somatic response properties. J. Neurophysiol. 79, 126-136.

Eger, E., Pinel, P., Dehaene, S., Kleinschmidt, A., 2015. Spatially invariant coding of numerical information in functionally defined subregions of human parietal cortex. Cereb. Cortex 25, 1319-1329.

Engel, S.A., 2012. The development and use of phase-encoded functional MRI designs. NeuroImage 62, 1195-1200.

Fasold, O., Heinau, J., Trenner, M.U., Villringer, A., Wenzel, R., 2008. Proprioceptive head posture-related processing in human polysensory cortical areas. NeuroImage 40, 1232-1242.

Ferri, S., Rizzolatti, G., Orban, G.A., 2015. The organization of the posterior parietal cortex devoted to upper limb actions: An fMRI study. Hum. Brain Mapp. 36, 3845-

3866.

Filimon, F., Nelson, J.D., Hagler, D.J., Sereno, M.I., 2007. Human cortical representations for reaching: mirror neurons for execution, observation, and imagery. NeuroImage 37, 1315-1328.

Filimon, F., Nelson, J.D., Huang, R.S., Sereno, M.I., 2009. Multiple parietal reach regions in humans: cortical representations for visual and proprioceptive feedback during on-line reaching. J. Neurosci. 29, 2961-2971.

Fischl, B., Sereno, M.I., Dale, A.M., 1999. Cortical surface-based analysis. II: Inflation, flattening, and a surface-based coordinate system. NeuroImage 9, 195-207.

Fischl, B., Sereno, M.I., Tootell, R.B., Dale, A.M., 1999. High-resolution intersubject averaging and a coordinate system for the cortical surface. Hum. Brain Mapp. 8, 272-284.

Fisher, N.I., 1993. Statistical Analysis of Circular Data, first ed. Cambridge University Press, Cambridge, UK. ISBN: 978-051-15-6434-5. doi: 0.1017/CBO9780511564345.

Flechsig, P., 1920. Anatomie des menschlichen Gehirns und Rückenmarks auf myelogenetischer Grundlage. Georg Thieme Verlag, Leipzig, Germany.

Furlan, M., Wann, J.P., Smith, A.T., 2014. A representation of changing heading direction in human cortical areas pVIP and CSv. Cereb. Cortex 24, 2848-2858.

Gattass, R., Nascimento-Silva, S., Soares, J.G., Lima, B., Jansen, A.K., Diogo, A.C., Farias, M.F., Botelho, M.M., Mariani, O.S., Azzi, J., Fiorani, M., 2005. Cortical visual areas in monkeys: location, topography, connections, columns, plasticity and cortical dynamics. Philos. Trans. R. Soc. Lond. B Biol. Sci. 360, 709-731.

Graziano, M.S., Cooke, D.F., 2006. Parieto-frontal interactions, personal space, and defensive behavior. Neuropsychologia 44, 845-859.

Guipponi, O., Wardak, C., Ibarrola, D., Comte, J.C., Sappey-Marinier, D., Pinede, S.,

Ben Hamed, S., 2013. Multimodal convergence within the intraparietal sulcus of the macaque monkey. J. Neurosci. 33, 4128-4139.

Hagler, D.J., Jr., Riecke, L., Sereno, M.I., 2007. Parietal and superior frontal visuospatial maps activated by pointing and saccades. NeuroImage 35, 1562-1577.

Helfrich, R.F., Becker, H.G., Haarmeier, T., 2013. Processing of coherent visual motion in topographically organized visual areas in human cerebral cortex. Brain Topogr. 26, 247-263.

Hoffmann, M.B., Stadler, J., Kanowski, M., Speck, O., 2009. Retinotopic mapping of the human visual cortex at a magnetic field strength of 7T. Clin. Neurophysiol. 120, 108-116.

Holt, D.J., Cassidy, B.S., Yue, X., Rauch, S.L., Boeke, E.A., Nasr, S., Tootell, R.B., Coombs, G., 3rd, 2014. Neural correlates of personal space intrusion. J. Neurosci. 34, 4123-4134.

Huang, R.S., Chen, C.F., Sereno, M.I., 2015. Neural substrates underlying the passive observation and active control of translational egomotion. J. Neurosci. 35, 4258-4267.

Huang, R.S., Chen, C.F., Tran, A.T., Holstein, K.L., Sereno, M.I., 2012. Mapping multisensory parietal face and body areas in humans. Proc. Natl. Acad. Sci. U. S. A. 109, 18114-18119.

Huang, R.S., Sereno, M.I., 2007. Dodecapus: An MR-compatible system for somatosensory stimulation. NeuroImage 34, 1060-1073.

Huang, R.S., Sereno, M.I., 2010. Two-dimensional somatotopic mapping of the human face. Abstract in: 16th Annual Meeting of the Organization for Human Brain Mapping, Barcelona, Spain.

Huang, R.S., Sereno, M.I., 2013. Bottom-up retinotopic organization supports top-down mental imagery. Open Neuroimag. J. 7, 58-67.

Huang, R.S., Sereno, M.I., 2018. Multisensory and Sensorimotor Maps. in: Vallar, G., Coslett, H.B. (Eds.), The Parietal Lobe. Neurological and neuropsychological deficits (Handbook of Clinical Neurology, Vol. 151). Elsevier, Amsterdam, the Netherlands.

Jammalamadaka, S.R., SenGupta, A., 2001. Topics in Circular Statistics. World Scientific Publishing Co., River Edge, New Jersey, USA. ISBN: 978-981-02-3778-3.

Jastorff, J., Begliomini, C., Fabbri-Destro, M., Rizzolatti, G., Orban, G.A., 2010. Coding observed motor acts: different organizational principles in the parietal and premotor cortex of humans. J. Neurophysiol. 104, 128-140.

Konen, C.S., Kastner, S., 2008. Representation of eye movements and stimulus motion in topographically organized areas of human posterior parietal cortex. J. Neurosci. 28, 8361-8375.

Lewis, J.W., Van Essen, D.C., 2000. Mapping of architectonic subdivisions in the macaque monkey, with emphasis on parieto-occipital cortex. J. Comp. Neurol. 428, 79-111.

Lewis, J.W., Van Essen, D.C., 2000. Corticocortical connections of visual, sensorimotor, and multimodal processing areas in the parietal lobe of the macaque monkey. J. Comp. Neurol. 428, 112-137.

Meier, J.D., Aflalo, T.N., Kastner, S., Graziano, M.S., 2008. Complex organization of human primary motor cortex: a high-resolution fMRI study. J. Neurophysiol. 100, 1800-1812.

Moulton, E.A., Pendse, G., Morris, S., Aiello-Lammens, M., Becerra, L., Borsook, D., 2009. Segmentally arranged somatotopy within the face representation of human primary somatosensory cortex. Hum. Brain Mapp. 30, 757-765.

Orban, G.A., Claeys, K., Nelissen, K., Smans, R., Sunaert, S., Todd, J.T., Wardak, C., Durand, J.B., Vanduffel, W., 2006. Mapping the parietal cortex of human and non-human primates. Neuropsychologia 44, 2647-2667.

Patel, G.H., Shulman, G.L., Baker, J.T., Akbudak, E., Snyder, A.Z., Snyder, L.H., Corbetta, M., 2010. Topographic organization of macaque area LIP. Proc. Natl. Acad. Sci. U. S. A. 107, 4728-4733.

Pitzalis, S., Sdoia, S., Bultrini, A., Committeri, G., Di Russo, F., Fattori, P., Galletti, C., Galati, G., 2013. Selectivity to translational egomotion in human brain motion areas. PLoS One 8, e60241.

Scheperjans, F., Eickhoff, S.B., Homke, L., Mohlberg, H., Hermann, K., Amunts, K., Zilles, K., 2008. Probabilistic maps, morphometry, and variability of cytoarchitectonic areas in the human superior parietal cortex. Cereb. Cortex 18, 2141-2157.

Scheperjans, F., Hermann, K., Eickhoff, S.B., Amunts, K., Schleicher, A., Zilles, K., 2008. Observer-independent cytoarchitectonic mapping of the human superior parietal cortex. Cereb. Cortex 18, 846-867.

Schlack, A., Sterbing-D'Angelo, S.J., Hartung, K., Hoffmann, K.P., Bremmer, F., 2005. Multisensory space representations in the macaque ventral intraparietal area. J. Neurosci. 25, 4616-4625.

Schluppeck, D., Glimcher, P., Heeger, D.J., 2005. Topographic organization for delayed saccades in human posterior parietal cortex. J. Neurophysiol. 94, 1372-1384.

Seelke, A.M., Padberg, J.J., Disbrow, E., Purnell, S.M., Recanzone, G., Krubitzer, L., 2012. Topographic maps within Brodmann's Area 5 of macaque monkeys. Cereb. Cortex 22, 1834-1850.

Sereno, M.I., Dale, A.M., Reppas, J.B., Kwong, K.K., Belliveau, J.W., Brady, T.J., Rosen, B.R., Tootell, R.B., 1995. Borders of multiple visual areas in humans revealed by functional magnetic resonance imaging. Science 268, 889-893.

Sereno, M.I., Huang, R.S., 2006. A human parietal face area contains aligned head-centered visual and tactile maps. Nat. Neurosci. 9, 1337-1343.

Sereno, M.I. and Huang, R.S., 2010. Finding somatosensory area boundaries in humans with the field sign technique. Abstract in: 40th Annual Meeting of the Socie-

ty for Neuroscience, San Diego, USA.

Sereno, M.I., Lutti, A., Weiskopf, N., Dick, F., 2012. Mapping the human cortical surface by combining quantitative T1 with retinotopy. Cereb. Cortex 23, 2261-2268.

Sereno, M.I., Huang, R.S., 2014. Multisensory maps in parietal cortex. Curr. Opin. Neurobiol. 24, 39-46.

Sereno, M.I., McDonald, C.T., Allman, J.M., 2015. Retinotopic organization of extrastriate cortex in the owl monkey -- dorsal and lateral areas. Vis. Neurosci. 32:e021.

Sereno, M.I., Pitzalis, S., Martinez, A., 2001. Mapping of contralateral space in retinotopic coordinates by a parietal cortical area in humans. Science 294, 1350-1354.

Smith, A.T., Wall, M.B., Thilo, K.V., 2012. Vestibular inputs to human motion-sensitive visual cortex. Cereb. Cortex 22, 1068-1077.

Sunaert, S., Van Hecke, P., Marchal, G., Orban, G.A., 1999. Motion-responsive regions of the human brain. Exp. Brain Res. 127, 355-370.

Swisher, J.D., Halko, M.A., Merabet, L.B., McMains, S.A., Somers, D.C., 2007. Visual topography of human intraparietal sulcus. J. Neurosci. 27, 5326-5337.

Wall, M.B., Smith, A.T., 2008. The representation of egomotion in the human brain. Curr. Biol. 18, 191-194.

5 Conclusion

The phase-encoded design was originally developed in order to make full use of the low temporal samples of fMRI time series in mapping topological organization of visual, auditory, and somatosensory cortices. Phase-encoded fMRI data are typically analyzed by Fourier transform, and an overall signal-to-noise ratio and a single phase of periodic signals are estimated from the entire time series. However, this method cannot fully characterize the temporal dynamics and stability of periodic signals and phases. In research, I developed a data processing pipeline that uses independent component analysis, time-frequency analysis, and circular statistics to comprehensively analyze and model the temporal characteristics of periodic fMRI signals in sensorimotor mapping experiments. This data-driven approach provides additional statistical measures, not obtainable using conventional linear methods, to evaluate the stability (phase jitter) of the observed periodic fMRI signals. These validation methods are fundamental steps to construct a more accurate and comprehensive functional brain atlas of the human sensorimotor cortex.